12-2002

2p or not 2p:The 14O(α,2p) 16O Reaction Rate and Its Implications on Nova and X-ray burst Nucleosynthesis

Luc L. Dessieux, Jr.
University of Tennessee - Knoxville

To the Graduate Council:

I am submitting herewith a thesis written by Luc L. Dessieux, Jr. entitled "2p or not 2p:The 14O(α,2p) 16O Reaction Rate and Its Implications on Nova and X-ray burst Nucleosynthesis." I have examined the final electronic copy of this thesis for form and content and recommend that it be accepted in partial fulfillment of the requirements for the degree of Master of Science, with a major in Physics.

Mike Guidry, Major Professor

We have read this thesis and recommend its acceptance:

Soren Sorensen, Michael Smith, C.C. Shih, Raphael Hix

Accepted for the Council:
Carolyn R. Hodges

Vice Provost and Dean of the Graduate School

(Original signatures are on file with official student records.)

To the Graduate Council:
I am submitting herewith a thesis written by Luc L. Dessieux, Jr. entitled "2p or not 2p:The $^{14}O(\alpha,2p)^{16}O$ Reaction Rate and Its Implications on Nova and X-ray burst Nucleosynthesis." I have examined the final electronic copy of this thesis for form and content and recommend that it be accepted in partial fulfillment of the requirements for the degree of Masters of Science, with a major in Physics.

Mike Guidry
Mike Guidry, Major Professor

We have read this thesis
and recommend its acceptance:

Soren Sorensen
Michael Smith
C.C. Shih
Raphael Hix

Accepted for the Council:

Anne Mayhew
Vice Provost and Dean of Graduate Studies

(Original signatures are on file with official student records.)

2p or Not 2p: The $^{14}O(\alpha,2p)^{16}O$ Reaction Rate and Its Implications On Nova and X-ray Burst Nucleosynthesis

A Thesis

Presented for the

Masters of Science Degree

The University of Tennessee, Knoxville

Luc L. Dessieux, Jr.

December 2002

In the memory of Avey Zapirow

ACKNOWLEDGMENTS

I would like to thank my major Professors Dr. Mike Guidry, Dr Michael Smith and Dr.Raphael Hix for the knowledge of astrophysics I acquired under their guidance and for their support and encouragement. In addition I would like to thank the other members of my committee: Dr. Soren Sorensen and Dr. C.C. Shih also for their help and guidance with the development of my thesis.

Thanks also to members of my group: Erin McMahon, Eric Lingerfelt, Susan Parete-Koon, Wayne Kincaid, John Meyer, and Viktor Chupryna for their help with editing my thesis and practicing my defense.

Special thanks to my parents Luc and Jaccinette for supporting me in the pursuit of this degree, to my siblings Rools, Lesly, Guesly, Sabine, and Melinda for their support in pursuit of this thesis, and to my significant other Olivera Lukajic whom at times is my rock.

I would also like to Thank Dr. Lee Riedinger and Dr. Soren Sorensen, the former and present head of the physics department, for the award of a teaching assistantship.

ABSTRACT

During explosive hydrogen burning, the catalytic CNO cycle suffers depletion by additional thermonuclear capture reactions on the members of the cycle. This " break out" from the β-limited CNO cycle has been suggested to occur in novae and X-ray bursts for temperatures greater than 0.4 GK [3,26,28]. At these temperatures α captures can occur on the CNO waiting point isotopes through the nuclear reactions $^{14}O(\alpha,p)^{17}F$, $^{15}O(\alpha,\gamma)^{19}Ne$, and $^{18}Ne(\alpha,\gamma)^{21}Na$ [3]. An additional reaction, $^{14}O(\alpha,2p)^{16}O$ has been suggested as a possible break out path from the CNO cycle [49]. To investigate the astrophysical significance of the $^{14}O(\alpha,2p)^{16}O$ reaction for the isotopes that are synthesized during novae outbursts and X-ray bursts, the unknown rate of this new reaction and the accepted rate of $^{14}O(\alpha,p)^{17}F$ have been varied using a scaling factor from negligible (10^{-9} of the $^{14}O(\alpha,p)^{17}F$ accepted rate), to a value exceeding the accepted $^{14}O(\alpha,p)^{17}F$ rate by a factor of 10^3. If this new rate is found to have significant astrophysical implications, it could be investigated with a radioactive beam at the Oak Ridge National Laboratory's Holifield Radioactive Beam facility.

For a nova occurring on a 1.35 $M_\odot$ white dwarf, we found that varying the $^{14}O(\alpha,p)^{17}F$ reaction rate by 12 magnitudes (ranging from 10^{-9} to 10^3 times the accepted rate) has an insignificant effect on the final abundances produced. When the unknown $^{14}O(\alpha,2p)^{16}O$ reaction rate is added into the reaction rate library with a value assumed equal to the accepted $^{14}O(\alpha,p)^{17}F$ rate and the rate varied by 12 magnitudes, no significant effect was observed on the final abundances. The effect on the 1.25 $M_\odot$ ONeMg white dwarf was even smaller, and still smaller for the 1.00 $M_\odot$ C-O white dwarf.

For the X-ray burst case, variation of the $^{14}O(\alpha,p)^{17}F$ reaction rate over 12 magnitudes revealed four distinct groupings of results from the scaled rate. When the rate is reduced by factors between 10^{-1} and 10^{-3} an enrichment of 20%-30% is observed in the CNO isotopes and A=20-50 mass region when compared to the case using the accepted $^{14}O(\alpha,p)^{17}F$ rate. The energy production is consistent with that of the calculation with the accepted rate. At factors greater than unity compared to the accepted rate, we observed a 20%-30% depletion in the CNO isotopes. When the $^{14}O(\alpha, p)^{17}F$ rate is mildly dominant (10^{-4} to 10^{-6} of the accepted $^{14}O(\alpha,p)^{17}F$ rate), we observed an enrichment in both the CNO isotopes and the A=20-50 mass region by a factor up to 7, while the A=51-72 mass region is depleted by a factor up to 7. When the $^{14}O(\alpha, p)^{17}F$ rate is not dominant (10^{-7} or less of

the accepted $^{14}O(\alpha,p)^{17}F$ rate), we observed a depletion in both CNO isotopes and the A=20-72 mass region by factors up to 60, due to a one second delay in energy production caused by the reduced rate. ^{56}Ni is a good candidate for observation as depletion and enrichment occurs in the A=51-72 mass region as a function of the scaled rate.

When the $^{14}O(\alpha,2p)^{16}O$ rate is added to the reaction rate library with a value assumed equal to the accepted $^{14}O(\alpha,p)^{17}F$ rate, and than varied in the same manner as the $^{14}O(\alpha,p)^{17}F$ rate, we observed three distinct groupings of behavior for X-ray bursts. When the $^{14}O(\alpha,2p)^{16}$rate is reduced by a factor of 10^{-1} or less, we find no change in nucleosynthesis or energy production when compared to the case using the accepted $^{14}O(\alpha,p)^{17}F$ rate. When the $^{14}O(\alpha,2p)^{16}O$ rate is set equal in strength to the $^{14}O(\alpha,p)^{17}F$ rate, we observed a depletion of less than 10% in ^{14}O and ^{16}O. The energy production is consistent with that of the accepted rate. At factors greater than unity compared to the accepted $^{14}O(\alpha,p)^{17}F$ rate, we observed a depletion of up to 33% and 25%in ^{14}O and ^{16}O respectively. The energy production is consistent with that of the known $^{14}O(\alpha,p)^{17}F$ rate . During the X-ray burst the $^{14}O(\alpha,p)^{17}F$ reaction is pivotal for energy generation, while the unmeasured $^{14}O(\alpha,2p)^{16}O$ reaction has an insignificant effect on energy production and final abundances during the X-ray burst.

TABLE OF CONTENTS

CHAPTER **PAGE**

LIST OF FIGURES

LIST OF TABLES

“What may only appear to be a white puff of smoke in space is actually the violent end of one stellar system and the possible beginnings of another.” P. Scoma, 1968

Chapter 1

Introduction

1.1 Less Massive Type stars

The fate of a star depends on the mass with which it was born. The fate of stars more massive than 8-10 times our sun is quite different than their less massive brethren [1]. A less massive star, for example, our Sun, upon collapsing to the main sequence from a nebula (a gaseous cloud of dust) will become a yellow dwarf. As a yellow main sequence star, the star will burn hydrogen into helium. The star will remain in that state for approximately 10 billion years.

After 10 billion years, the hydrogen at the center of the star will be nearly completely converted into helium. The (now helium) core is surrounded by a shell of burning hydrogen. There is no fusion at the core of the star because the temperature is too low to fuse helium, so the internal pressure will diminish. As a result, gravity will contract the core, increasing the temperature. This contraction also heats the shell, enhancing the rate at which hydrogen fuses to helium, causing the surface of the star to swell. Its surface temperature drops to roughly 2000 K, the star will appear reddish

and remains at this stage for roughly ten million years. Such a star is called a red giant.

While the outer layers are expanding, the inner core continues to contract and heat up, eventually reaching a temperature of 100 million K. It is at this point that three helium nuclei can fuse to form carbon by the 3α process. The red giant star will exhaust its entire core of this fuel; the (now carbon and oxygen core), surrounded by helium and hydrogen shells, will contract and heat up again, similar to the preceding scenario with the helium core. However, pressure from degenerate electrons halts the contraction before carbon can fuse. Instabilities develop in the shells leading to dramatic oscillations which eject the outer envelope of the star, leaving the bare core behind. The core of the star is now a hot white dwarf with a surface temperature of roughly 100,000 Kelvin or more. The ejected envelope forms an emission nebula around the white dwarf that is termed a planetary nebula. The star will remain in this stage for roughly 50,000 years. Over that time, the gas around the star will spread and fade out, leaving just the white dwarf behind. Stars with initial mass less than roughly 10 solar masses will end their life as white dwarfs. The remnant white dwarfs have masses less than about 1.4 solar masses, the Chandrasekhar limit. Matter within these stars is packed into a volume the size of the earth,

which means that white dwarfs are very dense; their density is approximately 10^6 g/cm^3.

1.2 Massive Stars

Massive stars face a different fate than that of the less massive stars. Upon collapsing as blue giants onto the main sequence, the massive stars (those with mass more than 10 times our sun) will be the most luminous stars in the sky. Their surface temperatures will range as high as 40 thousand Kelvin, which means they are the hottest stars in the sky. However, even with 10 times the fuel they cannot last as blue giants for long.

They burn their hydrogen fuel rapidly due to their high luminosity. A blue giant exhausts its central hydrogen by fusing it into helium. The star's core will contract and its outer layers will expand. The core will transform its helium into carbon via the triple alpha process and the temperature in the core will exceed 600 million Kelvins. High luminosity from the overlying shells causes the outer layers to continue to expand even as the helium exhausts itself into carbon. The star is now a red supergiant with a carbon-oxygen core surrounded by helium and hydrogen shells.

Unlike less massive stars, the core is supported by radiation pressure in addition to electron degeneracy. Following helium exhaustion, the now

carbon-rich core contracts, heats up and continues to fuse heavier elements. The thermonuclear process produces neon burning after the carbon exhaustion, oxygen burning after neon exhaustion, silicon burning after oxygen exhaustion, and finally the silicon exhausts itself into iron. (Although we may speak of these reactions in these schematic terms, the actual process leading to iron production involves a complex set of near-equilibrium reactions.) Fusion of iron into heavier elements consumes energy instead of releasing it. With no available source of energy the buildup of this inert iron-rich core signals the impending violent death of the massive star.

The now iron-rich core cools via emission of neutrinos, which carry away energy and remove thermal pressure support from the core [64]. To compensate for the energy and pressure drainage by neutrinos, the star must provide more energy by burning thermonuclear fuel, or contracting, or both. Because the core is composed of iron the only source of energy is contraction. Unable to support itself against its own gravity, the core collapses.

The collapse is accelerated by the increasing electron capture rate, which removes the pressure support provided by the electrons [64]. The neutrinos produced by electron captures continue to escape the core until the

core reaches nuclear density. The core becomes very stiff, and inner core collapse is halted as the unsupported shells collapse inward at speeds up to 15% the speed of light [25].

As the matter falls on the stiff core, enormous pressure and temperature develops [1], and the inner core rebounds as a whole, sending out pressure waves. The pressure waves form a shock that propagates supersonically toward the surface of the star. Energy losses to escaping neutrinos and photodissociation cause the shock to stall and become an accretion shock. If it is not revitalized the supernova fails and the star collapses into a black hole. However, the copious numbers of neutrinos that are produced from the newly formed proto neutron star rejuvenate the shock it escapes from the core. The now hot core is a proto neutron star, it will radiate neutrinos as it cools and contracts, and eventually become a neutron star if the shock continues to propagate, or possibly a black hole if it accretes enough mass. The outer layers are lifted because of the revitalized shock, and the star increases tremendously in brightness and is termed observationally a (core collapse) supernova.

1.3 White Dwarfs

A white dwarf is the remnant of a star that is no longer supported by thermonuclear reactions at its core, but rather by electron degeneracy. We

will explain electron degeneracy in chapter 2. For our discussion, we may distinguish two types of white dwarfs (hereafter WD). For stars with initial main sequence mass less than about 8 solar masses, helium burning is the final thermonuclear burning stage [18]. The result is a carbon-oxygen core surrounded by a thin helium envelope [2]. This is the carbon-oxygen WD (hereafter C-O WD). For stars with initial main sequence mass ranging from 8 solar masses to 10 solar masses, carbon burning occurs producing elements all the way to magnesium [18]. An oxygen-neon-magnesium core is left behind; this is referred to as an oxygen-neon-magnesium WD (hereafter ONeMg WD). The ONeMg WDs are the more massive WDs with masses that range from 1.25 solar masses to 1.35 solar masses. The CO WDs are the less massive WDs and typically have a mass below 1.0 solar mass.

The elements found in the interior of WDs are completely ionized, forming a Coulomb plasma [13]. Since the densities of WDs are large, the ions in a cool WD form a crystalline lattice embedded in an electron gas [2]. Gases at the cores of WDs are degenerate, while the thin surface gas of a WD is non-degenerate.

WDs are of interest in this study when they occur in a cataclysmic variable [hereafter CV] system and they serve as a host for nova outbursts.

A classical nova outburst is a thermonuclear runaway that occurs on the surface of a WD that has been accreting hydrogen-rich matter from a close binary companion. The companion star in the CV system is a main sequence or giant star.

1.4 Pre-Nova Conditions

In a CV system the stars have formed a shared gravitational potential. The innermost potential contours of the two stars are spherical, growing less so as one retreats from each star. The contours will intersect at a unique point lying between the two stars where the two gravitational potentials are equal [14], this point is called the inner Lagrange point. This equipotential contour defines two regions, one around each star, which are called Roche lobes (see fig 1). However, when a binary system involves a WD and a main sequence star, the companion star may eventually fill it Roche lobe (see fig1; for further reading see 20,21) because of stellar evolution. As a result, some of the hydrogen-rich layer of the other star (hereafter, donor star) will flow through the Lagrange point into the gravitational potential of the WD. This hydrogen-rich matter will have high velocity and angular momentum, it will often swirl around the WD, creating an accretion disk that eventually settles on the surface of the WD, raising the surface temperature of the WD and setting the stage for a thermonuclear runaway.

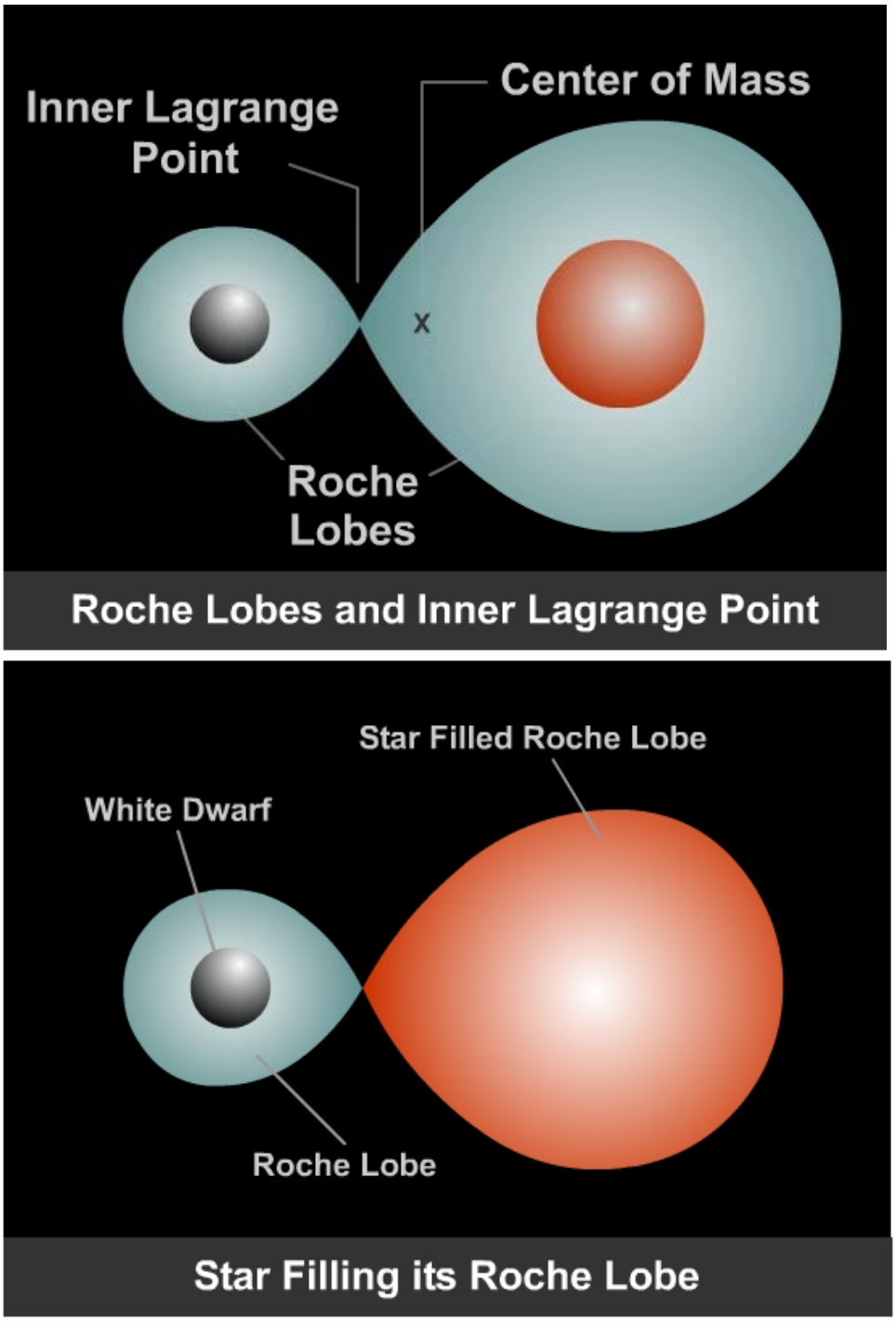

Source: OJTA

Figure 1 Above: Roche lobes and the inner Lagrange point. Below: donor star filling its Roche lobe.

The mechanism for the loss of velocity and angular momentum that causes the settling of matter from the accretion disk onto the white dwarf is not well understood; however, it is believed that viscosity within the disk transfers the angular momentum outward and the orbit of the matter decays until it swirls down onto the surface of the WD [4].

As matter streams from the donor star and accretes on the WD, it will release energy as it interacts with the WD and the previously accreted matter in the disk. This will increase the average kinetic energy of the excited nuclei and the electron gas, thus increasing the temperature. The mass accretion rate and accreted envelope will determine the luminosity and temperature of the WD [18]. If matter is accreted too fast, the material will become hot during the accretion process, and steady burning of hydrogen to helium will occur. This fast accretion can produce a thick layer of helium that can serve to ignite a thermonuclear runaway that is so violent that the WD is destroyed [22].

However, a large accretion rate will produce a more luminous and hotter envelope for the WD. The temperature is important because it helps determine the time of ignition and the degree of degeneracy before the thermonuclear runaway is ignited. The material in the envelope will have kinetic energy given by

$$E = kT \quad (1.1)$$

where T is the temperature in Kelvin (K) and k is the Boltzmann constant, k = $8.617*10^{-8}$ keV/K. The hotter the accreted layer is, the more energetic the particles in the envelope will be. This is important because the reactions in the thermonuclear runaway involve the capture of protons into a nucleus already containing a number of protons; thus a large kinetic energy is needed to overcome the strong repulsive Coulombic barrier.

The ejecta of novae are observed to be enriched in heavier isotopes and the hydrogen that is accreted onto it. It is widely accepted that these heavier isotopes (like magnesium, sodium, and aluminum) are matter that were processed heavy seed nuclei that were dredged off the core of the WD [3,18]. The dredging mechanism is not yet well understood, but three explanations have been proposed for the matter that is mixed on the surface. Some have suggested it takes place by diffusion-induced convection [3,23]. Others have suggested it takes place by shear-induced convection [3,12]. Recently [29] have suggested that mixing may take place by slow convective motion.

1.5 Neutron Stars

Neutron stars (hereafter NS) are the remnant cores of massive stars; they are degenerate just like the WDs, but their cores are made of a

degenerate neutron gas instead of a degenerate electron gas. They can be thought of approximately as a large atomic nucleus, containing 10^{57} neutrons packed into a sphere 10 kilometers in radius. In addition to being extremely dense, neutron stars have other remarkable properties. For example, they may rotate as fast as 1000 times per second, they may have a very strong magnetic field (up to 10 trillion Gauss), and their surface temperatures are very high (up to 1 million Kelvin). Some rotating neutron stars emit beamed electromagnetic radiation; they are known as pulsars. Just as WDs have an upper mass limit, neutron stars have an upper limit on their mass, above which even degeneracy pressure is insufficient to support them against gravitational collapse. The upper limit is somewhat uncertain, but is believed to be around 3 solar masses. A more massive would-be neutron star will collapse into a black hole.

Neutron stars are of most interest to us in a binary system, where they may accumulate matter in the same fashion as the white dwarf and an X-ray burst may occur. An X-ray burst (hereafter XRB) is the result of thermonuclear runaway that occurs on the surface of neutron star that has been accreting hydrogen rich matter from a close binary companion. The mechanism for the XBR is comparable to that of the nova although the conditions on the surface of the NS are more extreme than those of a WD.

The next chapter will discuss the electron and neutron degeneracy found in these stellar corpses that we have termed white dwarfs and neutron stars.

Chapter 2
Degeneracy

2.1 Electron And Neutron Degeneracy

The physics of stellar evolution is governed primarily by three sets of microscopic physical properties of the stellar material, the opacity, which we will not discuss in this thesis, the nuclear reaction rates, which we will discuss at great length in chapter 4, and the equation of state. The equation of state is a relationship among thermodynamic variables. In the case of most interest here, the equation of state is the relationship between the density, temperature, and pressure of the stellar material. To further understand stellar structure we need to understand this relationship at a star's surface, and in its interior.

We have indicated in the previous chapter that for a WD the interior contains degenerate electrons, while the gases on its surface are not degenerate. We have also made a similar statement for the NS, where its core contains of degenerate neutrons instead of electrons. At the surface of both degenerate objects the gas obeys approximately the ideal gas law

$$PV=NRT \quad (2.1)$$

where the pressure and the temperature are linearly related. This indicates that the gas maintains a Maxwell-Boltzmann distribution. The story is not as

simple in the core where the pressure is so extreme that it squeezes the atoms into a volume smaller than the ionic radius of the atom.

2.2 Electron Degeneracy

The gases inside the WD are completely ionized. Ionization can occur in a gas if the temperature is high, or if the density of the gas is high enough even at low temperature; this latter case is termed pressure ionization. Pressure ionization implies the possibility of producing a cold gas of electrons [16].

Heisenberg's uncertainty principle states that if a measurement of position is made with precision Δx and a simultaneous measurement of momentum is made with precision Δp, then the product of the two uncertainties can never be smaller than the order of ħ [17].

$$\Delta x \Delta p \geq \hbar/2 \qquad (2.2)$$

This means that for a two-dimensional phase space the quantum state can be represented by an area ħ/2 for each spin quantum number of the electron. But since we are dealing with free electrons, it is best that we describe the quantum state in 6-dimensional phase space, x, y, z, p_x, p_y, p_z where these quantities describe the position (x, y, z) and momentum (p_x, p_y, p_z)of the electron. Hence we can rewrite equation 2.2 as

$$\Delta x \Delta y \Delta z \Delta p_x \Delta p_y \Delta_z \geq \hbar^3 \qquad (2.3)$$

Thus we can think of a unit volume of phase space as $\hbar^3$.

Electrons are Fermions, a class of particles having half-integer spin quantum number that obey Fermi-Dirac statistics. Electrons can have a spin projection of 1/2 or –1/2. The Pauli exclusion principle states that no two Fermions can occupy the same quantum states; this means that a volume of phase space, $\hbar^3$, can contain at most two electrons, and then only if their spin projections are different.

A completely degenerate gas is one where all the lowest available momentum states are full, and thus the gas does not follow a Maxwell-Boltzmann distribution. In the high-density interior of the WD, the electrons become highly crowded. This will lead to a point where electrons of the same momenta will occupy almost the same positions. We can thus consider that volume of phase space to be full; only if the momentum of any additional electron is different will it be possible to put any other electron in that volume. Therefore, the additional electrons will be forced to have higher momentum in order to obey Pauli's exclusion principle. A higher momentum implies higher kinetic energy. As a result, the gas will have greater pressure than it would have if it were an ideal gas at the same temperature.

In a non-degenerate plasma the electrons are typically responsible for most of the pressure, so an increase in T in equation 2.1 indicates that the electrons are moving faster, thus absorbing the energy and increasing the pressure so that ultimately the gas will expand. But, in a degenerate electron gas the constraints on the quantum mechanical energy state complicate the absorption of energy by the electrons when the temperature is increased. An increase in temperature does not lead to a corresponding increase in pressure for a fully degenerate gas. In a completely degenerate gas, all the lower energy states are filled up to an energy level called the Fermi level, E_F [14]. E_F is directly related to the Fermi momentum, and the Fermi momentum increases as the density of the gas increases. The natural temperature scale for the gas, known as the Fermi temperature T_F, is directly related to the Fermi energy and can be written as

$$E_F = kT_F \quad (2.4)$$

where k is the Boltzmann constant. Note that T_F is not the physical temperature of the gas; but when the temperature of the gas is lower than T_F, the gas is referred to as a cold degenerate electron gas. While the temperature is less than the Fermi temperature, the additional kinetic energy from the increase in temperature is a small fraction of the kinetic energy due to degeneracy. Therefore, an increase in temperature results only in a minute

increase in pressure. However, the non-degenerate positive ions will absorb the energy [16]; their equation of state can be treated by equation 2.1.

2.3 Neutron Degeneracy

Neutrons, like electrons, are fermions, so they follow Fermi-Dirac statistics. The neutron degenerate gas found in the NS behaves in many ways like the electron degenerate gas found in the WD (though on very different temperature and density scales). As the density increases in the later stages of massive stellar evolution, the E_F of the electrons gets large enough that the energetic electrons will react with protons inside or outside nuclei [14] through the weak interaction to create neutrons and neutrinos. As we have already discussed, the neutrinos will escape the star. Thus we are left with a degenerate neutron gas, since all the lower energy neutron states will be filled and a Maxwell-Boltzmann distribution will not be maintained. Both the electron degenerate gas and the neutron degenerate gas will behave much like matter at zero temperature, even if the actual temperature is tens of millions of Kelvin.

The next chapter will discuss both X ray bursts and novae, and the nucleosynthesis that occurs on each. The classic nova and XRB occur in electron degenerate conditions.

Chapter 3
Nucleosynthesis

The term nucleosynthesis refers to the formation of atomic nuclei. As we have discussed in Chapter 1, all main sequence stars convert hydrogen into helium and a number of the less massive type stars later convert helium into carbon and a few convert carbon into magnesium. We have also seen that the massive stars will convert hydrogen all the way to iron through a series of burning stages. These conversions will take place via nuclear fusion. Radioactive nuclei are important in many astrophysical phenomena, such as the early universe, red giant stars, nova explosions, X-ray bursts, supernova explosions, and supermassive stars. All of these phenomena are examples of element production sites. The sites differ in the element production processes that they support. A few of these processes are slow neutron capture process (s process) which occurs in the beta stability valley (the region of the Chart of Nuclides where nuclei that are stable against radioactive decay reside), the rapid neutron capture process (r process) which occurs near the neutron drip line (the region of the Chart of nuclides, where neutrons appear to drip out of nuclei) and the rapid proton process (rp-process), which occurs near the proton drip line (the region of the Chart of nuclides where protons appear to drip out of nuclei). The range of nuclei

produced by these processes and the stellar phenomena in which they occur are detailed in figure 3.1. In this thesis we shall study the burning of hydrogen on the surface of white dwarfs and also on the surface of neutron stars, processes that run along the proton rich side of stability. We present a brief discussion of the nucleosynthesis of both novae and X-ray bursts. The interested reader is encouraged to consult the literature [4,27,30,34,40] for a more detailed discussion.

3.1 Novae

Because of the large density of a white dwarf, the matter in the envelope will become degenerate through gravitational compression. Once that occurs a critical pressure must be reached at the base of the accreted envelope for the thermonuclear runaway to ignite. By substituting this critical pressure into the expression for hydrostatic pressure

$$P_{crtical} = \frac{GM_1 M_e}{4\pi R^4} \tag{3.1}$$

where M_1 is the mass of the WD, and R is the surface radius of the WD, one may solve for M_e, the mass of the envelope at ignition. Gravitational compression releases heat and produces a temperature of roughly 10^7 K at the bottom of the degenerate envelope igniting fusion of hydrogen into helium via the pp-chain, and releasing energy.

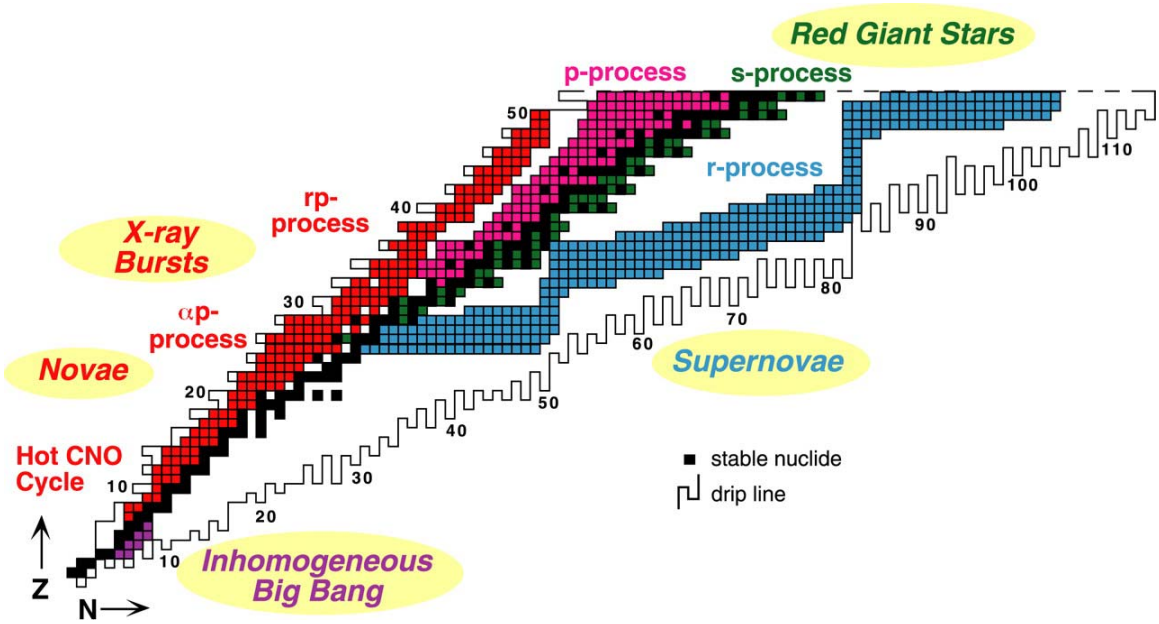

Source: M.S. Smith & K.E. Rehm, Annu Rev. Nuc. Part. Sci., **51**: 130(2001)

Figure 3.1 The different processes that synthesize matter and the sites where they occur.

The further evolution of thermonuclear burning on the WD now depends upon the initial mass and initial luminosity of the WD, the rate of mass accretion, and the chemical composition of the reacting layers [4]. As we discussed, the more massive a WD, the less massive the envelope needed to produce a thermonuclear runaway, and for a given WD mass the luminosity decreases as the accretion rate increases [4]. If the WD is too luminous and the accreted matter is not degenerate, thermonuclear reactions may occur, but there will not be an ejection of the accreted material.

During the early stages of nuclear burning, the envelope evolves slowly since energy generation is dominated by the pp chain which has a temperature dependence of approximate T^4. At this stage the nuclear burning timescale is much longer than the timescale of envelope accretion. However, when the temperature exceeds 18 million Kelvin, the hot CNO cycle becomes dominant [15]. The reactions of the hot CNO cycle have a temperature dependence of T^{16}-T^{18} [4]. The rate of the reactions increases by orders of magnitudes, releasing energy faster than it can be radiated. Because of the degeneracy, the released energy greatly increase the temperature while the density and pressure remain approximately constant . As a result a thermonuclear runaway (hereafter TNR) takes place. The TNR is enhanced by dredged up ^{12}C and ^{16}O, which act as catalysts for the hot

CNO cycles, a series of proton captures on isotopes like carbon, nitrogen, oxygen and fluorine, coupled with beta decay reactions, to produce helium (see figure 3.2). Once the TNR has generated a temperature of 10^8 Kelvin the nova reaches it maximum luminosity and the TNR will release enough energy to eject most of the accreted material.

For ejection to occur the degeneracy in the envelope must be lifted. This occurs once the temperature of the envelope exceeds the Fermi temperature T_F for the electrons in equation 2.2, which can also be expressed as

$$T_F = 3.03*10^5(\rho/\mu_e), \qquad (3.1)$$

where ρ is the density (in g cm^{-3}) and μ_e is the electron mean molecular mass. The lifting of degeneracy will allow the envelope to expand and that will slow or stop the TNR. If the envelope temperature rises too fast and expansion has not begun, that will stop any further rise in envelope's temperature [4]. As a result, a convective zone at the bottom of the envelope is formed. The convective zone will grow to the surface and becomes a vehicle for the β^+ emitters, produced by the hot CNO cycle, to transfer to the surface [27]. The outward flux of β-decay energy can increase the luminosity to values in excess of 10^{38}ergs/sec.

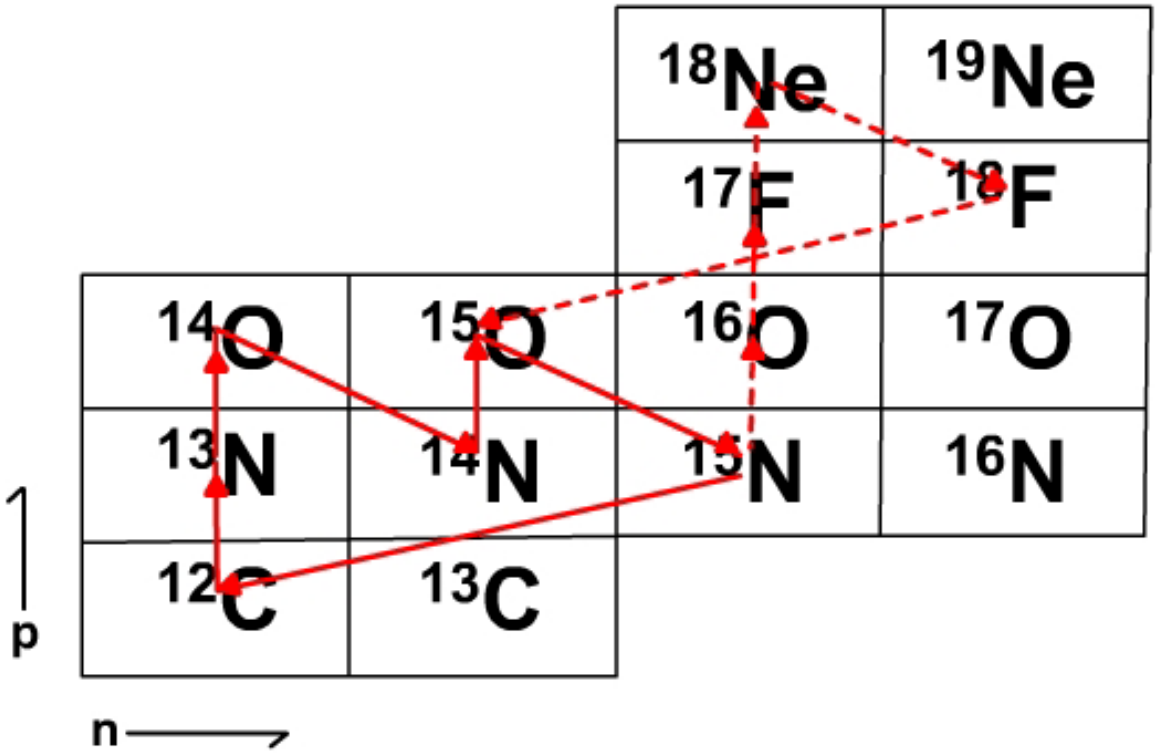

Source: M. Wiescher, J. Gorres and H. Schatz , J. Phys. G: Nucl. Part. Phys.,**25,** R133 (1999)

Figure 3.2 The hot CNO cycles are a series of proton captures on intermediate mass isotopes like carbon, nitrogen, and fluorine that, coupled with beta decay reactions, lead to the fusion of four protons into helium. The first cycle shown by the red solid line is $^{12}C(p,\gamma)^{13}N(p,\gamma)^{14}O(\beta^{+}\nu)^{14}N(p,\gamma)^{15}O(\beta^{+}\nu)^{15}N(p,\alpha)^{12}C$. The second cycle shown by the red dotted line is $^{16}O(p,\gamma)^{17}F(p,\gamma)^{18}Ne(\beta^{+}\nu)^{18}F(p,\alpha)^{15}O(\beta^{+}\nu)^{15}N(p,\gamma)^{16}O$ [6]. Here (p,γ) indicates the capture of a proton and release of a gamma ray, (p,α) indicates the capture of a proton and release of ^{4}He and $(\beta^{+}\nu)$ denotes a beta decay.

This super-Eddington luminosity (Eddington luminosity is the luminosity at which outward radiation pressure balances inward pull due to gravity) causes rapid expansion and ejection of the envelope [27].

Spectroscopic studies of the ejecta of several novae have shown a substantial enhancement in helium, carbon, nitrogen, oxygen, neon, sodium, magnesium and aluminum relative to solar composition [18] (See Table (3.1)). These novae are thought to have been enhanced to higher than solar metallicity in order to synthesize the significant abundances of the heavier elements observed during the explosion. If the envelope is significantly enriched over solar abundance in CNO isotopes, the TNR will start earlier and run faster than in an envelope with sparse CNO [4]; as a result a fast nova occurs. A fast nova is defined as a nova that reaches its maximum brightness within a few hours and fades by two orders of magnitude within 25 days [4]. A critical pressure of 10^{20} dyne/cm^2 must be reached at envelope core interface for a fast nova to occur [56].

The TNR on a CO white dwarf is driven by energy release from the hot CNO cycle. The critical parameters are those governing the proton capture reactions on the short-lived radioactive isotopes ^{13}N, ^{17}F, and ^{18}F [26], which determine the nucleosynthesis and therefore the carbon, oxygen, and nitrogen isotopic abundance distribution in the ejecta [3]. At nova

temperatures the reaction rate of $^{13}N(p,\gamma)^{14}O$ is faster than the rate for $^{13}N(\beta^{+}\nu)^{13}C$ of the classical CNO cycle, leading to breakout from the regular CNO cycle. The new path is $^{12}C(p,\gamma)\,^{13}N(p,\gamma)^{14}O$. The proton captures are halted at ^{14}O since ^{15}F is proton unbound. The cycle continues with a slow beta decay $^{14}O(\beta^{+}\nu)^{14}N(p,\gamma)\,^{15}O(\beta^{+}\nu)^{15}N(p,\alpha)^{12}C$ (see figure 3.2). This cycle is limited by the proton drip line (proton capture on ^{14}O would give a product unstable against proton emission) and the slowest decays occur for ^{14}O and ^{15}O. At higher temperature a second cycle emerges, initiated by a proton capture on ^{16}O: $^{16}O(p,\gamma)^{17}F(p,\gamma)^{18}Ne(\beta^{+}\nu)^{18}F(p,\alpha)\,^{15}O$ (see Figure 3.3). This cycle is also limited by the proton drip line. Since ^{19}Na is proton unstable, no further proton capture can occur on ^{18}F.

In both cycles the conversion timescale for fusion of four hydrogen nuclei to helium and the amount of energy generation are temperature independent and determined by the β-decay lifetime of the waiting-points isotopes $^{14}O(t_{1/2}=70.59s)$, $^{15}O(t_{1/2}=122s)$, and $^{18}Ne(t_{1/2}=1.67s)$ [3]. Waiting point isotopes are isotopes where relatively large abundance due to the wait for a slow reaction (β decay in this case). The waiting point isotopes are characterized by low or negative Q-values for proton capture, making those reactions unlikely [62].

Table 3.1 Heavy-Element Abundances in Novae

		Mass Fraction										
Object	**Date**	**H**	**He**	**C**	**N**	**O**	**Ne**	**Na**	**Mg**	**Al**	**Si**	**S**
RR Pic	1925	0.53	0.43	0.0039	0.022	0.006	0.011	…	…	…	…	…
Hr Del	1967	0.45	0.48	…	0.027	0.047	0.003	…	…	…	…	…
T Aur	1891	0.47	0.4	…	0.079	0.079	…	…	…	…	…	…
V1500 Cyg	1975	0.49	0.21	0.07	0.075	0.075	0.023	…	…	…	…	…
V1668 Cyg	1978	0.45	0.23	0.047	0.14	0.14	0.0068	…	…	…	…	…
V6993Cr A	1981	0.29	0.32	0.0046	0.08	0.08	0.17	0.0016	0.0076	0.0043	0.0022	…
DQ Her	1934	0.34	0.095	0.045	0.23	0.23	…	…	…	…	…	…
V1379 Aql	1982	0.053	0.085	0.031	0.095	0.095	0.47	…	0.0092	…	0.0012	0.19

Source: J.W Turan & Livio, Ap.J., 308: 721-727 (1986)

The mass fraction of a particular element is the fraction of nucleons of in the sample, which in this case is the nova envelope, which are of that species of element. The mass fraction of an element is related to the abundance of that element by the element's atomic mass such that mass fraction equals abundance multiplied by the atomic mass [65] .

For TNR at the surface of an ONeMg white dwarf, additional energy is generated by proton capture reaction sequences triggered on the initial ^{20}Ne and ^{24}Mg abundances [26]. As a result, two new groups of reactions emerge: a NeNa cycle and a MgAl cycle (see figure (3.3)). These two new cycles have a particular interest because of ^{26}Al and ^{22}Na production which are potentially observable by γ-ray telescopes [39]. The reaction path is characterized by cyclic burning all the way up to sulfur and calcium [26]. The reaction rates in these cycles help to determine the energy production as well as the final abundances of isotopes.

ONeMg novae have been considered as possible sites for break out of the CNO cycle. Breakout reactions are nuclear reactions that bridge the proton unbound drip line isotopes [3]. Breakout of the CNO cycle involves α captures on the CNO waiting-point isotopes. Temperatures greater than 0.4 GK (billion Kelvin) must be reached in order for break out to occur from the CNO cycle [3][26][50]. ONeMg novae have also been considered as possible sites for the rp process. The rp process occurs from break out of the NeNa cycle and MgAl cycle and is unlikely to proceed beyond mass-40 isotopes, even in the hottest novae.

Novae are only responsible for 0.3% of the interstellar matter in our galaxy. Theoretical and observational studies have identified novae as the

likely source of ^{13}C, ^{15}N, ^{17}O, and ^{17}F [32]. Of observed novae, 33% involve a WD in the mass range 1.2 to 1.35 solar masses, though this range represents only < 5% of the white dwarf population [18]. Such massive white dwarfs are believed to be ONeMg white dwarfs, and when they are in a binary system and become novae, their ejecta have been observed to be enriched in nitrogen, neon, silicon, sulfur, and phosporus abundances [26].

3.2 X-Ray Bursts

X-ray bursts result from accretion in a close binary similar to the nova case discussed above. However, the companion star donates mass onto a neutron star instead of a white dwarf. As matter is accreted, the density and temperature at the bottom of the accreted envelope rise, igniting the pp chain. The energy generation starts in partially degenerate matter. Further evolution of the nuclear burning on the neutron star depends on the composition of the accreting matter, the accretion rate, and the temperature of the neutron star envelope [34]. The accreted matter consists of H, He, and very small amounts of heavier elements, since binary systems involving neutron stars are thought to be old and belong to population II [34]. If the donor star is a He white dwarf, then the accreted matter does not contain hydrogen, but traces of heavy elements are still present.

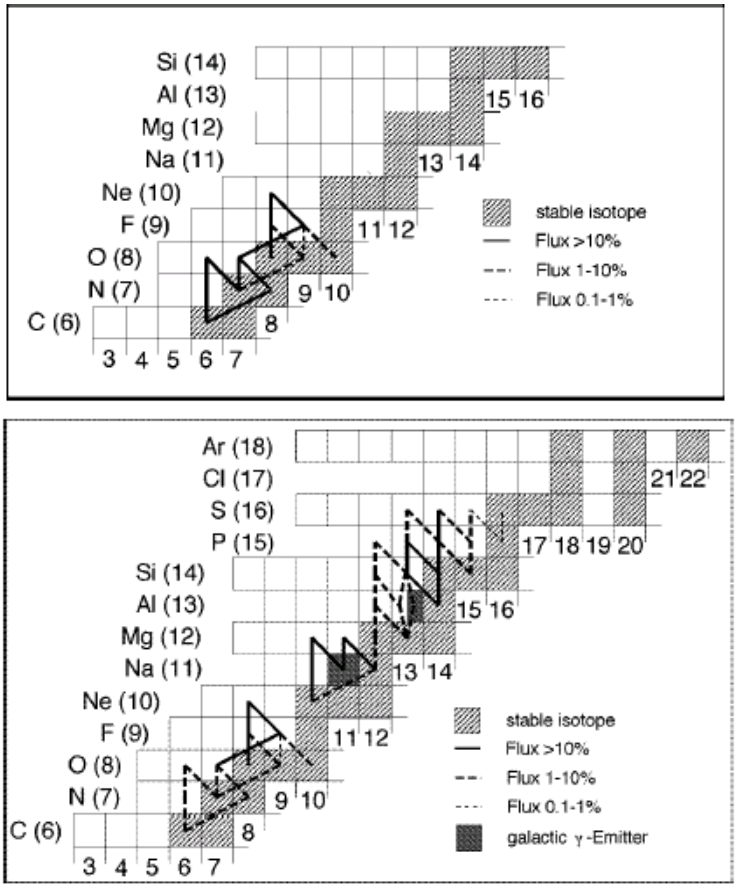

Source:M. wiescher, H. Schatz, & A.E. Champagne, Phil. Trans. R. Soc. Lond. A. 356,2105-2136(1998)

Figure 3.3 Top: the hot CNO cycles that drive the thermonuclear runaway in a C-O nova. Bottom: the reaction flow during the thermonuclear runaway in a ONeMg nova.

At low accretion rate and therefore low envelope temperature, the hydrogen and helium will burn stably via the pp chain. At very high accretion rates, both hydrogen and helium will again burn stably. At high envelope temperature and low accretion rate, the hydrogen burns via the hot CNO cycle, and the helium burns via the triple-α reaction [62]. Such burning is thermally unstable [75] and leads to thermonuclear H and He flashes, which appear as an X-ray burst.

The energy production of the hot CNO cycle is limited because of the long beta decay half lives of the CNO waiting-point isotopes. After ignition, the explosion is triggered via the rp process which releases additional energy. This process is initiated as the CNO isotopes are converted into heavier isotopes by alpha capture processes on the CNO waiting point isotopes [3] (see figure(3.4). The reaction rates of the alpha capture processes determine the conditions for the thermonuclear runaway at X-ray burst temperatures. The CNO nuclei are processed to heavier isotopes, and the further processing of these isotopes feeds the luminosity of the burst. Peak temperatures up to 2GK can be reached before the degeneracy is lifted.

This temperature is high enough to ignite the rp and αp processes. The energy release during this latter process drives the runaway [27]. The

total energy release during the burst is in the range of 10^{39}-10^{40} ergs, on a timescale that varies between 10 seconds to 100 seconds [40], and may be repeated after hours or days. On timescale of 10s to 100s, the rp process proceeds all the way up to ^{56}Ni. Energy production is halted at this waiting point, and further processing is inhibited by a strong photodisintegration reaction ^{57}Cu(γ,p)^{56}Ni (see fig 3.4). Eventual breakout occurs via a two proton capture process, ^{56}Ni(2p,γ)^{58}Zn. The two-proton capture process will also face strong competition from photodisintegration. This reaction could initiate a second burst by subsequent rp processing along the N=Z line up to iodine [26]. The path beyond ^{56}Ni is restricted by the proton drip line, which runs close to the N=Z line; thus the time scale of the rp process is dependent on the long lifetime of the beta decays. When further proton capture is suppressed, a slow down in energy production occurs. This is a result of the long lifetime of the β decays in this mass range, the proton gap of the N=Z nuclei is eventually bridged by two proton capture in the short timescale of the X-ray burst.

Recent observations have suggested that the nuclear burning is not uniform on the surface of the neutron star in an XRB. The thermonuclear runaway may be ignited at a single point and then propagate around the surface of the neutron star [33].

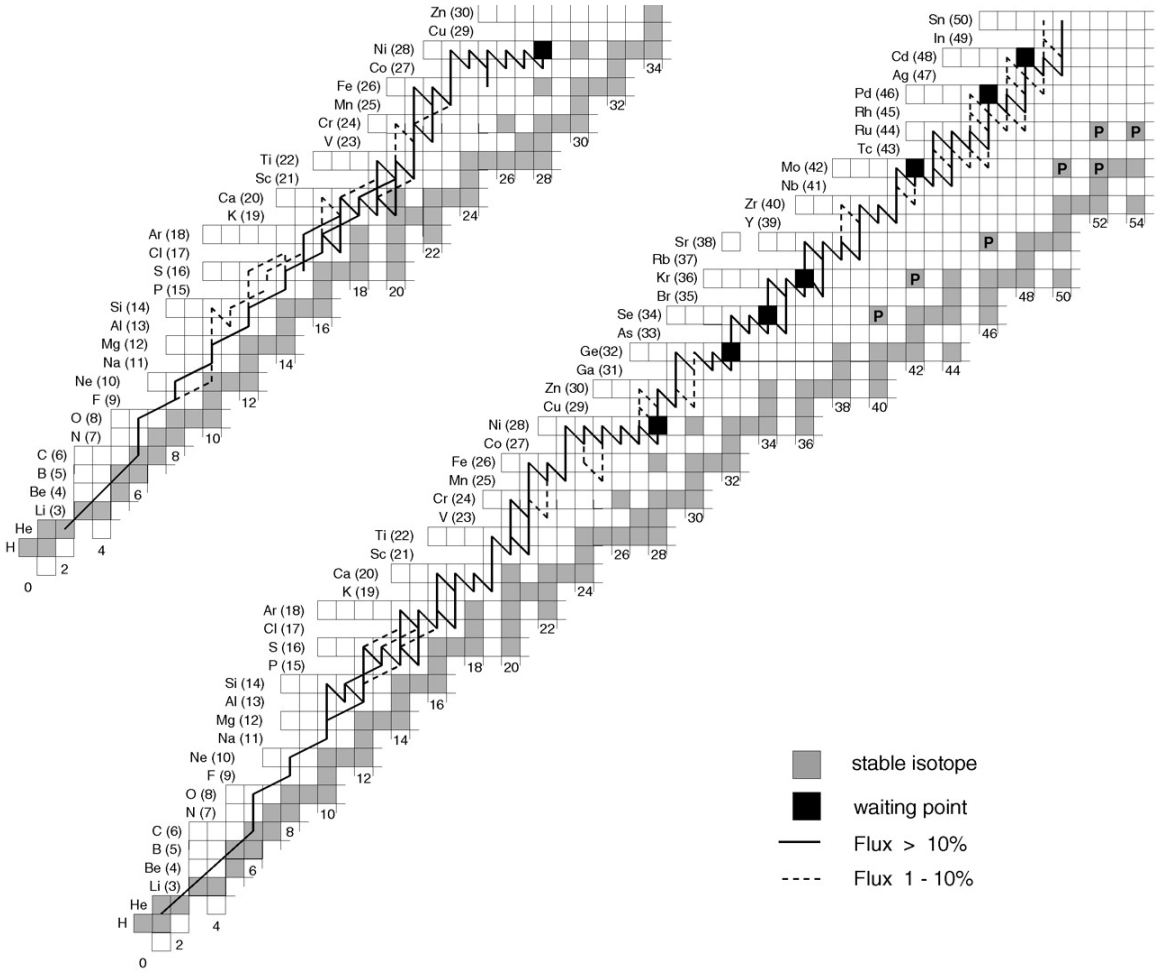

Source:F. Käppeler, F.-K Thielemann, & M. Wiescher, Annu Rev. Nucl. Part. Sci 48: 175-251 (1998)

Figure 3.4 Upper:The reaction flux intergrated over the thermonuclear runaway. Bottom: The cooling phase of an X-ray burst.

The propagation across the surface of the neutron star can occur in three different ways: (1) As a deflagration wave, (2) in a detonation wave, if the ignition density is at $\rho \geq 10^7$ g cm^{-3}, and (3) if the internal magnetic field $B_i \geq 10^{11}$ Gauss and the burning front does not detonate, convection and turbulence are suppressed and the resulting conduction wave propagates at a lower velocity $v_{flame} \approx 10^3 - 10^4$ cm s^{-1} [34].

Deflagration is an unstable convective ordinary flame front that propagates across the neutron star surface at velocity of $v_{flame} \approx 10^6$ cm s^{-1} [34]. The unstable nuclear burning has been observed [33,35,43] as brightness oscillations during the X ray burst.

This concludes our brief discussion of nucleosynthesis in novae and X-ray bursts. The next chapter will discuss the calculations of the reaction rates important in both novae and X ray bursts.

Chapter 4
Nuclear Reaction Rates and Cross Sections

The vast majority of energy on earth is produced by chemical reactions. However, it has been established for centuries that such reactions are insufficient to power the stars, since a sun powered by chemical reactions would have run out of fuel billions of years ago. As first shown by [63][see also 57], the sun and all other stars are powered by nuclear reactions. This section gives some formalism related to stellar energy production. It is divided into three parts: relating rates to cross section, the nuclear S factor, and thermal distributions and thermal averaging of the rates.

4.1 Reactions

It is possible to change the structure of nuclei by bombarding them with energetic particles [17]. A nucleus X bombarded with an energetic particle (or nucleus) a can change into a nucleus Y while emitting a particle b

$$a + X \rightarrow Y + b \tag{4.1}$$

This reaction can be written in a more compact form as $X(a,b)Y$. The projectile a and target nucleus X together represent the entrance channel,

while the emerging nuclei Y and b together constitute the exit channel. The total energy released as a result of the reaction is termed the Q value and is defined as

$$Q = (M_a + M_X - M_b - M_Y)c^2 \qquad (4.2)$$

where the $M's$ are the masses of the respective particles and c is the speed of light. A positive Q ensures a residual energy that appears as the kinetic energy of the products, which means the mass loss in the system is balanced by an increase in the kinetic energy of the final particles; this is called an exothermic reaction. An endothermic reaction is a reaction for which Q is negative. In order for an endothermic reaction to occur, the entrance channel kinetic energy must be larger than Q. The minimum energy required for a reaction to occur is called the threshold energy.

In all nuclear reactions the total energy, momentum, parity and angular momentum are conserved. The conservation of momentum guarantees that the kinetics of all nuclear reactions can be described in terms of motion of the center of momentum of the nuclear system and the motion of the particles with respect to their center of mass. The total energy or momentum can be expressed in terms of that for the center of mass system plus the energy or momentum of the motion of the center of mass itself [15].

Conservation of momentum demands that the motion of the center of mass be unaltered by the reaction [15]. Conservation of energy demands that the total energy of the reactants is equal to the total energy of the products such that the energy of the above reaction can be written as

$$E_{aX} + (M_a + M_X)c^2 = E_{bY} + (M_b + M_Y)c^2 \qquad (4.3)$$

where E_{aX} is the kinetic energy in the center of mass of a and X and E_{bY} is the kinetic energy in the center of mass of b and Y [15]. The reader is encouraged to read [15,17,24,25] for complete details on nuclear reactions.

4.2 Reaction Rates and Cross Sections

The most basic piece of information one can know about a nuclear reaction is its cross section σ. For 2 body-collisions, the cross section is the probability per pair of interacting particles that a nuclear reaction will occur between particles. The cross section is important because it can be measured directly in laboratory experiments. If we consider the reaction $X(a,b)Y$, the rate or the number of events per unit time in some volume V, is defined as

$$\frac{dN}{dt} = \int d\vec{x} n_a(p_a, \vec{x}) n_X(p_X, \vec{x}) |\vec{v}_a - \vec{v}_X| \sigma_{aX}(p_a \cdot p_X) \qquad (4.4)$$

where $n_a(p_a, \vec{x})$ is the number density (the number of particles per unit volume) of particles a with four-momentum p_a, $n_X(p_X, \vec{x})$ is the number

density of particles X with four-momentum p_X, the relative velocity $|\vec{v}_a - \vec{v}_X|$ is defined as

$$|\vec{v}_a - \vec{v}_X| = (((p_a \cdot p_X)^2 - m_a{}^2 m_X{}^2) \cdot (E_a E_X)^{-1})^{1/2} \quad (4.5)$$

For simplicity assume that all particles X are at rest and all particles a are projectiles and have velocity v. Holding the densities constant over the volume of interest, the integration over **x** yields a rate

$$r = \frac{1}{V}\frac{dN}{dt} = N_a N_X v\sigma(v) \quad (4.6)$$

where N_a and N_X are respectively n_a and n_X integrated over the volume. The number of reactions that occur in a volume is proportional to the incident flux of projectiles, $F = vN$; thus the rate r is best described as the product of the cross section area and the incident flux [14].

4.3 Thermal Distributions and Thermally Averaged Rates

The particles in any stellar gas will have a distribution of momenta that is characterized by the temperature. Thus to find the total reaction rate it is necessary to integrate equation 4.4, weighted by the momentum distribution. For gases in a normal stellar environment, the nuclei are nondegenerate and move at nonrelativistic velocities. The momentum distribution can be thought of as a velocity distribution. The gases are in

thermodynamic equilibrium and the velocities of the nuclei can be described by a Maxwell-Boltzmann velocity distribution [14],

$$\Phi(v) = 4\pi v^2 \left(\frac{m}{2kT}\right)^{\frac{3}{2}} \exp\left(-\frac{mv^2}{2kT}\right). \tag{4.7}$$

In this expression, m is the mass of the nucleus and T is the temperature of the gas. Equation 4.7 can be rewritten in terms of energy,

$$\Phi(E) \propto E \exp\left(-\frac{E}{kT}\right) \tag{4.8}$$

For the reaction in Eq. 4.1 the velocities of both X and a can be described by a Maxwell-Boltzmann velocity distribution, so the cross section averaged over the velocity distribution, denoted by <σv>, involves a double integral over the velocity distribution of both X and a, and can be written as

$$< \sigma v >= 4\pi \left(\frac{\mu}{2kT}\right)^{\frac{3}{2}} \int_0^\infty v^3(v) \exp\left(-\frac{\mu v^2}{2kT}\right) dv, \tag{4.9}$$

where μ is the reduced mass,

$$\mu = \frac{m_a m_X}{(m_a + m_X)}, \tag{4.9a}$$

and μv^2 is the center of mass energy E. Equation 4.9 can also be written as

$$< \sigma v >= \left(\frac{8}{\pi\mu}\right)^{3/2} \left(\frac{1}{kT}\right)^{-3/2} \int_0^\infty \sigma(E) E \exp\left(-\frac{E}{kT}\right) dE \tag{4.10}$$

and the total reaction rate can be written as

$$r = N_a N_X \left(\frac{8}{\pi\mu}\right)^{3/2} \left(\frac{1}{kT}\right)^{-3/2} \int_0^\infty \sigma(E) E \exp\left(-\frac{E}{kT}\right) dE \qquad (4.11)$$

This equation describes the reaction rate at any given stellar temperature T. As the star evolves, its temperature changes; hence the reaction rate must be calculated for the temperature of interest [14].

4.4 The Astrophysical S factor

Nuclear reactions of various types can occur in stars. The first division of types is between charged particle reactions and neutron-induced reactions. The physical distinction between the charged particle reactions and the neutron-induced reactions is the Coulomb barrier suppression for the former, and the need for a stellar neutron source in the latter. The primary applications that we will make involve charged particles. Charged particle reactions can be further classified into two more or less distinct classes known as compound nucleus reactions and direct capture reactions.

4.4.1 Nonresonant Cross section

For nuclear reactions involving direct capture, the projectile may interact with the target nucleus at it passes without forming a long-lived intermediate state and the timescale for the reaction is generally comparable to the time for the projectile to cross the diameter of the target nucleus

($\sim 10^{-22}$ s). Such reactions are called nonresonant reactions. For charged-particle reactions Gamow [15] showed that the probability for two particles of charge Z_1 and Z_2 traveling toward each other with velocity v to overcome their Coulomb electrostatic repulsion is proportional to the factor

$$P \propto \exp(-(2\pi Z_1 Z_2 e^2/\hbar v)) \qquad (4.13)$$

Since the reaction cannot happen unless particles overcome this repulsion, the cross section is proportional to P. In the range between 25 keV and 55 keV, which is the typical stellar energy range (the range of kinetic energies corresponding to most probable velocities in the gas), P varies rapidly with the energy. To separate this dependence (remembering that $\pi\lambda^2$ is inversely proportional to E), we can parameterize $\sigma(E)$ as

$$\sigma(E) = S(E)E^{-1}\exp(-(2\pi Z_1 Z_2 e^2/\hbar v)) \qquad (4.14)$$

which can be rearranged to solve for the parameter S(E),

$$S(E) = \sigma(E)E\exp(-(2\pi Z_1 Z_2 e^2/\hbar v)) \qquad (4.15)$$

which is the astrophysical S factor, containing all the strictly nuclear effects of the cross section. For nonresonant reactions S(E) varies smoothly and slowly with energy. S(E) can be estimated by experimental cross section measurements made at higher energies than those of a stellar environment, and extrapolated to the lower energies that are relevant to stellar

environments. For stellar explosions, the cross section is often measured directly at the energy of interest.

If we insert equation 4.14 into equation 4.11, we immediately see that $\langle\sigma v\rangle$ involves a sharp competition between the effect of the Maxwell-Boltzmann distribution and that of the Gamow barrier penetration factor. Since the factor that arises from the Maxwell-Boltzmann distribution decreases rapidly with energy, while the factor that arises from the barrier penetration increases rapidly with energy, their product (known as the Gamow window) is strongly localized in energy [16]. Thus only charged-particle reactions that fall within the relevant Gamow window occur with significant probability.

For reactions involving a compound nucleus the story is quite different. The reaction $X(a,b)Y$ may be viewed as an intermediate state W, such that

$$a + X \rightarrow W \rightarrow Y + b \qquad (4.1a)$$

The physical picture is that X and a will form an unstable compound nucleus W that will decay into final states Y and b. This intermediate state can occur only if the energy of the entrance channel is equal to the energy of the compound nucleus, which occurs for all excited energies that are above the threshold energy of the reaction.

The compound nucleus is transient, but it exists much longer than the time it takes the nucleons to cross the nucleus [14]. On that crossing timescale, it is long-lived. Nucleons in the compound nucleus have states that are characterized by finite energy widths, quantized angular momenta, and definite parities. These states in the compound nucleus are said to be quasistable. They are similar to the bound eigenstates, but they are eigenstates of the compound nucleus. Transitions between these states occur because of interaction terms in the complete Hamiltonian[15], and these transitions cause each state to have a finite lifetime τ, or equivalently a finite energy width by $\Gamma=\hbar/\tau$, such that a long lifetime implies a small energy width and a short lifetime implies a large energy width. We can describe $<\sigma v>$ in the center of mass system in terms of these energy widths,

$$\sigma_{ab}(E) = \pi g \lambda^2 \Gamma_a \Gamma_b f(E) \Gamma^{-2} \qquad (4.12)$$

Here Γ_a is the entrance channel width, Γ_b is the exit channel width, and $\Gamma=\Sigma_i\Gamma_i$. The geometrical factor $\pi\lambda^2$ is inversely proportional to the energy of the particle. Since λ is the DeBroglie wavelength, $\pi\lambda^2$ is a measure of the spatial localization of the quantum wave packet. The function $f(E)$ contains details of the form (either resonant or nonresonant) of the reaction, and g is a

statistical factor that contains information on the spins of the projectile, target, and compound nucleus.

4.4.2 Breit-Wigner Resonances

If the intermediate nucleus is probed, resonances will be observed. A resonance can occur in a nuclear reaction if the kinetic energy E of the particles at infinity is just such that the total energy coincides with one of the quasistationary states of the compound nucleus [15]. The resonance cross section is often expressed in the Breit-Wigner form,

$$\sigma(E)=g\pi\lambda^2\Gamma_a\Gamma_b((E-E_r)^2+\Gamma^2/2)^{-1} \qquad (4.16)$$

where E is the kinetic and E_r is the resonant energy, Γ_a is the entrance channel width, and Γ_b is the exit channel width. This is the cross section for a single isolated resonance; the total resonant cross section is a summation over all the contributing resonances. Note that such resonant cross sections are strongly dependent on the location and width of the quasistationary states in the compound nucleus. The resonance state and finite lifetime of the compound nucleus greatly affect the reaction rate.

4.5 Decay Rates

Another important reaction that occurs in stars is the decay of a particle 1 to possible final states, which we number 2,3,4 etc. The rate can be written as

$$r = \rho_1(\lambda_{12} + \lambda_{13} + \lambda_{14} + ...) \qquad (4.17)$$

where λ is decay channel rate per particle and is given in unit of 1/s, and the mean lifetime is defined as

$$\tau_{12} = < t > = \int_0^\infty \exp(-\lambda_{12} t) t dt = 1/\lambda_{12} \qquad (4.18)$$

so that the half life is

$$\tau_{1/2} = \exp(-\lambda_{12})^{1/2} = \tau_{12}{}^{1/2} = \ln_2/\lambda_{12} \qquad (4.19)$$

If there is more than one decay channel, the total rate is

$$\lambda = \lambda_{12} + \lambda_{13} + \lambda_{14} + ... \qquad (4.20)$$

and the total half life τ_{total} is

$$1/\tau_{total} = 1/\tau_{12} + 1/\tau_{13} + ... \qquad (4.21)$$

This completes our brief summary of thermonuclear reactions and rates. The interested reader is encouraged to read [14,15,60] for a more complete discussion. Now we turn our attention to nuclear reaction networks, which

describe how these rates enter into the production of elements in stellar environments.

Chapter 5
Nuclear Reaction Networks

The reactions described in chapter 4 can be divided into three categories based on the number reactants. The reactions involving a single nucleus depend on the number density of the target. These reactions include decays, electron and positron captures, photodisintegrations, and neutrino-induced reaction. For rates of reactions involving two reactants, the reaction rate depends on the density of both projectile and target nuclei. The few important three particle-process reactions, like the triple alpha process, represent a series of reaction involving unstable targets and the rate depends on the number densities for the trio of particles [67].

The number density of each nuclear species is defined as the number of particles of that species per unit volume. The rate of change in number densities can be written as a sum of contributions from reactions of the three categories explained above,

$$\frac{\partial n}{\partial t} = \sum_j N_j^i r_j + \sum_{j,k} N_{j,k}^i r_{j,k} + \sum_{j,k,l} N_{j,k,l}^i r_{j,k,l} \quad . \qquad (5.1)$$

Here the r's represent the rates and the N^i are the number of nuclei produced or destroyed by each reaction. The individual N^i are given by $N_j^i = N_i$ for the

one-nucleus reactions, $N^i_{j,k} = (N_i / N_j!N_k!)$ for the two-nuclei reactions, and $N^i_{j,k,l} = N_i/(N_j!N_k!N_l!)$ for the three-nuclei reactions. The factorials are included in the denominator to avoid over counting when identical nuclei react with each other. A negative N represents the destruction of that species and a positive N represents the creation of that species.

The number density changes as an expansion or contraction of the reacting medium occurs. The hydrodynamical changes and the nuclear changes maybe separated by writing the number density in terms of the abundance,Y, which is not affected by changes in density. The abundance Y, has units of moles per gram (mol/g) and is given by

$$Y_i = n_i / \rho N_A \tag{5.2}$$

where N_A is Avagadro's number, n_i is the number density, and ρ is the mass density. Equation 5.1 may then be expressed in terms of abundances,

$$\dot{Y} = \sum_j N^i_j \lambda_j Y_j + \sum_{j,k} N^i_{j,k} \rho N_A \langle j,k \rangle Y_j Y_k + \sum_{j,k,l} N^i_{j,k,l} \rho^2 N_A^2 \langle j,k,l \rangle Y_j Y_k Y_l \cdot \tag{5.3}$$

Here λ is the rate for one-particle interactions, $\langle j,k \rangle$ is the velocity integrated cross section for two-particles processes, and $\langle j,k,l \rangle$ is the velocity integrated cross section for the three-particles processes. Note that the particle induced reactions are dependent on the density ρ.

The energy generation and nucleosynthesis that occurs in a stellar burning environment can be simulated by nuclear reaction network calculations tailored to the temperatures and densities of the particular stellar environment. A nuclear reaction network is a set of differential equations that ties the physics of individual reactions to an abundance pattern [11]. The simulation of the nucleosynthesis in the reaction network follows the time evolution of the species abundances. The final abundance, Y, of any one species is strongly dependent on sum of the reactions that produce or destroy the species during the astrophysical phenomenon in question and is found by the integration of equation (5.3) over time

$$Y(t)=\int_0^t \dot{Y}(t')dt'. \qquad (5.4)$$

Each reaction in the network is matched by its inverse (except for the inverse of the decay rate since tracking neutrino is not necessary in this calculation). The time integrated flux between species i and j is defined as

$$F_{i,j}=\int\left[\frac{dY_i}{dt}_{(i\rightarrow j)}-\frac{dY_j}{dt}_{(j\rightarrow i)}\right]dt \qquad (5.5)$$

The energy production in nucleosynthesis can be directly determined from the fluxes and the Q values of the contributing reactions along the reaction path. The energy production is given by

$$\varepsilon = \sum_{i,j} F_{i,j} \cdot Q_{i,j} \tag{5.6}$$

Equivalently one need only consider the change in mass energy

$$\varepsilon = \sum_{i} N_A M_i c^2 \dot{Y}_i \left(MeV g^{-1} s^{-1} \right). \tag{5.6a}$$

where $M_i c^2$ is the rest mass energy of species i in MeV, and M_i can be express in terms of atomic mass excess, $M_{ex,i} = M_i - A_i m_u$ (m_u is the atomic unit, A_i is the atomic mass), since all reactions conserve nucleon number.

Reaction rates in astrophysical plasmas occur over a large span of temperature, densities, and compositions, so they have a broad range of reaction timescales. Differential equations with wide ranges of timescales are known as stiff differential equations. Stiff differential equations are unstable unless particular care is taken in their integrations. This character of the equations limits the methods that can be used to solve a nuclear reaction network. To solve the nuclear reaction network the time integration in equation 5.4 is carried out in discrete steps via backwards differentiation for stability. To evolve the abundance Y over the time interval $\Delta t,$ we finite difference Eq. 5.4 as

$$\frac{\vec{Y}(t+\Delta t) - \vec{Y}(t)}{\Delta t} = (1-\Theta)\dot{\vec{Y}}(t+\Delta t) + \Theta \dot{\vec{Y}}(t) \tag{5.7}$$

For Θ=1, Eq. 5.7 is the explicit Euler method, while for Θ=0 it is the implicit backward Euler method; both cases are accurate to the first order. The stiff equations of the network are treated as fully implicit, which means each time step can be solved by finding the zeroes of

$$\vec{Z}(t+\Delta t) \equiv \frac{\vec{Y}(t+\Delta t)-\vec{Y}(t)}{\Delta t} - \dot{\vec{Y}}(t+\Delta t) = 0 \qquad (5.8)$$

Using the Newton-Raphson method [76], a Taylor expansion of $\vec{Z}(t+\Delta t)$ with respect to $\Delta Y(=Y(t+\Delta t)-Y(t))$ yields

$$\vec{Z} = \sum \frac{\partial Z_i(t+\Delta t)}{\partial Y_i(t+\Delta t)} \Delta \vec{Y} + O(\Delta \vec{Y})^2 + \ldots \quad . \qquad (5.9)$$

The higher terms of Eq.5.9 are neglected, so solving for $\Delta \vec{Y}$, we obtain

$$\Delta \vec{Y} = \left(\frac{\partial \vec{Z}(t+\Delta t)}{\partial \vec{Y}(t+\Delta t)} \right)^{-1} \vec{Z} \qquad (5.10)$$

where $\partial \vec{Z} / \partial \vec{Y}$ is the Jacobian matrix of $\vec{Z}$. The iterations continue until $\vec{Y}(t+\Delta t)$ converges.

The accuracy of individual abundance predictions by implicit methods decreases as Δt approaches the burning time scale, which is the timescale on which an individual abundances changes. To guarantee good accuracy for the most abundant species and an acceptable accuracy for the lesser species, Δt is set equal to the slower burning time scale of any species with an

abundance greater than some cutoff. Typically, this cutoff is set at an abundance of 10^{-6}, but in this thesis a cutoff abundance of 10^{-12} is used to follow smaller abundances.

The nuclear reaction network used in this project was written by W. Raphael Hix and Friedrich-Karl Thielemann. It solves coupled differential equations for an arbitrary set of isotopes and the reactions that link them. The nucleosynthesis calculations in the network are done under precalculated temperature and density conditions. This post processing approximation assumes that the energy generation and the ejection of the accreted envelope occur at constant density and temperature over a very short time interval for both novae and X-ray bursts. While this is an acceptable approximation to a certain point, during novae and X-ray bursts the nuclear reactions that are responsible for energy generation and ejection of the accreted envelope are coupled directly to the envelope temperature and density. Thus, for novae and X ray bursts a more accurate approximation would couple the nuclear reaction network with a multidimensional hydrodynamical calculation of the temperature and density for the envelope of the nova or that X ray burst. The interest reader is encouraged to read [67] for complete details on nuclear reaction networks. The next chapter will discuss the motivation and procedure of this project.

Chapter 6
Motivation and Procedure

6.1 Motivation

Over the past decade major advances have addressed some of the most compelling questions in the field of nuclear astrophysics. Observations of galaxies, stars, or explosive events (such as novae, supernovae, X-ray bursts) have shed considerable light on the elemental and isotopic composition of stellar photosphere as well as interstellar and intergalactic medium. The astrophysical models that mimic these events require as input the rate and energy release of the relevant nuclear reactions. Furthermore a good understanding of the underlying hydrodynamics, radiation transfer, and other aspects of stellar evolution is also required. The majority of the nuclear information input to these models is based on extrapolations and theoretical models that have no firm experimental basis, while the rest of the information originates from experimental measurements.

Because radioactive nuclei play an important role in astrophysical events, information on radioactive nuclei (cross sections, nuclear masses, and other nuclear properties that form an empirical basis of astrophysical models) are very important to improve our understanding of the processes that shape our universe. Historically, the nuclear physics information

needed by astrophysical models was obtained by indirect techniques. These unreliable methods in many cases yielded reaction rates that are incorrect by orders of magnitudes. With improved astrophysical models more precise nuclear physics information is needed to improve our understanding of the processes that shape our universe. To meet the shortcomings of the previously-used indirect techniques, beams of these radioactive nuclei must be produced and directed toward targets to perform cross section measurements [26,28]. Laboratories worldwide have undertaken a new challenge to reduce the uncertainties in nuclear astrophysics [28]. For example, [65] has studied the effect of the uncertainty of the $^{17}F(p,\gamma)^{18}Ne$ reaction rate on novae, and [66] in a recent experiment has measured the $^{14}O(\alpha,p)^{17}F$ reaction rate, finding the rate to be greater by a factor of 30 from previous determinations. With the success of these recent experiments and calculations, we move forward with our project.

The goals of this project are to determine the potential effect of a new (not yet measured) nuclear reaction on the nucleosynthesis in novae and X ray bursts, and to understand the $^{14}O(\alpha,p)^{17}F$ reaction in normal system and see if this reaction is the gateway to heavy element nucleosynthesis. For example, the new reaction, $^{14}O(\alpha,2p)^{16}O$ could be measured with a

radioactive beam at Oak Ridge National Laboratory's Holifield Radioactive Ion Beam Facility, but this expenditure of effort is only worthwhile if this rate has significant astrophysical implications. Therefore we have investigated the astrophysical significance of this reaction, mainly the effect on the isotopes that are synthesized in both novae and X-ray bursts as a function of the rate of this reaction. Nucleosynthesis calculations have been carried out for the hottest zones of models for a 1.0 $M_\odot$ CO white dwarf nova, a 1.25 $M_\odot$ ONeMg white dwarf nova, a 1.35 $M_\odot$ ONeMg white dwarf nova, and a one-zone X-ray burst.

6.2 Reaction Rate Libraries

Reaction rates in our reaction library are empirically parameterized. The reaction rates are expressed as exponentials with 7 parameters. These parameters are listed as function of reactants temperature in units of 10^9 K. Thus the reaction rate is parameterized as

$$< \sigma v > N_A = Exp[J + KT_9^{-1} + LT_9^{-1/3} + MT_9^{1/3} + NT_9 + PT_9^{5/3} + Q \ln T_9]. \qquad (6.1)$$

If necessary, separate parameter expressions are provided for both the resonant and nonresonant value of the rate.

The reaction rate library contains the reaction rate parameters needed for the network. For the nova cases, it consists of the 882 reactions collected

by Thielemann and collaborators [68]. The reaction rate for $^{14}O(\alpha,p)^{17}F$, both forward and reverse, was obtained from [72]. The reaction rate parameter for $^{17}F(p,\gamma)^{18}Ne$ was obtained from [51]. Two different reaction rate libraries were maintained in this project. The first library contains only the 882 reactions; from here on it will be termed the "old case". In the second library the $^{14}O(\alpha,2p)^{16}O$ rate is added, thus we now have 883 reactions, this library will be referred to as the "new case".

For the XRB case, the reaction rates library contains 5598 reactions. The first reactions in the network were collected from Thielemann and collaborators [68]. Additional strong and electromagnetic reaction rates were calculated by [69]. The weak reaction rates are those of [62] and [77], collected from two sources, [70] and [71]. Two different reaction rate libraries were also maintained for the XRB case. The first library contains only the 5598 reactions, from here on it will be termed the "old case". In the second library the $^{14}O(\alpha,2p)^{16}O$ rate is added, thus we now have 5599 reactions. This library will be referred to as the "new case".

6.2.1 Reactions

In this computer experiment we alter two reaction rates and study their impact on the final abundances and energy production. These reaction

rates are amenable to study with radioactive beams and it has been suggested that they are very important for nuclear astrophysics in explosive environments such as novae and X ray bursts.

6.2.2 The $^{14}O(\alpha,p)^{17}F$ Reaction

This reaction is one of the breakout paths from the hot CNO cycle to the rp process that occurs in hot XRB and possibly the hottest novae [3]. It is thought to be the trigger reaction for X-ray bursts. It is the beginning of a sequence of (α,p) and (p,γ) reactions that at high temperature comprise the αp process [28]. It is thought to be responsible for the peak energy generation during the XRB [27]. The reaction rate used for this reaction is part of a compilation by [72] and was estimated [55] for the $J^{\pi}= 1^{-}$ state of ^{18}Ne at an excitation energy of 6.125 MeV. The first term is a nonresonant contribution determined from the tails of nine resonances, the second and third terms are resonance contributions at resonance energies of 1.3 and 2.5 MeV (LAB). The remainder of the terms are derived from contributions of the other seven resonances augmented by Hauser-Feshbach theoretical reaction rates for $T_9>5.0$ GK, in view of a probably higher density of states in that regime [72]. The rates used for this calculation were obtained by taking the time-inverse reaction of the above reaction. A recent experiment

at Oak Ridge National Laboratory has measured this rate to be 30 times faster than the currently accepted rate [66].

6.2.3 The $^{14}O(\alpha,2p)^{16}O$ Reaction

This reaction provides an additional destruction mechanism for ^{14}O, potentially affecting the hot CNO or αp process. Since its rate is unknown at this time, we used the full strength of the reaction ^{14}O (α,p) ^{17}F for ^{14}O (α,p) ^{16}O as a baseline in the calculations. This reaction is based on the possible detection of a 2-proton decay out of ^{18}Ne [49]. If this reaction has any astrophysical implications, it could potentially be measured with radioactive beam at ORNL's Holifield Radioactive Ion Beam Facility.

6.3 Hydrodynamic Profiles

The network used in the calculations, detailed in chapter 5, follows a pre-calculated thermodynamic history drawn from hydrodynamic models. In hydrodynamic modeling of novae and X ray bursts, the enveloped is divided into concentric shells or zones. Each zone follows its own hydrodynamic profile.

These hydrodynamic profiles provide the temperature and density history within each zone as a function of time. Starrfield and collaborators generated all of the zones for the three novae studied in this thesis [47,53].

Figures 6.1-6.3 show the thermodynamic trajectories of the hottest zone of the three novae. The most extreme temperatures and densities are reached in the 1.35 $M_{\odot}$, which produces a faster and more violent nova. The 1.35 $M_{\odot}$ case will also cool faster than the other two cases as a result of its rapid expansion. The rapid cooling plays a significant role in the differing nucleosynthesis between the two ONeMg novae. The coolest WD is the 1.0 $M_{\odot}$ WD.

The hydrodynamic profile for the X ray burst was obtained for a one-zone model from [27]. Figure 6-4 shows the trajectory for the XRB. The temperature and density found in the XRB are even more extreme than those found in the 1.35 $M_{\odot}$ nova case. The XRB also cools faster than the 1.35 nova.

6.4 Initial Abundances

In order to produce a set of final abundances, the network must be provided a set of initial abundances that mimics the conditions on a white dwarf's surface prior to the nova and on a neutron star's surface prior to the X-ray burst. The initial abundances for novae are assumed to be a mixture of material from the donor star and the underlying WD [3,53]. For the 1.0 $M_{\odot}$ CO WD, the solar material from the donor star [46] was enriched by 50% with white dwarf matter, an equal mix of ^{12}C and ^{16}O with traces of

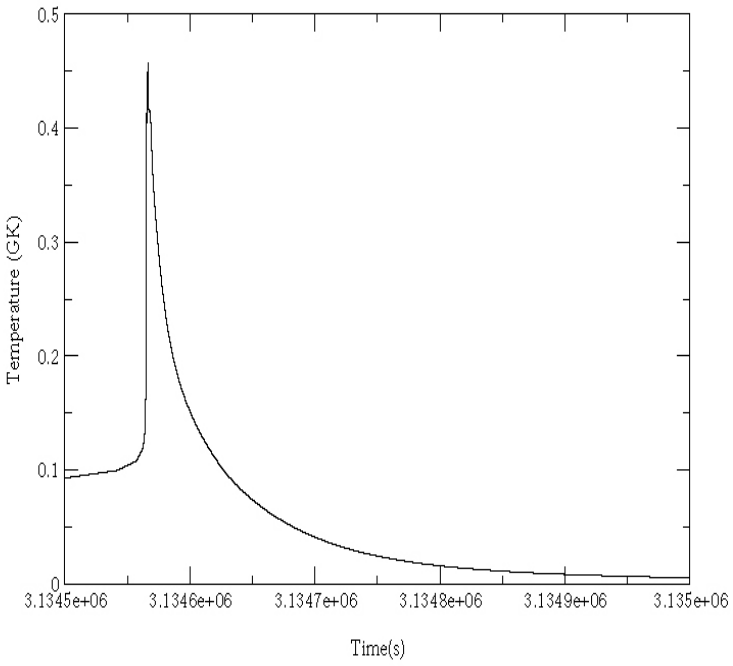

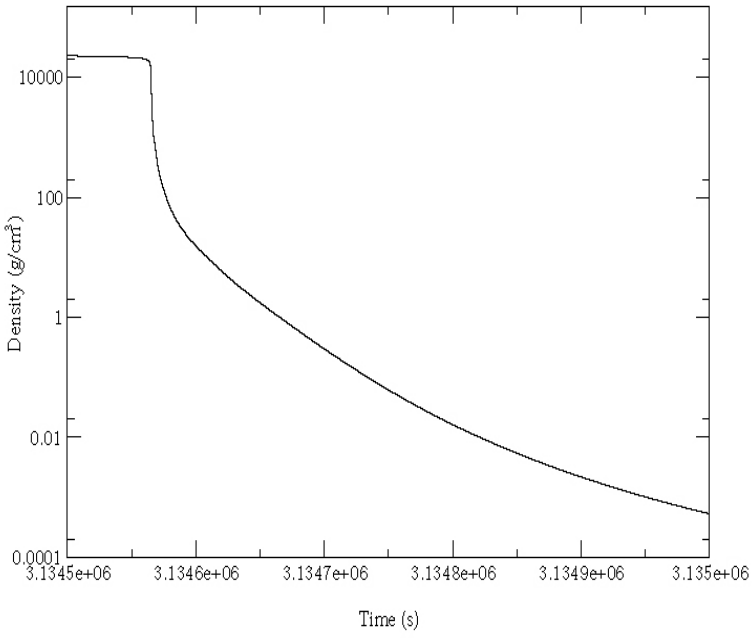

Figure 6.1 Hydrodynamic trajectory for the hottest zone of 1.35 $M_{\odot}$WD nova.

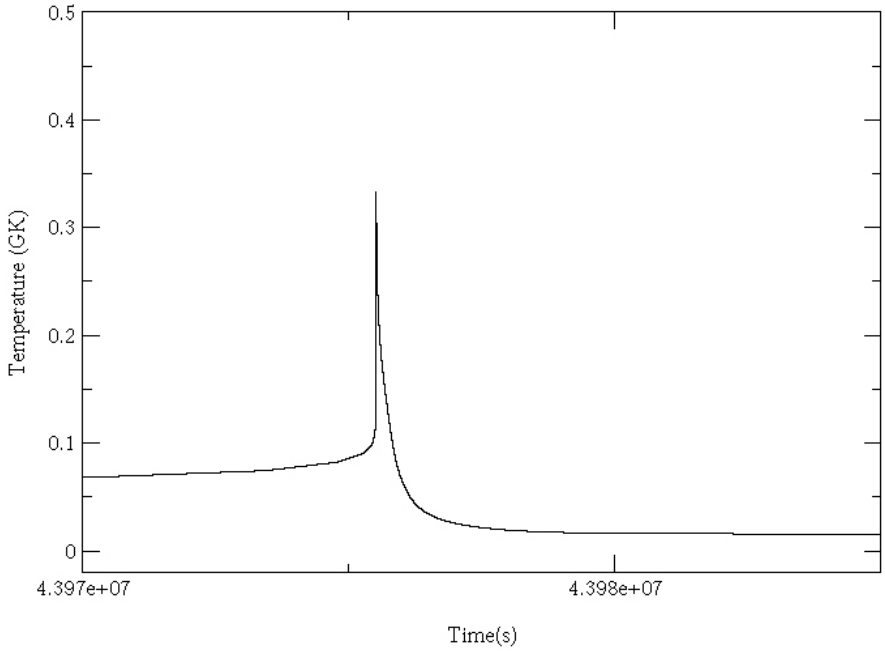

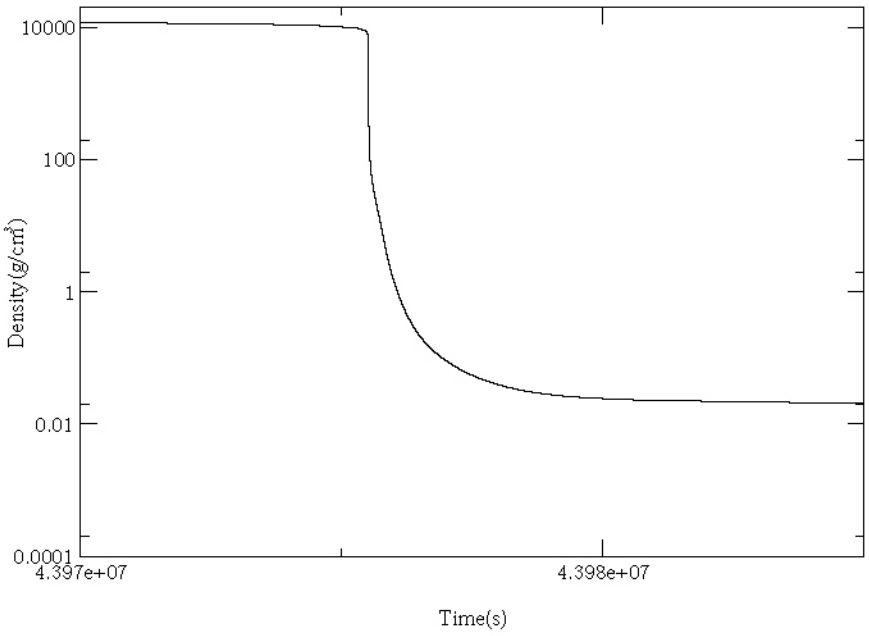

Figure 6.2 Hydrodynamic trajectory for the hottest zone of 1.25 $M_{\odot}$ WD nova.

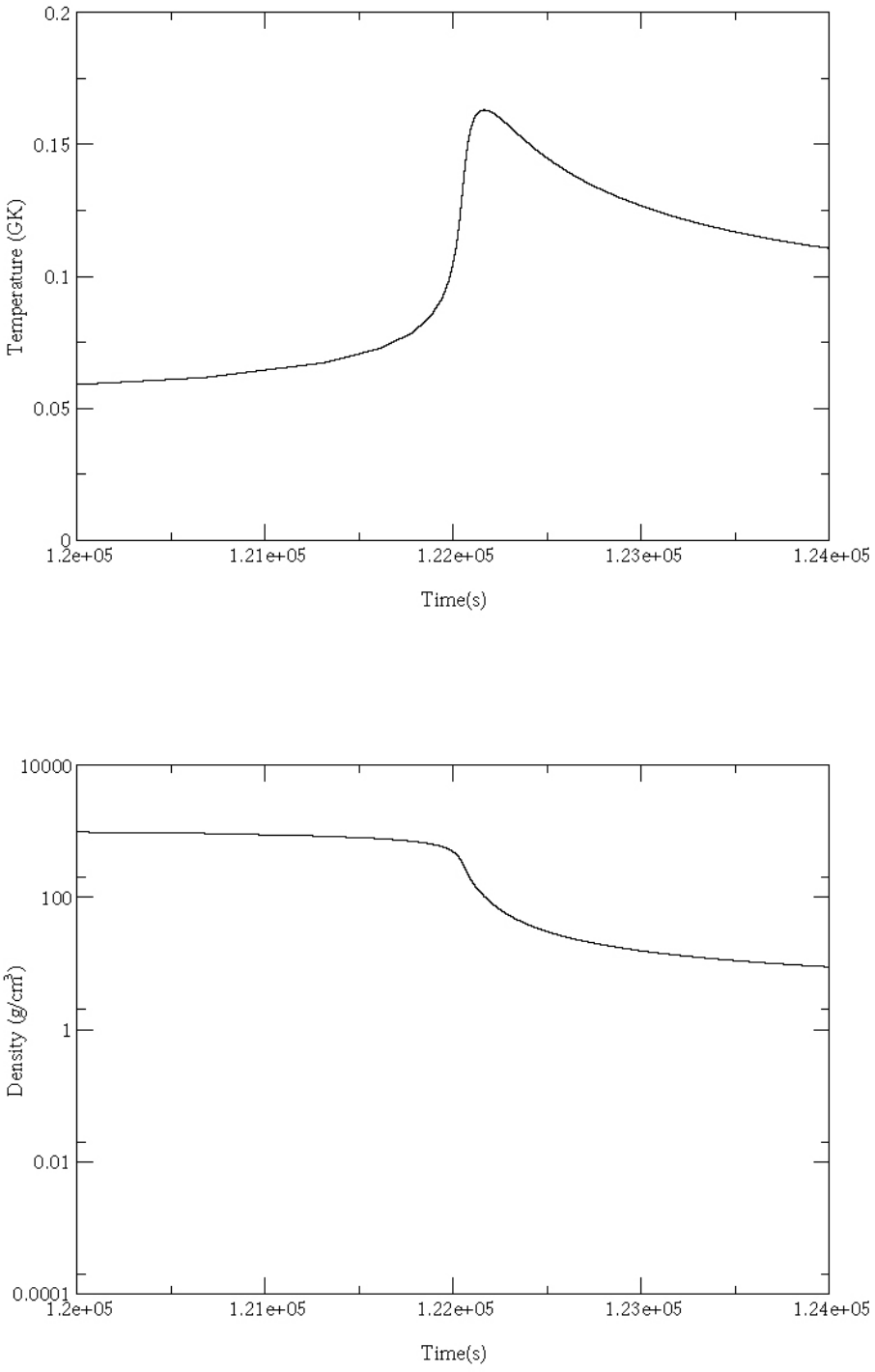

Figure 6.3 Hydrodynamic trajectory for the hottest zone of 1.00 $M_{\odot}$ WD nova.

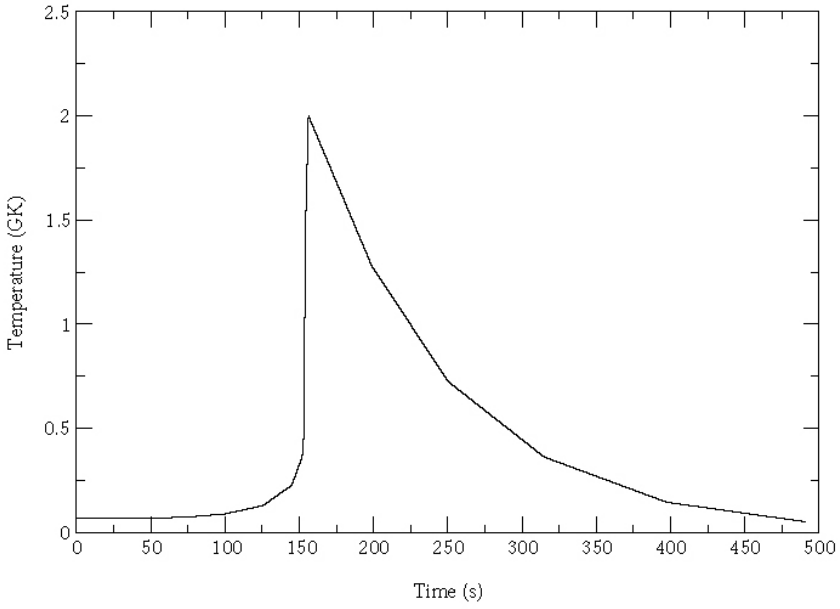

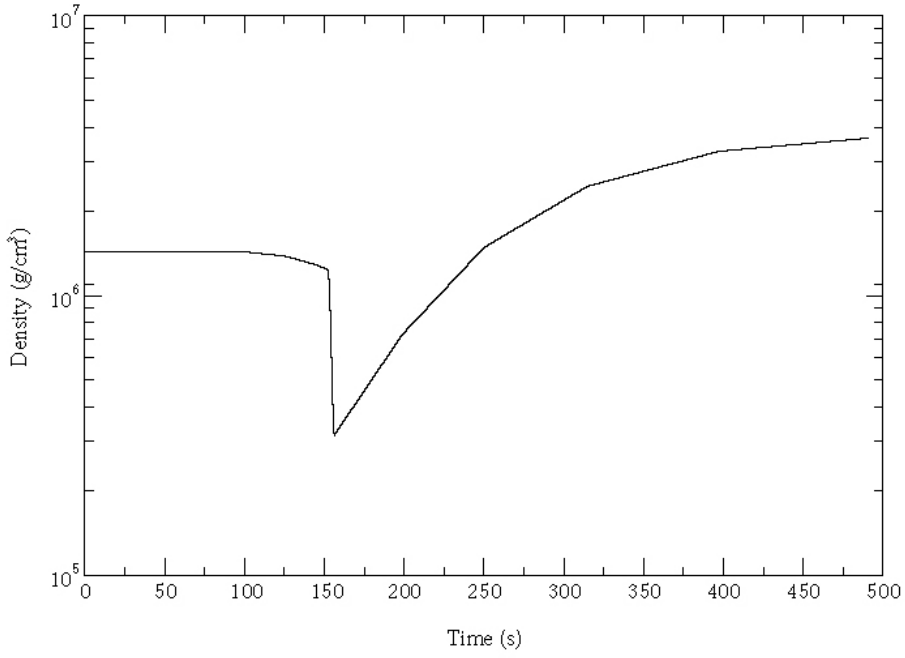

Figure 6.4 Hydrodynamic trajectory for one zone of an X-ray Burst

^{22}Ne. For the 1.25 $M_{\odot}$ and the 1.35 $M_{\odot}$ ONeMg WD, a mixture of the solar material from the donor star and a 50% enrichment of oxygen, neon and magnesium rich material from the underlying WD was assumed [53]. The initial abundances for the NS are assumed to be solar because the accreted matter is thought to lie atop of helium.

6.5 Network Modifications

I wrote a FORTRAN interface that allows the user to choose any reaction in the reaction rate library and change the J component of equation 6. 1. Since the expression is an exponential expression change the first parameter results in a temperature-independent change in the rate. In the present work the rate is changed at runtime by multiplying the existing rate by a scaling factor. The altered rate is then used by the network for that particular run.

6.5.1 Methods

To examine the whole range of possible values for the unknown ^{14}O (α,2p)^{16}O rate, it and the ^{14}O (α,p) ^{17}F rate were varied over a range of 12 orders of magnitude. The magnitudes varied from negligibly small (10^{-9}) to equal to the known rate of ^{14}O (α,p) ^{17}F, and finally to exceeding the known rate of ^{14}O (α,p) ^{17}F by a factor of 10^{3}. FORTRAN codes as well as

MATLAB codes were written to compare outputs of different runs of the network. This was done to determine the correlation between the output abundances, energy production, fluxes (flow diagram) and the input reaction rates for all species produced.

The next chapters will show the result of the simulations run with each nova and X-ray burst profile. The data are presented in terms of flow diagrams and plots of abundance ratios versus atomic mass for the nova cases. For the X-ray burst case, the data are presented in terms of flow diagrams, energy production versus time plots, and abundance ratios versus atomic mass plots.

.

Chapter 7
Results for Nova Cases

As we have established in chapter 3, to break out of the CNO cycle, alpha burning on a CNO waiting point nuclei must be initiated. Breakout may possibly occur in the hottest novae. The rate of one of the dominant breakout paths, $^{14}O(\alpha,p)^{17}F$, has been varied over a range of 12 magnitudes for three novae, to determine the sensitivity in model predictions to the $^{14}O(\alpha,p)^{17}F$ rate. The expected result in the final abundances is a decline in the higher mass abundances when this rate is greatly reduced (multiplied by 10^{-9}), since this reaction may primarily be responsible for enabling the processing of isotopes with ≤ 20 into higher mass isotopes. As the rate is varied artificially, the differences in abundance ratios and reaction flows are studied. The unknown rate $^{14}O(\alpha,2p)^{16}O$ was varied in the same manner. Since the "reference" value of this rate is unknown, we assume the value of the accepted $^{14}O(\alpha,p)^{17}F$ rate with which it shares the same entrance channel ($^{14}O+\alpha$).

7.1 Stimulations on 1.35 $M_\odot$ ONeMg WD Nova

The 1.35 $M_\odot$ ONeMg WD nova is the most energetic nova model we considered. Figures 7.1-7.3 are the reaction flow diagrams that correspond

to the currently accepted $^{14}O(\alpha,p)^{17}F$ reaction rate and the $^{14}O(\alpha,p)^{17}F$ reaction rate multiplied by factors of 10^{-9} and 10^{3}. Figure 7.4 is the ratio of the final abundances produced by the network when the $^{14}O(\alpha,p)^{17}F$ rate is enhanced by a factor of 10^{3} to the final abundances produced by the network with the accepted $^{14}O(\alpha,p)^{17}F$ reaction rate; figure 7.5 is the ratio of the final abundances produced by the network when the $^{14}O(\alpha,p)^{17}F$ rate is reduced by a factor of 10^{-9} to the final abundances produced by the network with the accepted $^{14}O(\alpha,p)^{17}F$ reaction rate. Each abundance ratio is plotted versus the atomic mass.

Figure 7.1 shows the reaction flow formed using the currently accepted rate of $^{14}O(\alpha,p)^{17}F$. As discussed in chapter 3, the hot CNO, the NeNa and MgAl cycles are evident. When the $^{14}O(\alpha,p)^{17}F$ reaction rate is slowly enhanced by factors of 10 until saturation 10^{3}(figure 7.2), there is no noticeable changes in the reaction flow. The ratio of abundances (figure 7.4) for the case with an enhancement of 10^{3} reveals a difference of less than 1% in the final abundances. Enhancing the $^{14}O(\alpha,p)^{17}F$ rate does not affect the flow of matter in the network. As the $^{14}O(\alpha,p)^{17}F$ rate is slowly reduced by factors of 10 until a factor of 10^{-9} is reached, that case shows no distinction in the final abundances.

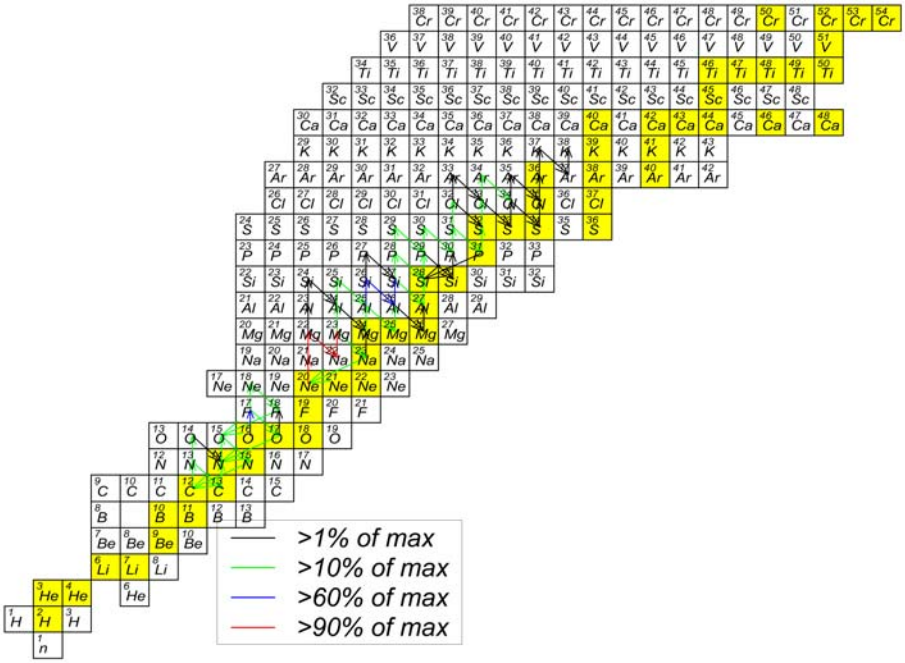

Figure 7.1. Reaction flow during the explosive burning of the ONeMg nova.

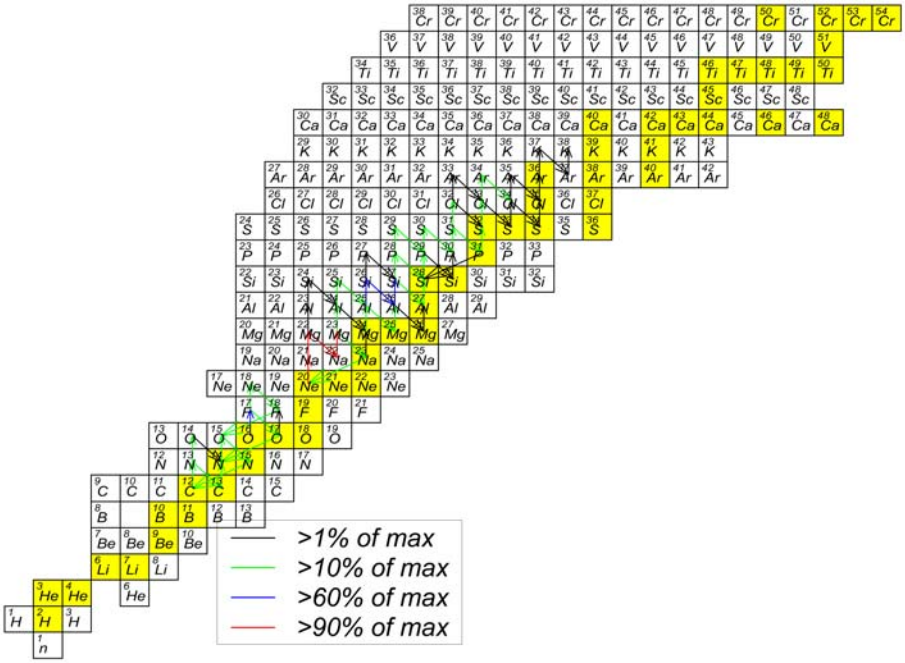

Figure 7.2. Flow with the $^{14}O(\alpha,p)^{17}F$ reaction rate reduced by a factor of 10^{-9} to the accepted $^{14}O(\alpha,p)^{17}F$ rate.

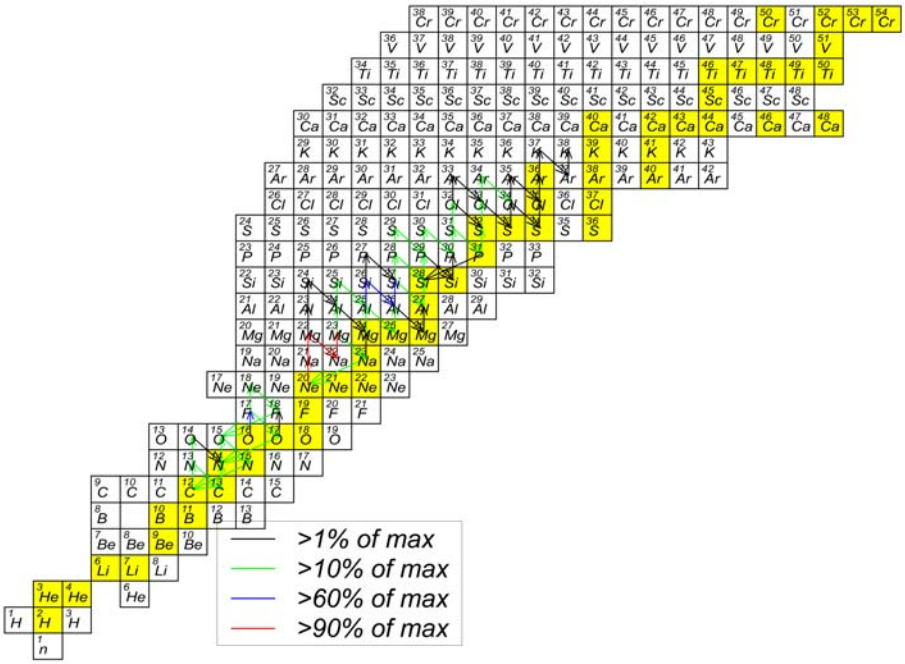

Figure 7.3. Flow with the $^{14}O(\alpha,p)^{17}F$ reaction larger by a factor of 10^3 to the accepted $^{14}O(\alpha,p)^{17}F$ rate.

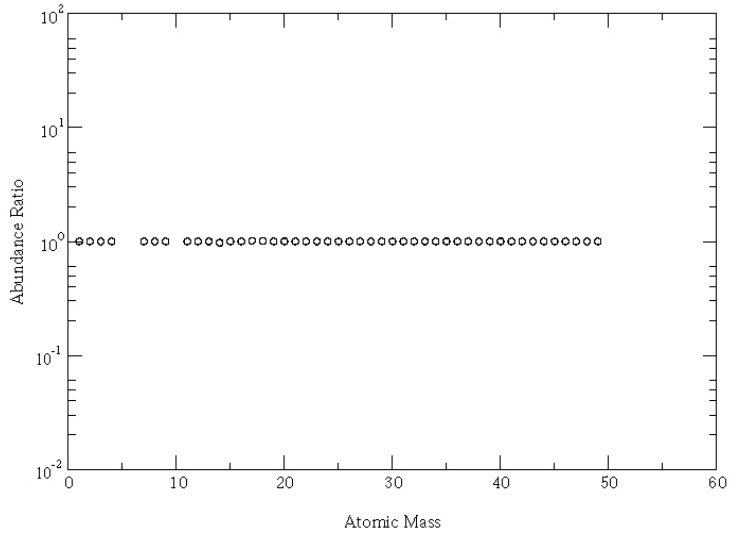

Figure 7.4. The final abundance ratio as a function of atomic mass when the $^{14}O(\alpha,p)^{17}F$ rate is a factor of 100 larger than the accepted $^{14}O(\alpha,p)^{17}F$ rate. There is no significant difference in the final abundances.

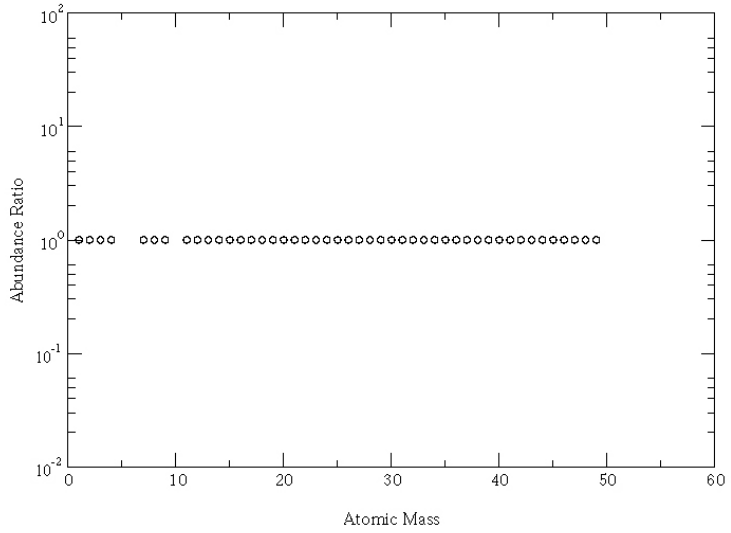

Figure 7.5. The final abundance ratio as a function of atomic mass when the $^{14}O(\alpha,p)^{17}F$ rate is reduced by a factor of 10^{-9} relative to the accepted $^{14}O(\alpha,p)^{17}F$ rate. There is no significant difference in the final abundances difference in the synthesizing of matter in the case of the 1.35 $M_{\odot}$ ONeMg nova.

The results are the same as those obtained using the accepted rate (see figure 7.3 for the reaction flow and 7.5 for abundance ratio). Reducing the rate for $^{14}O(\alpha,p)^{17}F$ does not make any significant difference in the final abundances.

The reaction $^{14}O(\alpha,2p)^{16}O$(rate unknown) when followed by $^{16}O(p,\gamma)^{17}F$ reaction, could result in a very similar element production as the $^{14}O(\alpha,p)^{17}F$ reaction. Figures 7.6-7.8 are reaction flow diagrams corresponding to the unknown$^{14}O(\alpha,2p)^{16}O$ reaction rate being reduced by a factor of 10^{-9}, being set equal to the accepted $^{14}O(\alpha,p)^{17}F$ rate, and being enhanced by a factor of 10^{3}, respectively. Figures 7.9-7.11 plot the ratio of final abundances produced by the network with the unknown $^{14}O(\alpha,2p)^{16}O$ rate to the final abundances produced by the network with the accepted $^{14}O(\alpha,p)^{17}F$ rate for the three cases described above. The final abundance ratios are plotted versus the atomic mass. Figure 7.6 shows the flow diagram for the case with the unknown rate reduced by a factor of 10^{-9}. It is the same as the flow diagram found using the currently accepted $^{14}O(\alpha,p)^{17}F$ reaction rate (Figure 7.1). Also, no significant change is noticed in the final abundant ratio (figure 7.9). The unknown $^{14}O(\alpha,2p)^{16}O$ rate was then enhanced by factors of 10 until the unknown $^{14}O(\alpha,2p)^{16}O$ reaction rate is set equal strength in to the known $^{14}O(\alpha,p)^{17}F$ rate. Figure 7.7 shows that

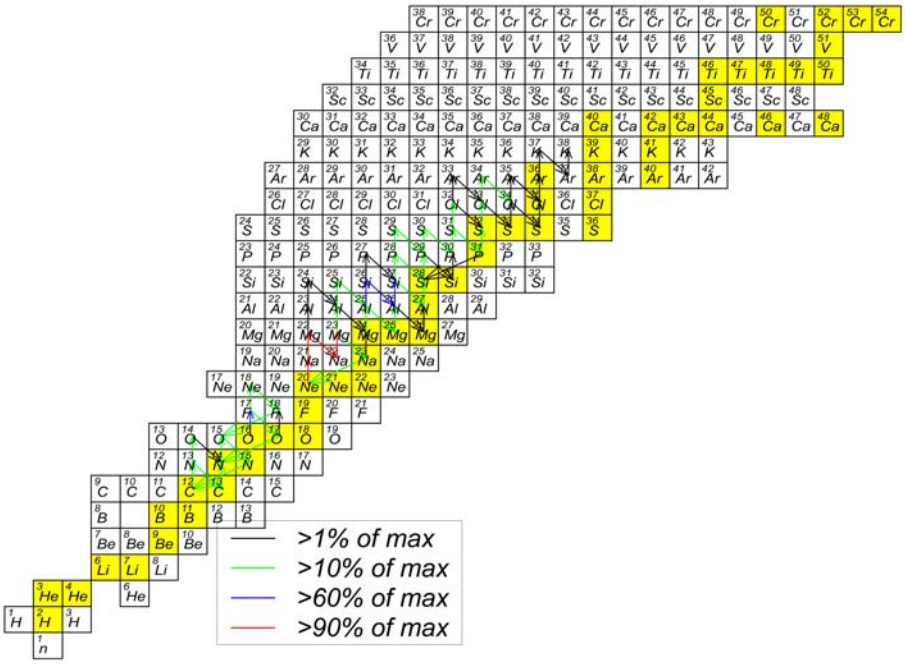

Figure 7.6. Flow with the $^{14}O(\alpha,2p)^{16}O$ reaction rate reduced by a factor of 10^{-9} to the accepted $^{14}O(\alpha,p)^{17}F$ rate.

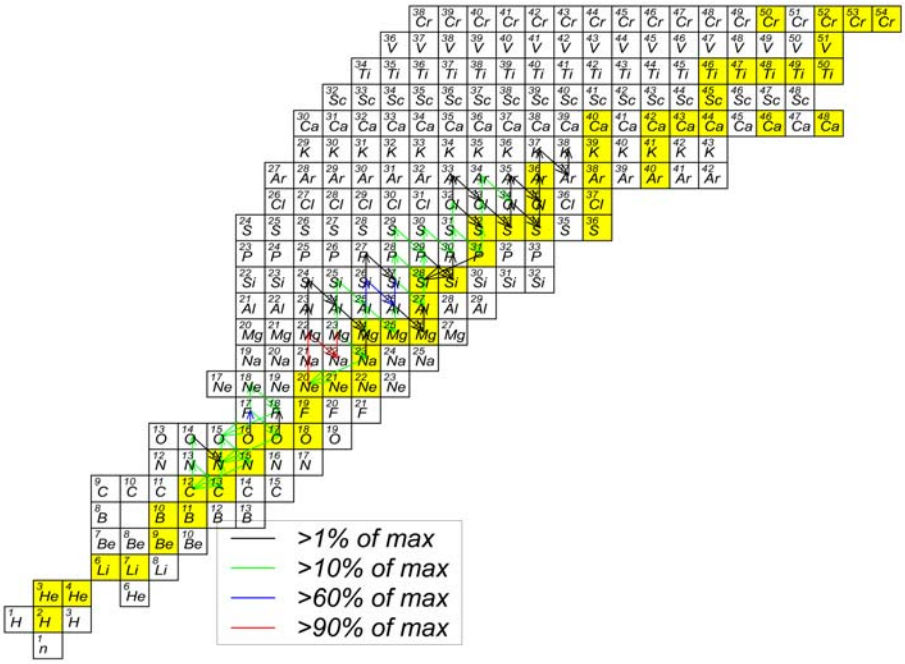

Figure 7.7. Flow with the $^{14}O(\alpha,2p)^{16}O$ reaction rate is equal in strength to the accepted $^{14}O(\alpha,p)^{17}F$ rate.

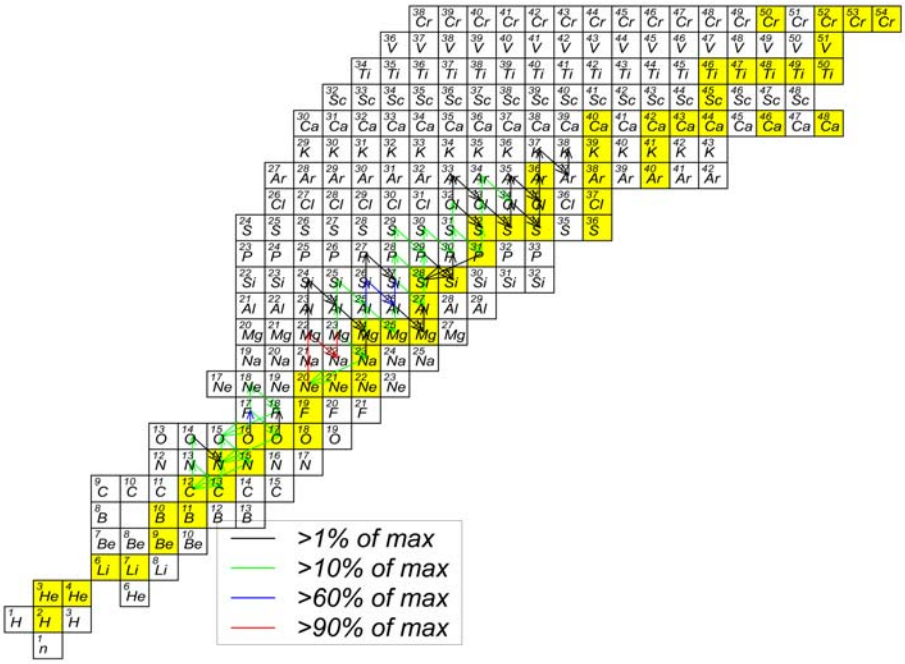

Figure 7.8. Flow with the $^{14}O(\alpha,2p)^{16}O$ reaction rate larger by a factor of 10^3 to the accepted $^{14}O(\alpha,p)^{17}F$ rate.

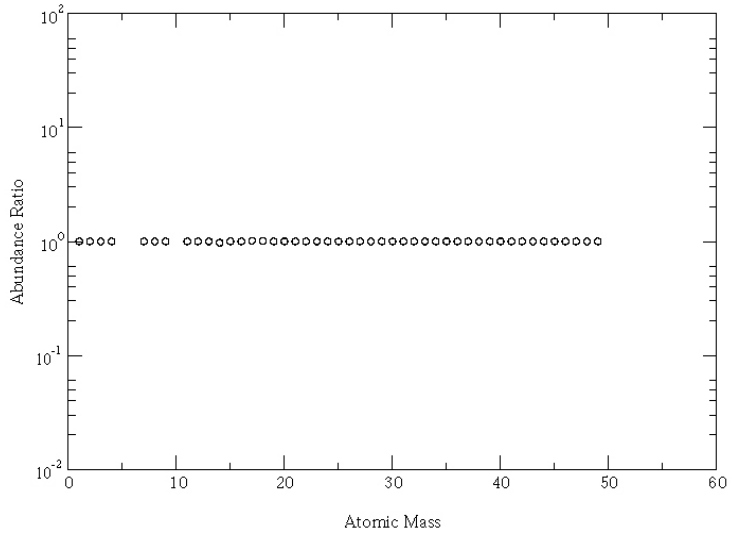

Figure 7.9. The final abundance ratio as a function of atomic mass when the $^{14}O(\alpha,2p)^{16}O$ rate is reduced by a factor of 10^{-9} than the accepted $^{14}O(\alpha,p)^{17}F$ rate. There is no significant difference in the final abundances.

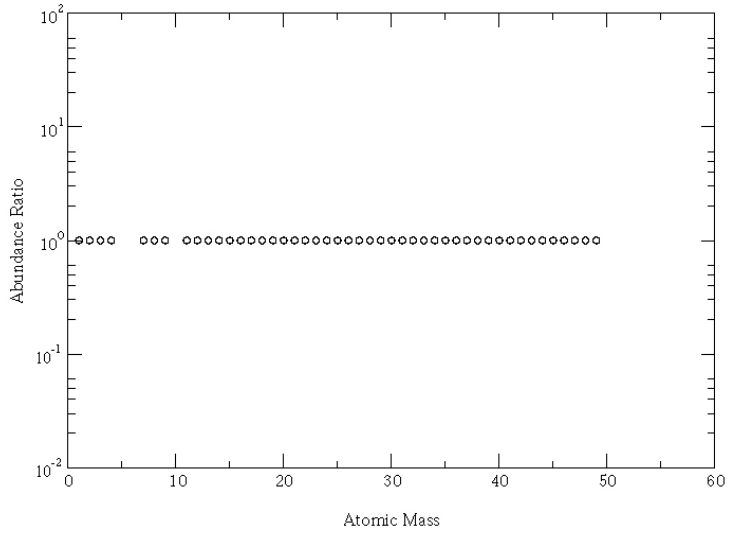

Figure 7.10. The final abundance ratio as a function of atomic mass when the $^{14}O(\alpha,2p)^{16}O$ rate is equal to the accepted $^{14}O(\alpha,p)^{17}F$ rate. There is no significant difference in the final abundances.

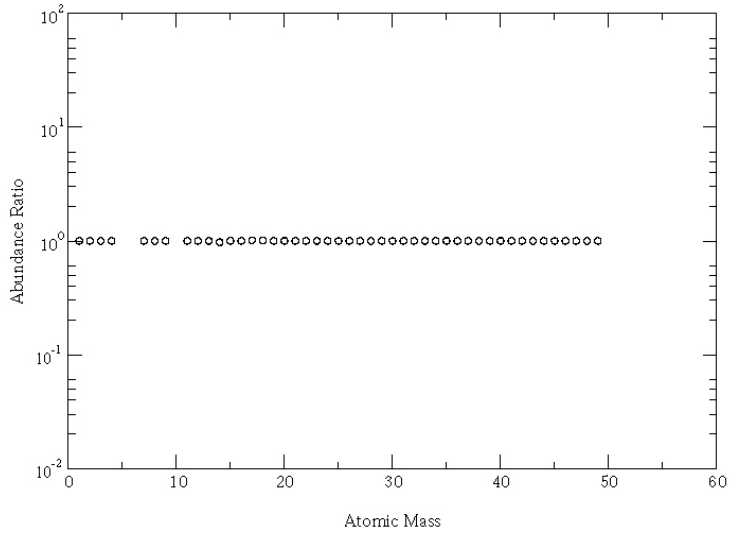

Figure 7.11. The final abundance ratio as a function of atomic mass when the $^{14}O(\alpha,2p)^{16}O$ rate is a factor of 1000 larger than the accepted $^{14}O(\alpha,p)^{17}F$ rate. There is no significant difference in the final abundances.

there is no significant difference among these cases when compared with the known $^{14}O(\alpha,p)^{17}F$ rate flow diagram. The final abundance ratio reveals changes of less than 1% in the final abundances (see figure 7.10). When the unknown $^{14}O(\alpha,2p)^{16}O$ rate is set to exceed the known $^{14}O(\alpha,p)^{17}F$ rate until saturation at a factor of 10^3, no significant difference is found (see figure 7.8 for reaction flow). The final abundance ratio also shows changes of less than 1% in the final abundances (see figure 7.11).

In our simulations, significant break out did not occur from the hot CNO cycle, and the $^{14}O(\alpha,p)^{17}F$ or $^{14}O(\alpha,2p)^{16}O$ reactions did not provide a path to heavy elements synthesis . The influence of $^{14}O(\alpha,p)^{17}F$ and $^{14}O(\alpha,2p)^{16}O$ are even smaller for the 1.25 $M_\odot$ ONeMg WD nova and 1.00 $M_\odot$ C-O WD nova since they have lower peak temperatures than the 1.35 $M_\odot$ ONeMg WD nova.

Chapter 8
X-Ray Burst Results (α,p) Case

As for the novae simulations, we vary the $^{14}O(\alpha, p)\,^{17}F$ rate over a range of 12 orders of magnitudes in our X-ray burst simulation. The scaling factor will again range from negligible (10^{-9}), increasing by factors of 10 until the accepted rate is reached (10^{0}) and exceeded (10^{3}). Again, when the $^{14}O(\alpha, p)\,^{17}F$ reaction rate is negligible (10^{-9}) we expect a decline in final abundance for the higher mass isotopes. As we steadily increased the rate by factors of 10, we analyzed the flux diagrams, the variation of fluxes in time, the energy production, the variation of abundances in time, the abundance ratios versus atomic mass, the abundance distribution after each simulation, and the over production relative to solar abundances for each simulation.

As established in chapter 3, nuclear burning for XRB is ignited at a density $\rho \geq 10^{6}$ g cm^{-3} through the pp chains, the triple-α process and the hot CNO-cycles. Figure 8.1 shows the reaction flow resulting from using the accepted $^{14}O(\alpha, p)^{17}F$ rate . Our reaction flow is comparable to the reaction flow found in [9,27], but there are some differences, most likely caused by the version of the reaction rate library we are using between the two reaction flows. As discussed in chapter 3, the temperatures of the burst are

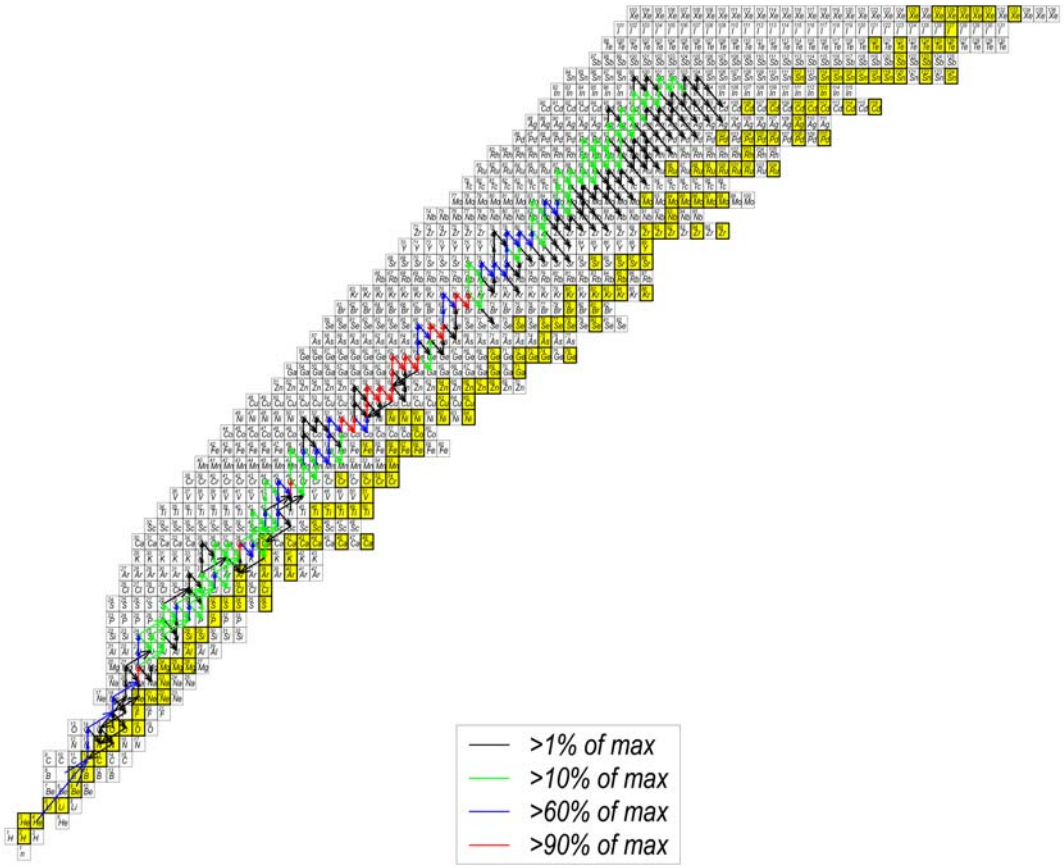

Figure 8.1. Flow diagram after a single zone X-ray burst.

sufficiently high to trigger the rp and αp-processes. Previous simulations have shown that the rp- process can proceed well into the A=80-100 mass region within the short time scale of the XRB. Figure 8.2 shows the abundance distribution following the thermonuclear runaway after our single zone XRB, they are comparable to the abundance distributions found in [9], with small differences most likely attributable to the different reaction rate library used. While there is still an appreciable amount of hydrogen, the bulk (90%) of the material has been converted to nuclei with masses $A \geq 70$ by the rp-process. Figure 8.2.1 shows the abundance distribution after freeze-out when all the β-unstable isotopes along the process path have decayed backed to the stability valley. The light p nuclei are enriched by more than seven orders of magnitude when compared to their solar abundance [27].

The energy production resulting from this rapid build up toward the A =100 mass region is shown in figure 8.3. The structure of this energy production plot is comparable to that for the energy production found in [27], again with small differences caused by the nuclear reaction rate library. The energy production shows periods of continuous reaction flow where rapid proton and alpha captures, and β decays, lead to an increase in energy production [27]. Also apparent are waiting point isotopes, where

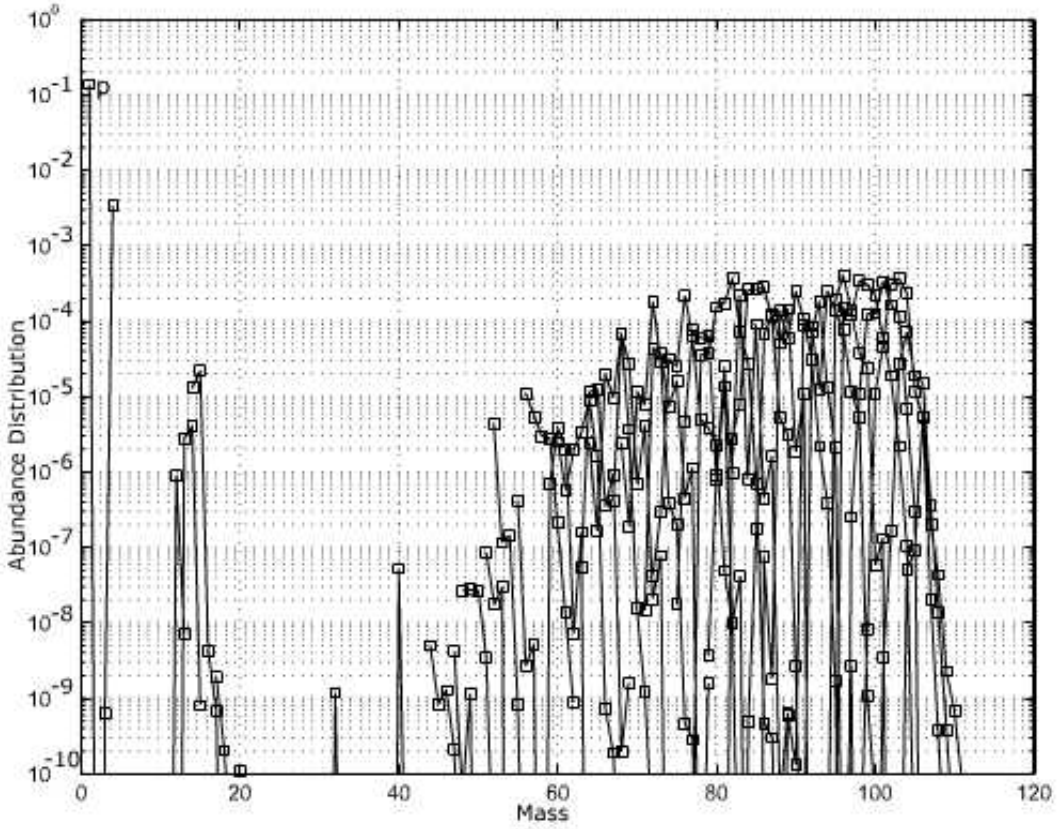

Figure 8.2. The abundance distribution after the TNR of a single XRB.

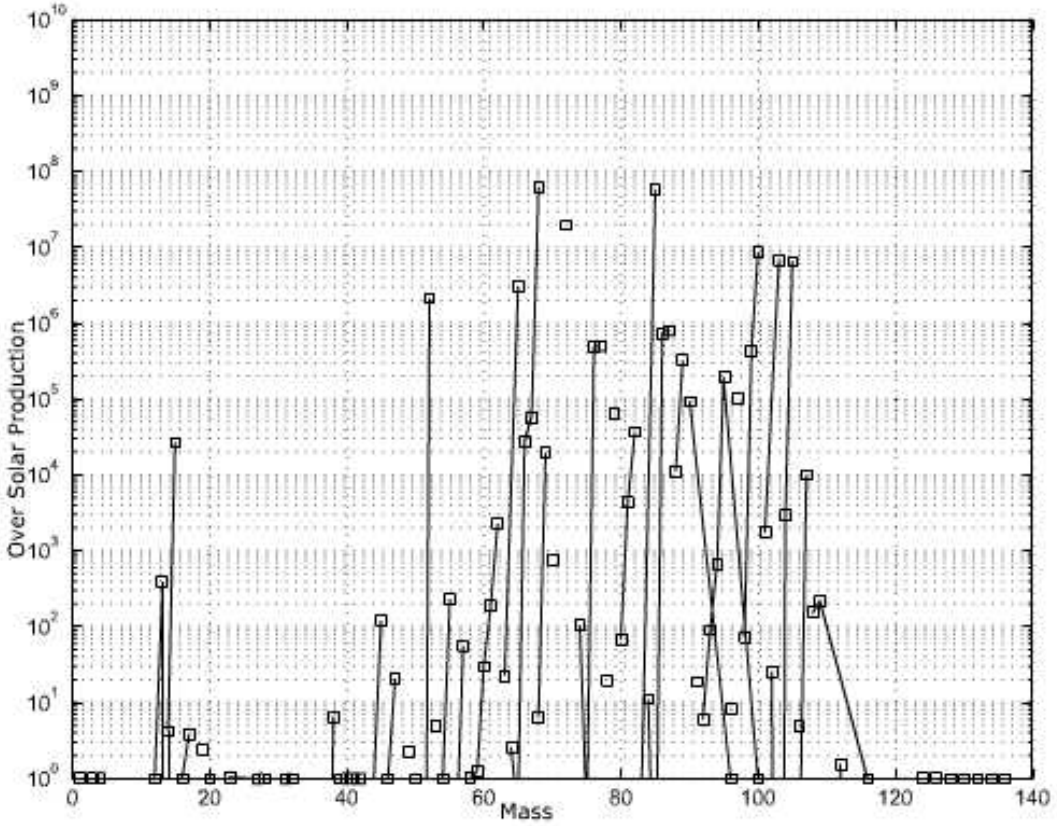

Figure 8.2.1 The ratio of the produced abundances and initial solar abundances after the TNR of an XBR.

further proton captures are suppressed [27,62]. Similarly to the finding in [9,27], our energy production is characterized by four distinct phases.

Phase (1) is the ignition of the burst, which is marked by the processing of the hot CNO cycles that serve as catalysts for the burst. Phase (1) is initiated by proton captures on ^{12}C, ^{14}N, and ^{16}O, which were not completely destroyed by spallation in the atmosphere of the accreting neutron star [30]. The first peak in energy production is caused by the conversion of the initial abundance of ^{12}C to the hot CNO waiting point nucleus ^{14}O via the path $^{12}C(p,\gamma)\,^{13}N(p,\gamma)\,^{14}O$. The second peak is a result of the conversion of the initial abundance of ^{16}O to the hot CNO waiting point at ^{18}Ne and ultimately to ^{15}O. The build up toward ^{18}Ne occurs by two successive proton captures: $^{16}O(p,\gamma)\,^{17}F(p,\gamma)\,^{18}Ne$. During the early phase of the burst, when temperatures are not too high, the ^{18}Ne will β^+ decay to ^{18}F and close the hot CNO cycle by returning to ^{15}O by the reaction path $^{18}F(\gamma,\alpha)^{15}O$. The temperature will rise sufficiently to trigger phase (2) of the energy production during the slow β decay of the hot-CNO waiting points ^{14}O and ^{15}O. The nucleosynthesis for this phase is shown in figure 8.4.

Phase (2) is instigated by triple-α burning; it is characterized by (α,p) reactions and considerably more helium is burned than hydrogen during this

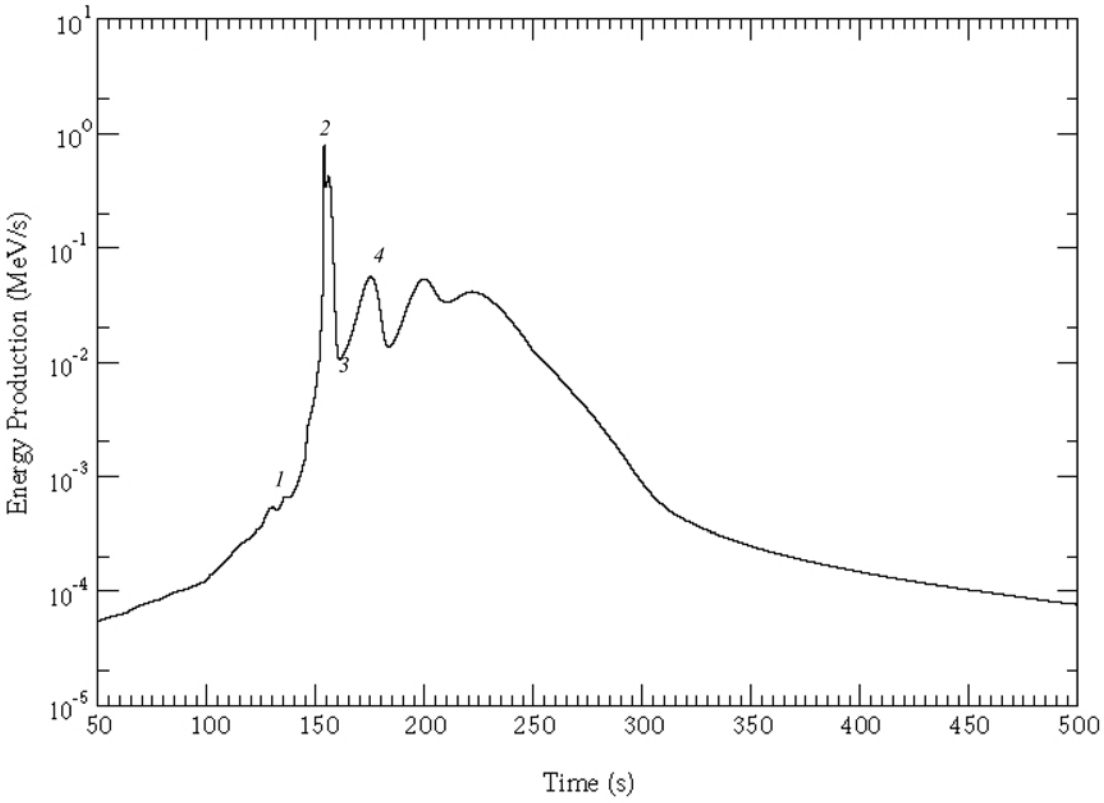

Figure 8.3. The energy production during an X-ray burst. It is characterized by four distinct phases.

phase. The fine structure of the energy production reveals four distinct features of building toward the next waiting points. During the first peak the hot CNO waiting point isotopes ^{14}O, ^{15}O, and ^{18}Ne are depleted and rapidly converted to the next waiting point nucleus, ^{24}Si, by the αp-process. Because of the β decay of the ^{24}Si ($t_{1/2}$=102ms) isotope, energy production drops until higher temperatures trigger further α and proton capture. The ^{24}Si is then rapidly converted to the next two waiting point isotopes ^{29}S and ^{34}Ar . Further α captures occur because of the swift rise in temperature and nuclei the above waiting points isotopes are eventually converted to ^{56}Ni. The temperature reaches its peak and further processing is stopped by a $^{56}Ni(p,\gamma)$-(γ,p) equilibrium [62]. As a result, the energy production will drop rapidly while most of the initial inventory of isotopes, as well as a large fraction of the initial helium, remains stored in the waiting point nucleus ^{56}Ni. The decline in energy production slows the temperature growth rate just before the peak is reached [27]. The nucleosynthesis of this phase is shown in figure 8.4.1

The energy production is then dependent on the reaction rates $^{56}Ni(p,\gamma)\,^{57}Cu$ and $^{57}Cu(p,\gamma)\,^{58}Zn$. At temperatures above 2GK, both rates are in equilibrium with the inverse photodisintegration [27]. The reaction flow

stops and the energy production drops; consequently there is a slow decrease in temperature. This corresponds to phase (3), the dormant phase of the burst (see figure 8.4.2); any further nucleosynthesis awaits the slow beta decay of ^{56}Ni.

Phase (4) is initiated as soon as the temperature drops below 2GK. The decrease in temperature will significantly decrease the effective lifetime of ^{56}Ni, which in turn removes (p,γ)-(γ,p) equilibrium and allows a two proton capture on ^{56}Ni [62] . The energy production and the reaction flow path of this phase are characterized by rp-process nucleosynthesis beyond ^{56}Ni. The first peak in the energy production is the result of the depletion of ^{56}Ni, the second peak is caused by further processing toward ^{64}Ge, and the last peak is a result of processing toward the next waiting point, ^{68}Se. During the final phase, ^{68}Se is processed to the mass 100 region. The nucleosynthesis for this phase is shown in figure 8.4.3.

Figures 8.5-8.16 are plots of the ratio of final abundances produced by the network with the varied rates for ^{14}O(α,p)^{17}F to the final abundances produced by the network with the currently accepted rate for ^{14}O(α,p)^{17}F. Each final abundance ratio is plotted versus the atomic mass. From these plots we determine the importance of the ^{14}O(α,p)^{17}F rate on the final

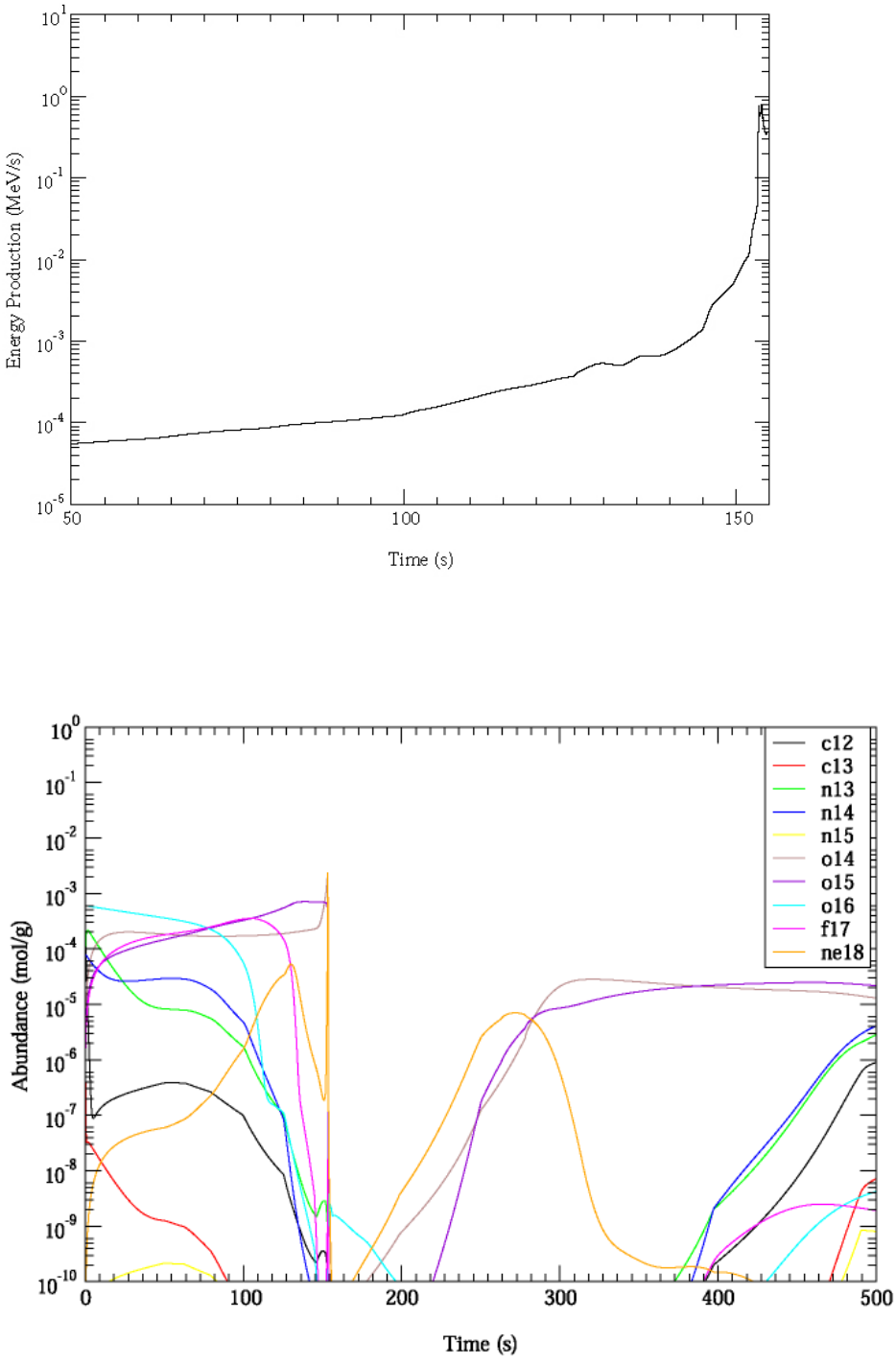

Figure 8.4. The first phase of the energy production which corresponds to the conversion of the initial abundances into the hot CNO waiting point isotopes of ^{14}O, ^{15}O, and ^{18}Ne.

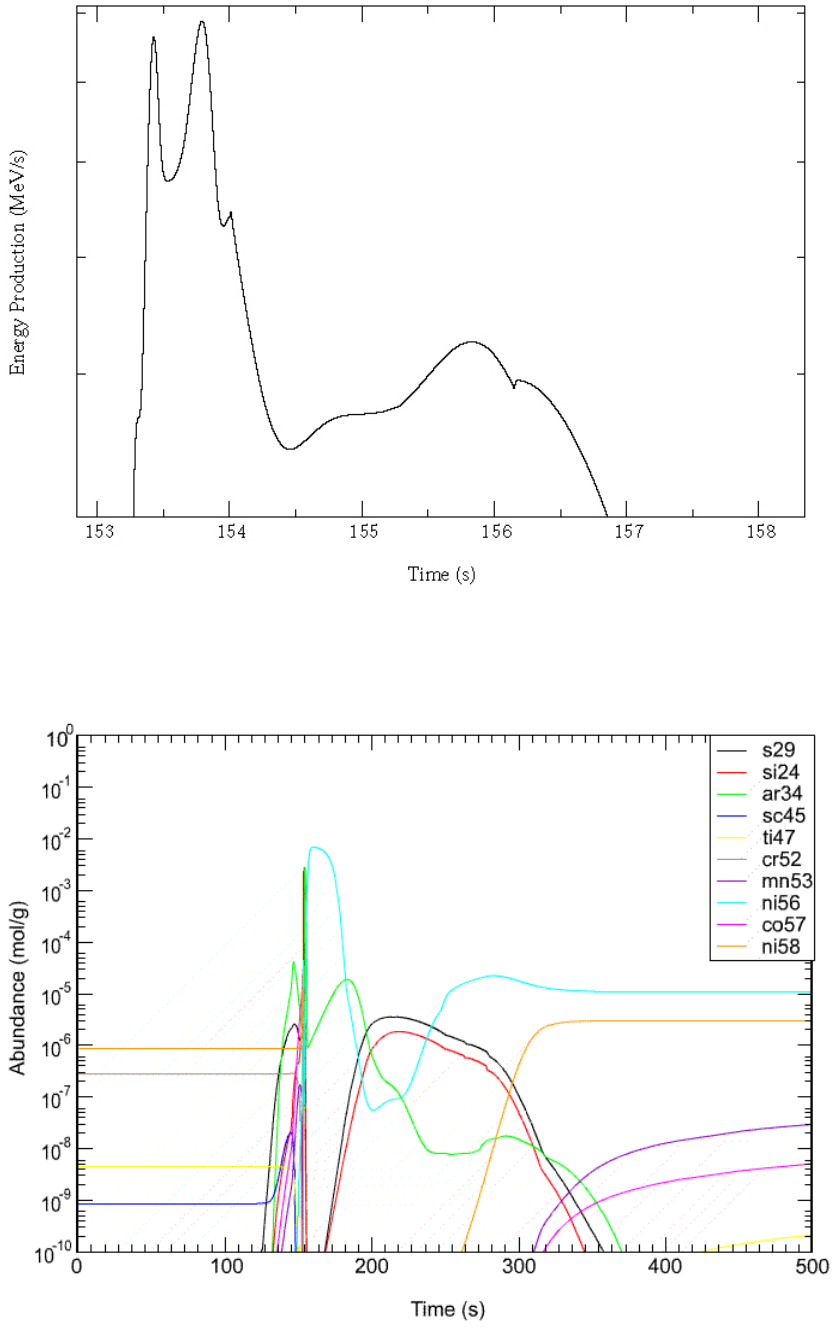

Figure 8.4.1 Phase 2 of the energy production, which corresponds to the peak of the XRB. During this phase the CNO waiting points are depleted and converted to ^{24}Si, ^{29}S,^{34}Ar and ^{56}Ni.

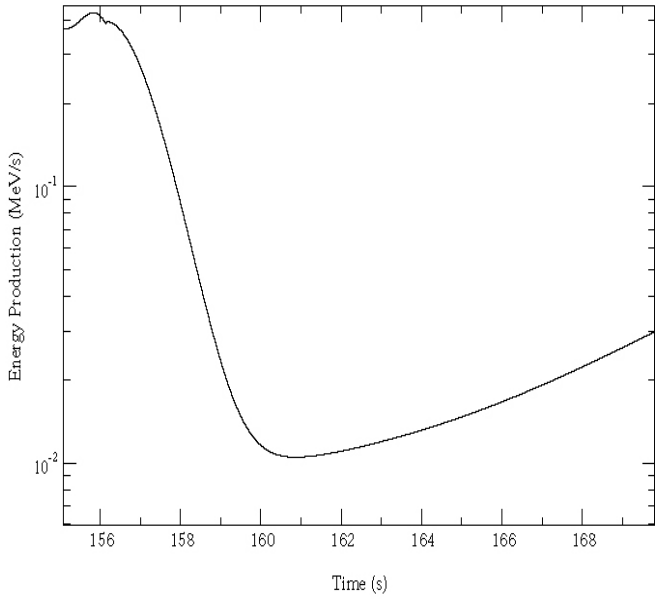

Figure 8.4.2 Phase 3 of the energy production, which is the dormant phase of the energy production of the XBR; in this phase nucleosynthesis awaits the slow beta decay of ^{56}Ni.

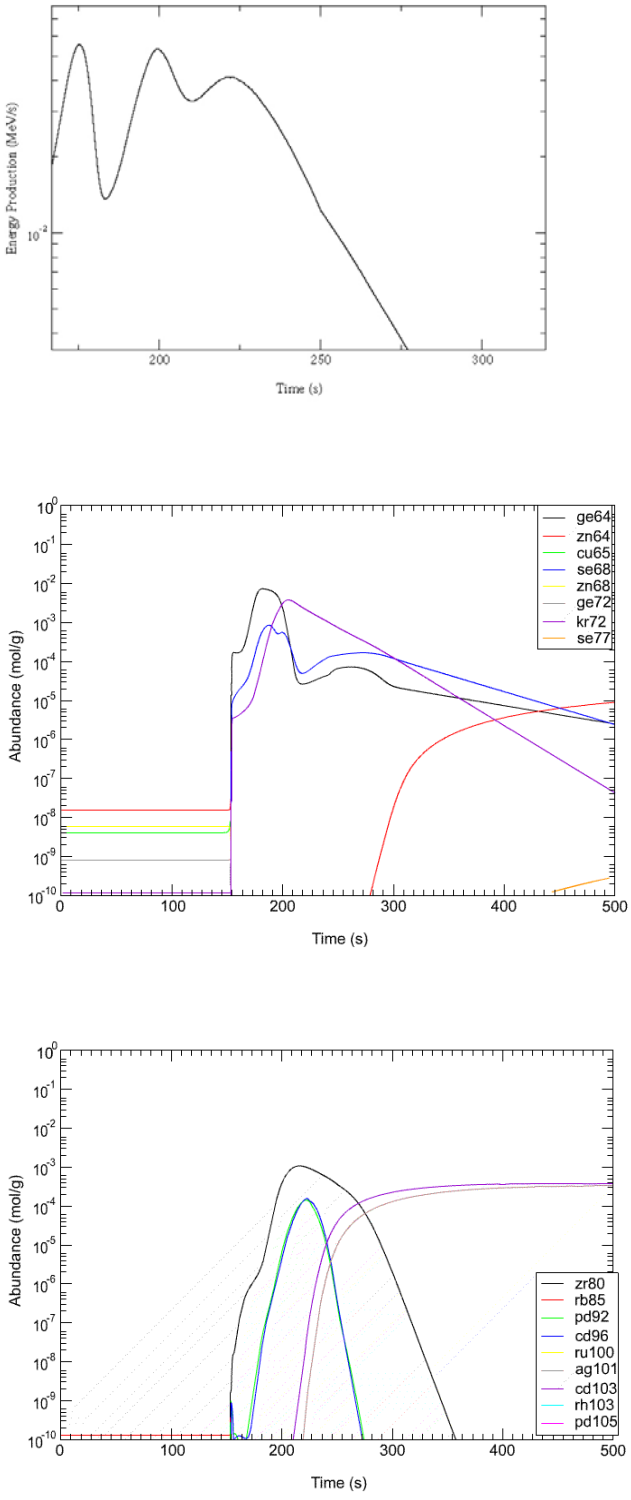

Figure 8.4.3 Phase 4 of the energy production, which corresponds to the destruction of the waiting point isotopes.

abundances. We have found distinct ranges of variations of the $^{14}O(\alpha,p)^{17}F$ rate on the final abundances, with multiplications factors of: 10 to 1000; 10^{-3} to 1; 10^{-4} to 10^{-6}; and 10^{-7} and 10^{-9}.

8.1 $^{14}O(\alpha, p)^{17}F$ Dominant (Factors 10^{-3} and Up)

At factors of 10^{-3} and larger the $^{14}O(\alpha,p)^{17}F$ reaction dominates until saturation. The flow diagram is similar to that for the accepted rate (see figure 8.1). Figures 8.8-8.11 are the abundance ratio when the $^{14}O(\alpha,p)^{17}F$ rate is reduced by factors 10^{-1} to 10^{-3}, respectively. At 10^{-1} of the accepted accepted $^{14}O(\alpha,p)^{17}F$ rate shows that the mass region A=51-72 is depleted up to 45%, with ^{56}Ni being depleted by 30%; while the CNO isotopes and mass region A=20-50 are enriched by 20%-51%, with ^{14}O being enriched by 51%. The energy production is consistent with the energy production obtained with the accepted rate. At factors greater than 1 (figures 8.5-8.8), the nucleosynthesis reveals that the mass region A=45-72 are enriched while the CNO isotopes and mass region A=20-44 are depleted. At factors of 10 and 100 ^{14}O is depleted by 25% and 33% respectively, while ^{56}Ni is enriched by 20% and 25% respectively. The energy production is again consistent with that of the known rate. It is important to mention that the $^{14}O(\alpha, p)^{17}F$

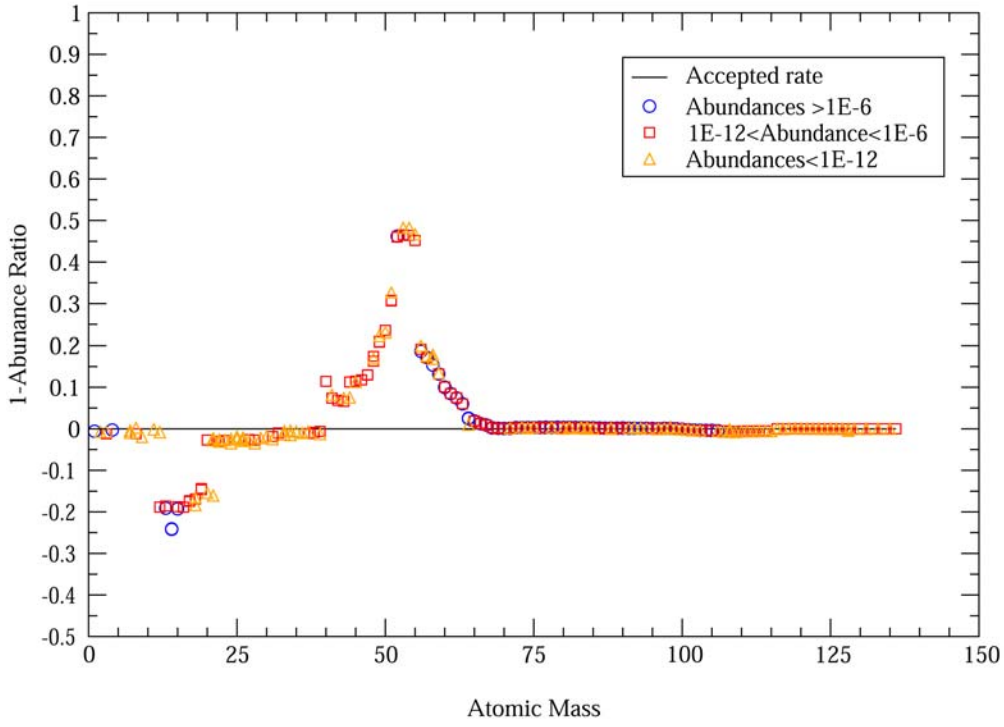

Figure 8.5. The final abundance ratio as a function of atomic mass when the $^{14}O(\alpha,p)^{17}F$ rate is a factor of 10 larger times the accepted $^{14}O(\alpha,p)^{17}F$ rate. The enhancement of the $^{14}O(\alpha,p)^{17}F$ rate enhances the flow of matter out of the CNO isotopes toward the A=20-72 region.

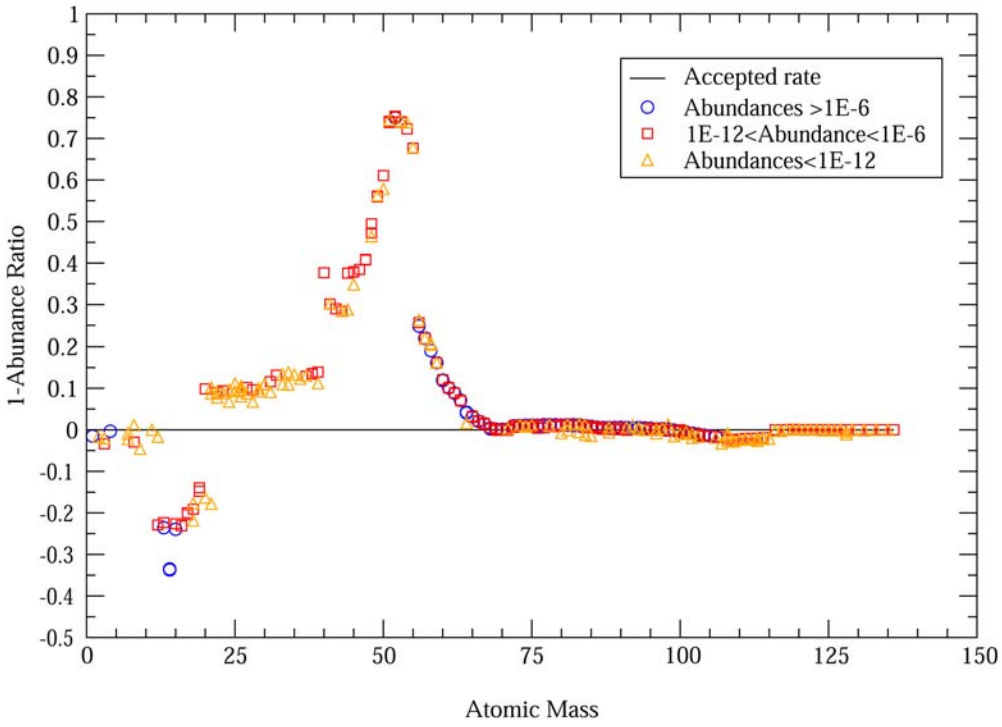

Figure 8.6. The final abundance ratio as a function of atomic mass when the $^{14}O(\alpha,p)^{17}F$ rate is a factor of 100 larger times the accepted $^{14}O(\alpha,p)^{17}F$ rate. The enhancement of the $^{14}O(\alpha,p)^{17}F$ rate by a factor of 100 further enhances the flow of matter out of the CNO isotopes toward the A=20-72 region.

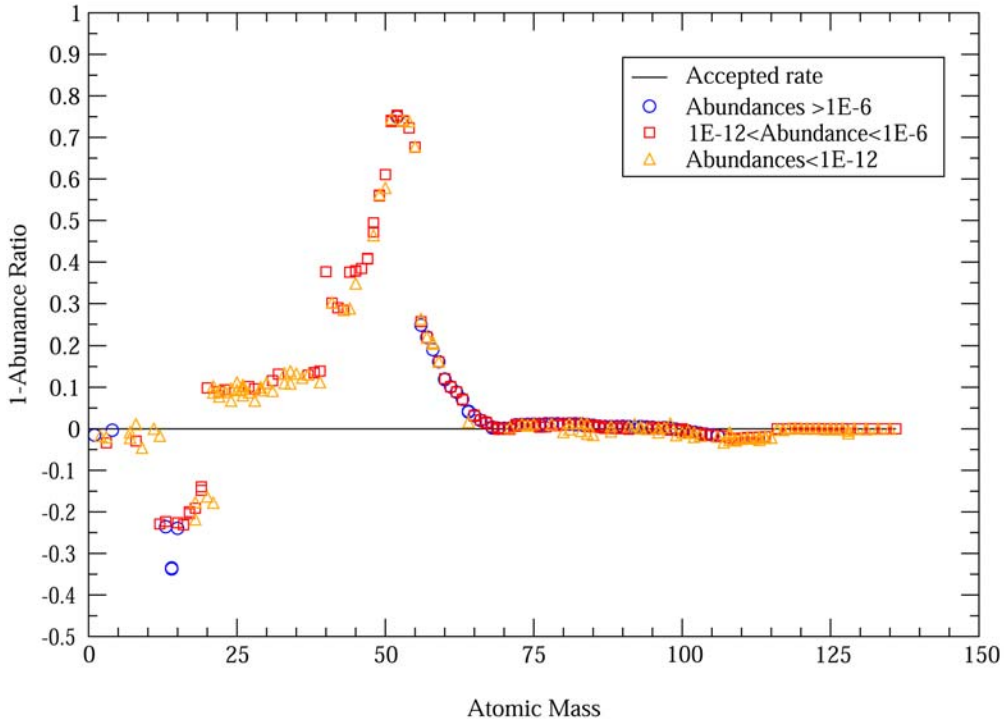

Figure 8.7. The final abundance ratio as a function of atomic mass when the $^{14}O(\alpha,p)^{17}F$ rate is a factor of 1000 larger times the accepted $^{14}O(\alpha,p)^{17}F$ rate. The $^{14}O(\alpha,p)^{17}F$ rate is saturated and does not enhances much faster than a factor of 100.

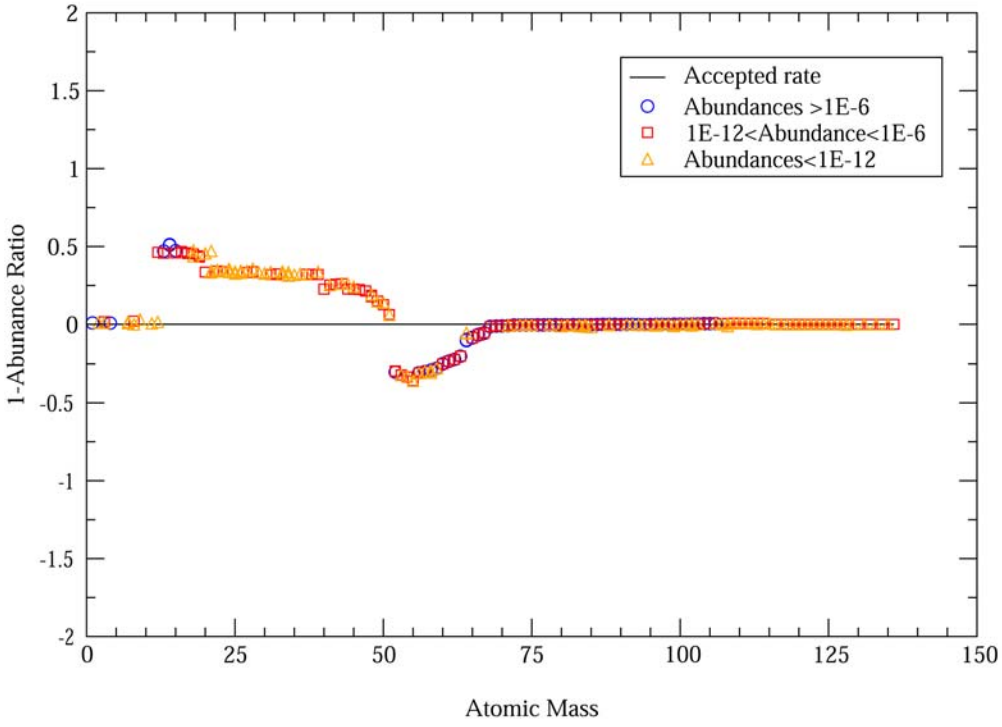

Figure 8.8. The final abundance ratio as a function of atomic mass when the $^{14}O(\alpha,p)^{17}F$ rate is reduced by a factor of 10^{-1} times the accepted $^{14}O(\alpha,p)^{17}F$ rate. The slight reduction of the $^{14}O(\alpha,p)^{17}F$ rate slows down the flow matter out of the CNO isotopes toward the A=20-72 region.

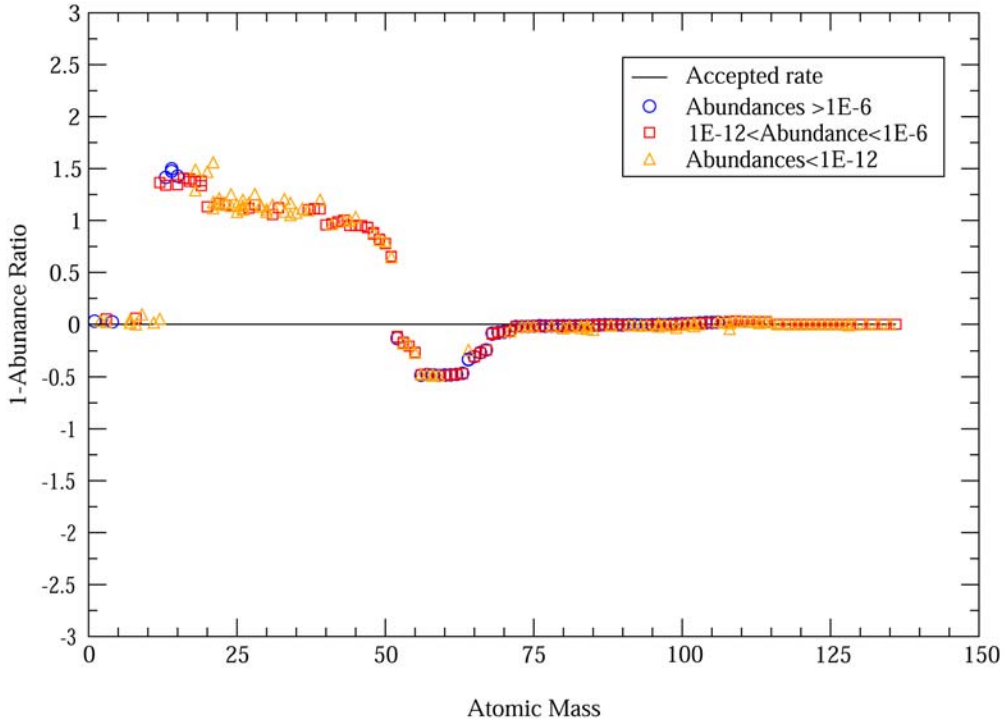

Figure 8.9. The final abundance ratio as a function of atomic mass when the $^{14}O(\alpha,p)^{17}F$ rate is reduced by a factor of 10^{-2} times the accepted $^{14}O(\alpha,p)^{17}F$ rate. The further reduction of the $^{14}O(\alpha,p)^{17}F$ rate further slows the flow of matter out of the CNO isotopes toward the A=20-72 region.

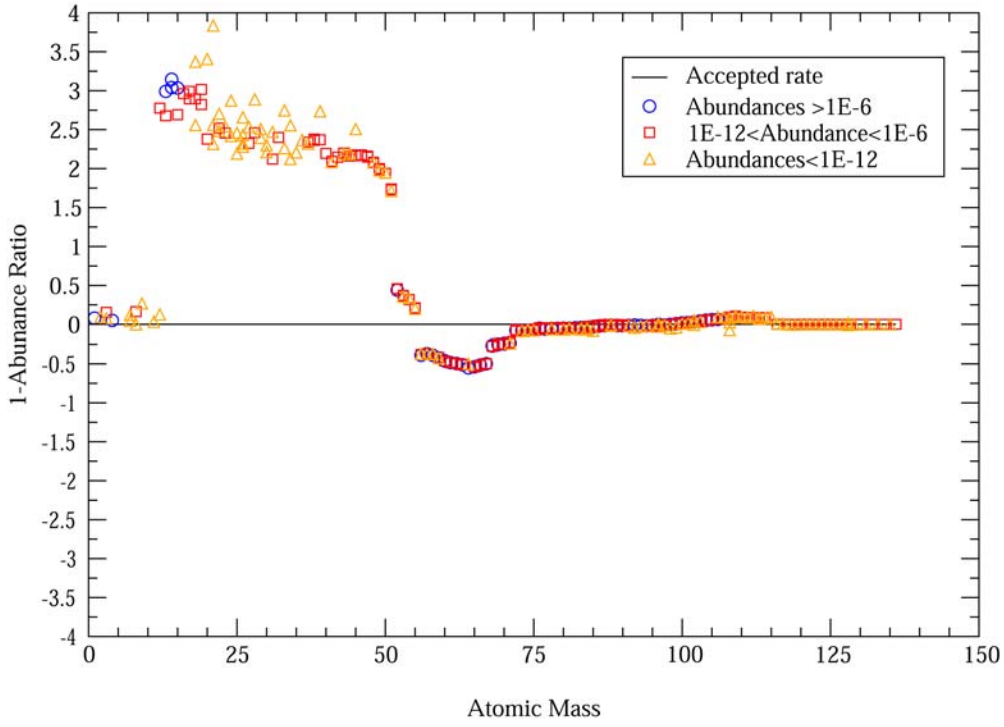

Figure 8.10. The final abundance ratio as a function of atomic mass when the $^{14}O(\alpha,p)^{17}F$ rate is reduced by a factor of 10^{-3} times the accepted $^{14}O(\alpha,p)^{17}F$ rate. The further reduction of the $^{14}O(\alpha,p)^{17}F$ rate further slows d the flow of matter out of the CNO isotopes toward the A=20-72 region.

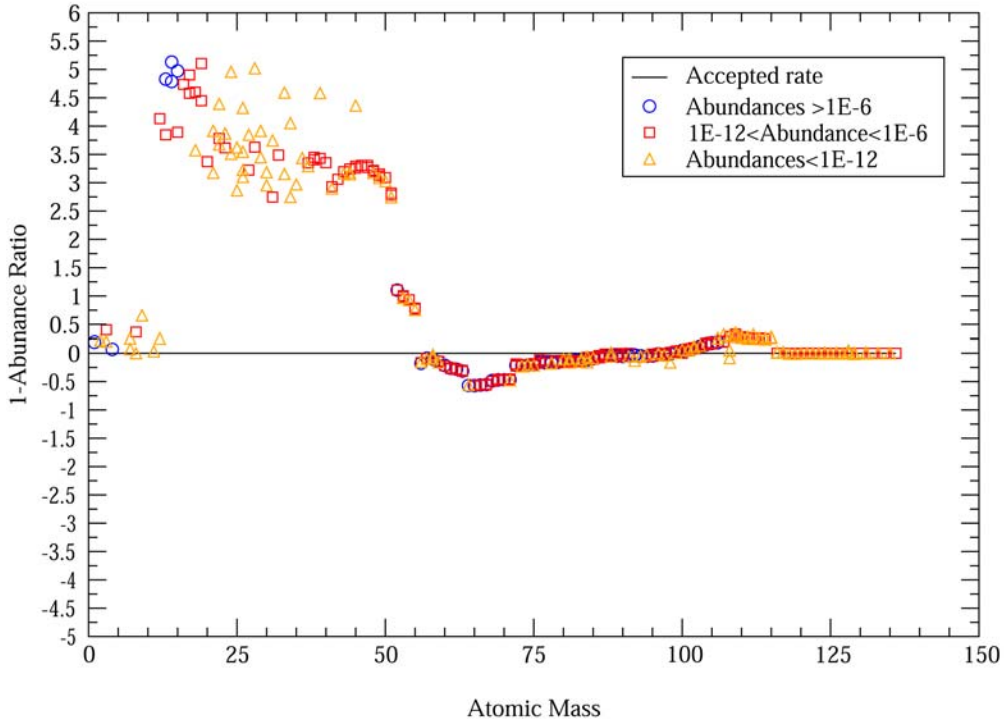

Figure 8.11. The final abundance ratio as a function of atomic mass when the $^{14}O(\alpha,p)^{17}F$ rate is reduced by a factor10^{-4} times the accepted $^{14}O(\alpha,p)^{17}F$ rate. The $^{14}O(\alpha,p)^{17}F$ rate is now mildly dominant and the $^{14}O(\alpha,\gamma)^{18}Ne$ contributes weakly to the funneling of matter toward the A=20-72 mass region.

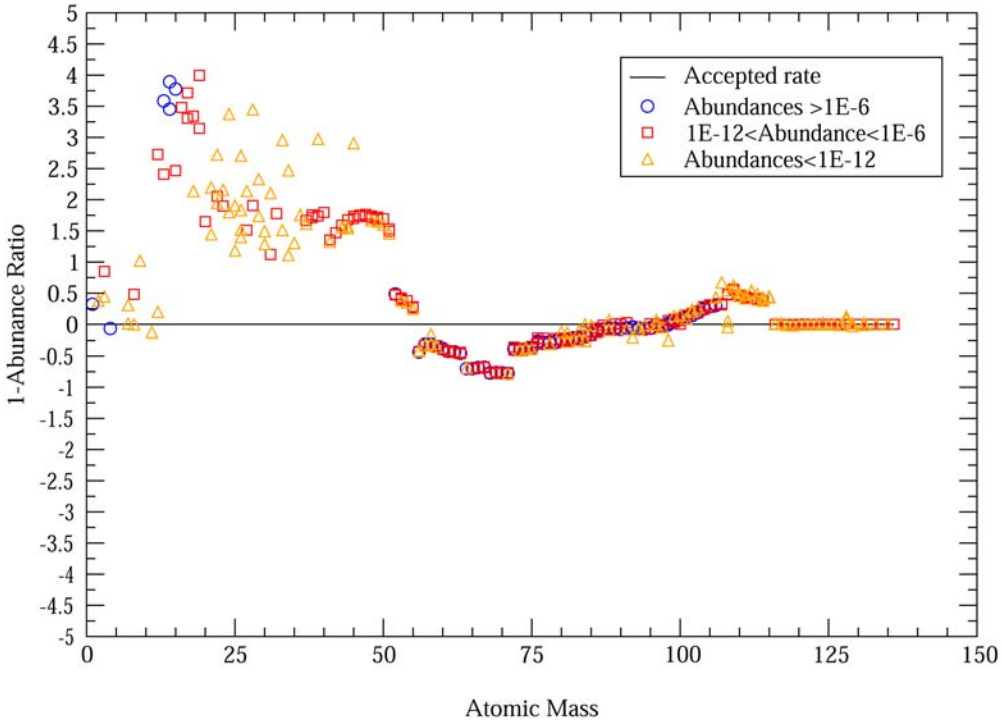

Figure 8.12. The final abundance ratio as a function of atomic mass when the $^{14}O(\alpha,p)^{17}F$ rate is reduced by a factor of 10^{-5} times the accepted $^{14}O(\alpha,p)^{17}F$ rate. The $^{14}O(\alpha,p)^{17}F$ rate is now mildly dominant and the $^{14}O(\alpha,\gamma)^{18}Ne$ is contributing in the funneling of matter toward the A=20-72 mass region.

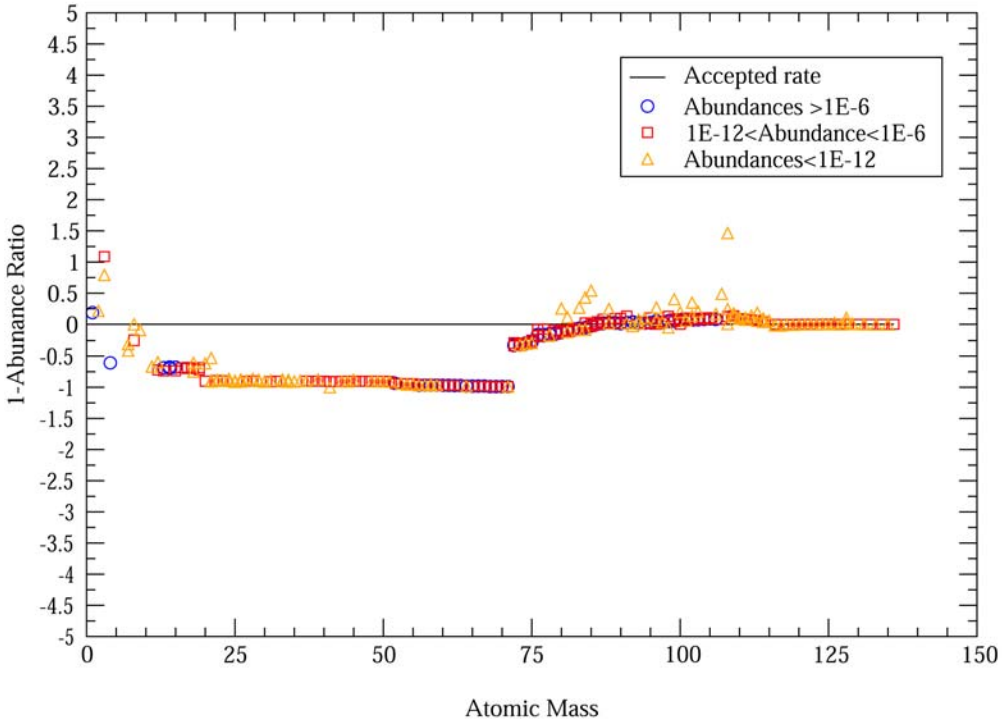

Figure 8.13. The final abundance ratio as a function of atomic mass when the $^{14}O(\alpha,p)^{17}F$ rate is reduced by a factor of 10^{-6} times the accepted $^{14}O(\alpha,p)^{17}F$ rate. The $^{14}O(\alpha,p)^{17}F$ and the $^{14}O(\alpha,\gamma)^{18}Ne$ reactions contribute at equal strength in the funneling of matter toward the A=20-72 mass region.

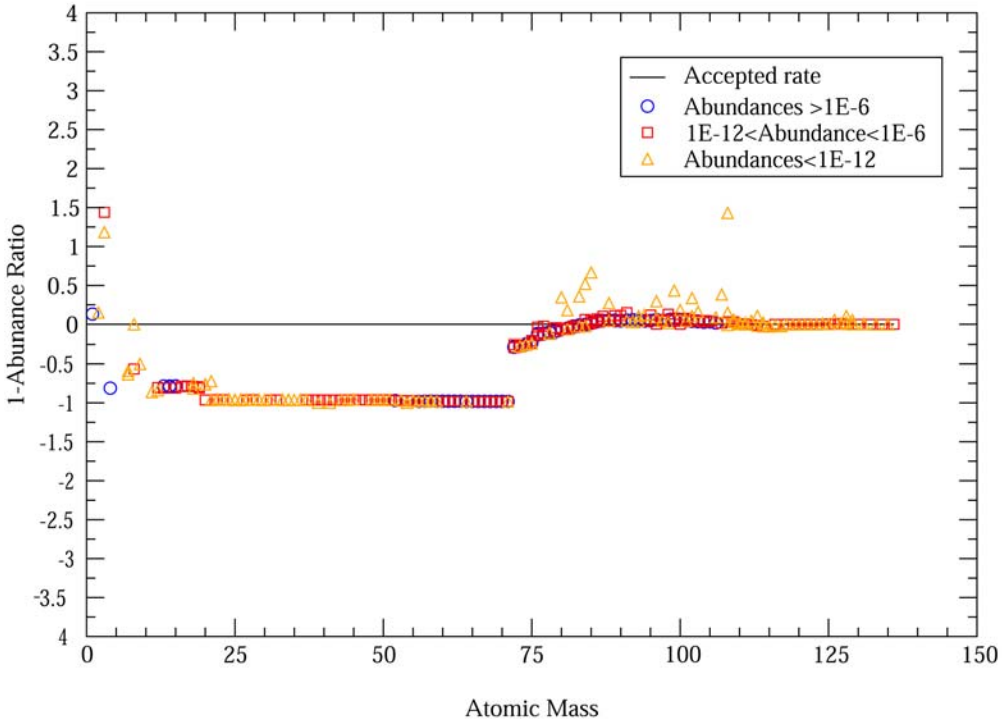

Figure 8.14. The final abundance ratio as a function of atomic mass when the $^{14}O(\alpha,p)^{17}F$ rate is reduced by a factor of 10^{-7} times the accepted $^{14}O(\alpha,p)^{17}F$ rate**.** The $^{14}O(\alpha,p)^{17}F$ rate is no longer dominant and the $^{14}O(\alpha,\gamma)^{18}Ne$ is now responsible in the funneling of matter toward the A=20-72 mass region.

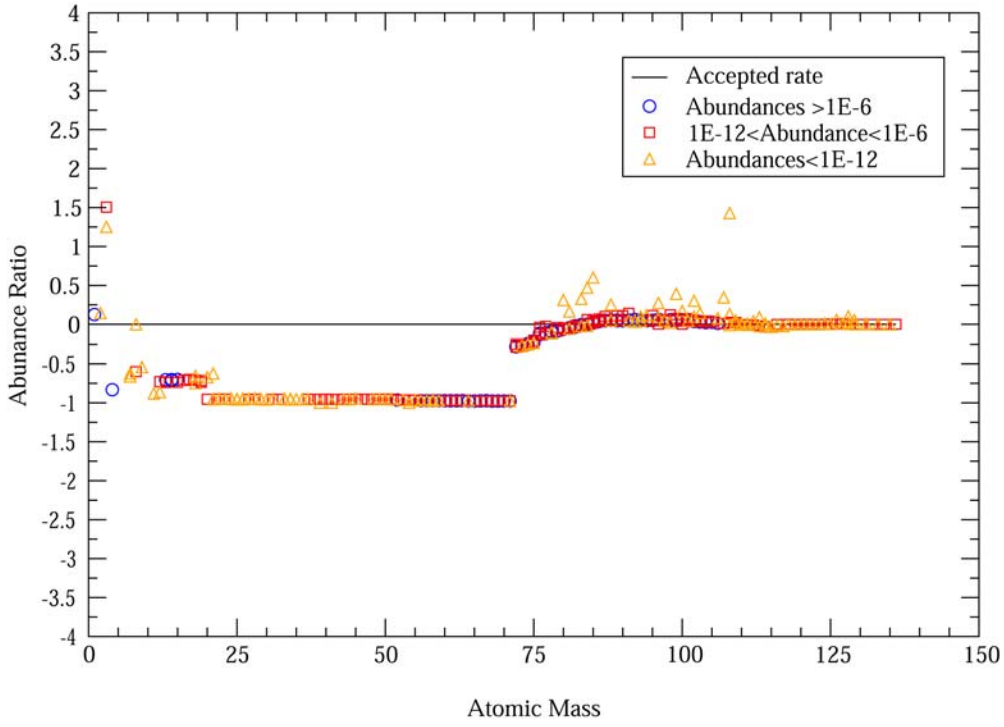

Figure 8.15. The final abundance ratio as a function of atomic mass when the $^{14}O(\alpha,p)^{17}F$ rate is reduced by a factor of 10^{-8} times the accepted $^{14}O(\alpha,p)^{17}F$ rate.

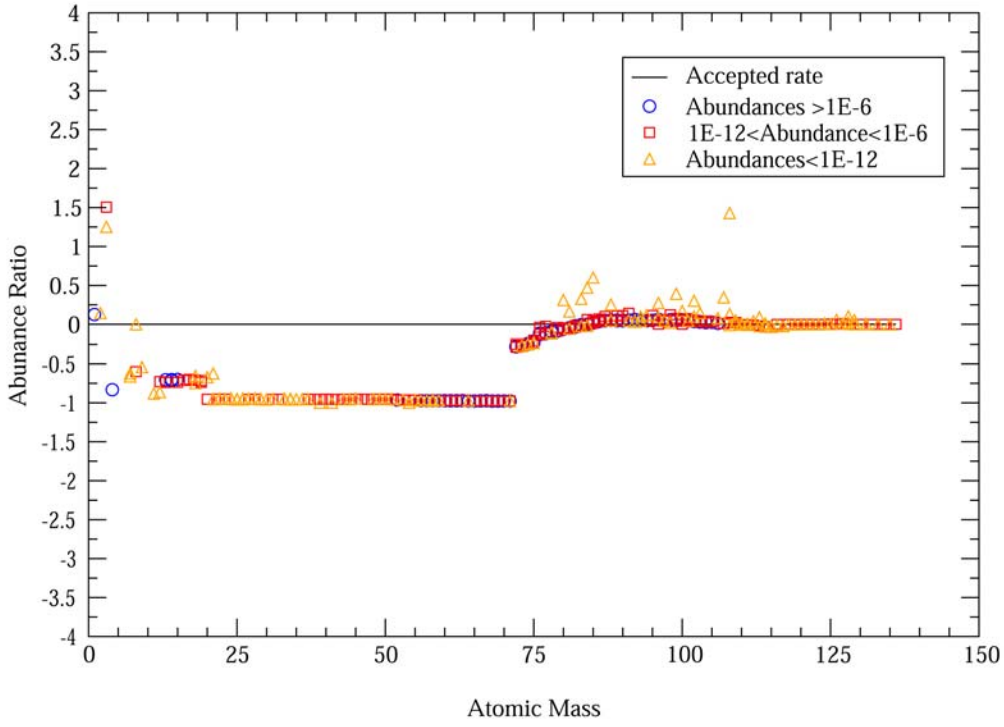

Figure 8.16. The final abundance ratio as a function of atomic mass when the $^{14}O(\alpha,p)^{17}F$ rate is reduced by a factor of 10^{-9} times the accepted $^{14}O(\alpha,p)^{17}F$ rate.

rate flux saturates when multiplied by a factor of 100 (see figure 8.17) or greater. Thus is not necessary to enhance the rate by factors greater than 100. Our finding shows for scaling factors greater than 100 the effect on final abundances are the same for the rate enhanced by a factor of 100.

8.2 $^{14}O(\alpha, p)^{17}F$ Rather Dominant (Factors 10^{-4} to10^{-6})

When the $^{14}O(\alpha, p)^{17}F$ rate is multiplied by a factor of 10^{-4} (see figure 8.18) the flow diagram reveals a weak $^{14}O(\alpha,\gamma)^{18}Ne$ path out of ^{14}O. The weak $^{14}O(\alpha,\gamma)^{18}Ne$ flux alters the reaction flow path above ^{22}Mg. Figure 8.18 shows that the destruction of ^{14}O occurs mostly by the $^{14}O(\alpha, p)^{17}F$ reaction. The build up to ^{22}Mg is consistent with that of the accepted rate, the destruction of ^{22}Mg occurs equally via two different paths. The first path $^{22}Mg(p,\gamma)^{23}Al$ builds toward the waiting point isotopes ^{24}Si and ^{29}S; the second path $^{22}Mg(\alpha, p)^{25}Al$ builds toward the waiting point isotope ^{34}Ar, where the two paths converge.

When the $^{14}O(\alpha, p)^{17}F$ rate is multiplied by a factor of 10^{-5} (see figure 8.19) the $^{14}O(\alpha, p)^{17}F$ still dominates, while the flux of the $^{14}O(\alpha,\gamma)^{18}Ne$ reaction gets relatively stronger. The path to ^{22}Mg remains unperturbed, whilst the depletion of ^{22}Mg takes place primarily via the (α, p)-(p,γ)

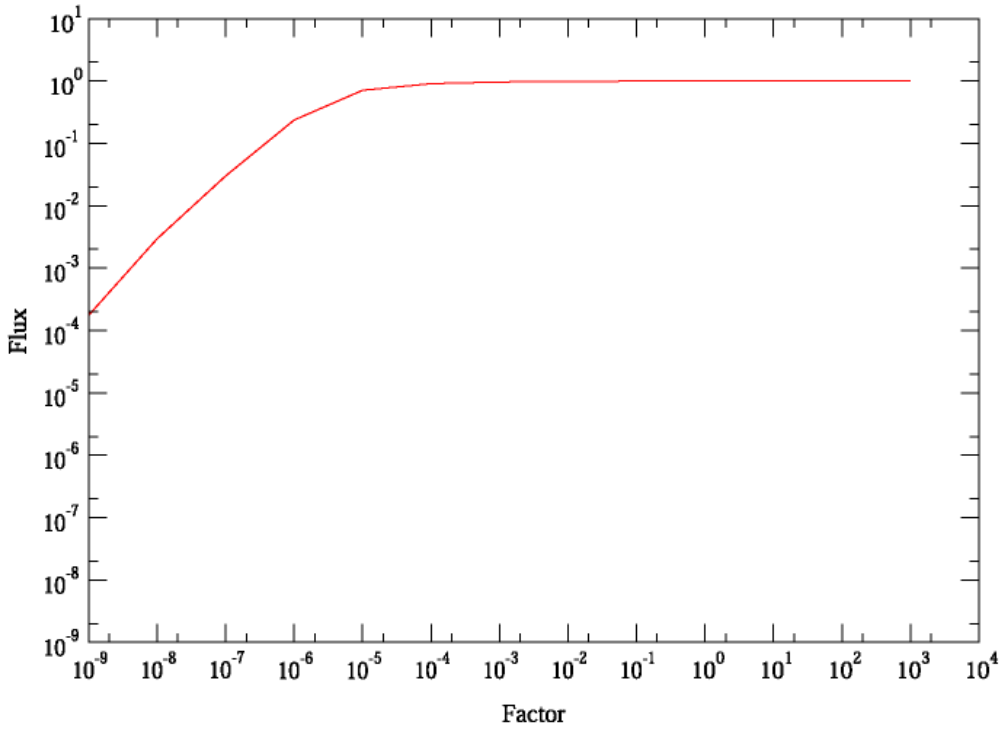

Figure 8.17. The $^{14}O(\alpha, p)\,^{17}F$ flux contributes heavily from a factor of 10^{-6} or greater and saturates when the $^{14}O(\alpha, p)\,^{17}F$ rate is multiplied by factors of 10 or greater.

reactions that build toward the waiting point isotope ^{34}Ar. When the ^{14}O(α, p) ^{17}F rate is multiplied by a factor of 10^{-6}, the ^{14}O(α, p) ^{17}F reaction and the ^{14}O(α,γ) ^{18}Ne reaction are roughly of equal strength (see figure 8.20). The depletion of ^{22}Mg takes place mostly via the (α, p)-(p,γ) reactions that build toward ^{34}Ar. Reduction by a factor of 10^{-6} is a unique case because it is the case where the ^{14}O(α, p) ^{17}F ceased being the dominant reaction out of ^{14}O. The effect can be seen immediately not only on the final abundances (Fig 8.14) but also on the energy production (Fig 8.26). On the final abundances the behavior reverses from reducing the rate by 10^{-5}, with CNO isotopes being enhanced due to a reduced ^{14}O(α, p) ^{17}F rate. Depletion from the CNO isotopes to A=20-72 mass region is observed. This behavior is further enhanced when the ^{14}O(α, p) ^{17}F rate is further reduced by a factor of 10^{-7} or smaller.

The comparison of the energy production with the accepted rate is shown in figure 8.26. The four different phases can be observed. The fine structure of the energy production plots reveals a change in phase (2) as the ^{14}O(α,p) ^{17}F rate is varied. This variation is a delay which is enhanced by the further reduction of the ^{14}O(α,p) ^{17}F, and ultimately affects the late time burning of the energy production plot. This delay is explained in 8.3.

Note that while the $^{14}O(\alpha,p)^{17}F$ rate is varied both CNO isotopes and the A=20-72 mass region are affected. The portrait that has been painted is that when the varied rate is enhanced depletion in the CNO isotopes and mass region A=20-50 are observed, with changes in the A=51-72 mass region. When the varied rate is reduced an enrichment in CNO isotopes and A=20-50 are observed.

Thus when the rate is reduced by a factor of 10^{-4}, the CNO isotopes are enhanced and the A=20-50 isotopes are enhanced by a factor no greater 7, with ^{14}O being enriched by 25% ; and the A=51-72 region mass is depleted by a factor no greater than 7, with ^{56}Ni depleted by 20% (Fig 8.12). The depletion of ^{56}Ni is a possible observable, since ^{56}Ni is a good γ-ray source. At a factor 10^{-5} of the known rate, the CNO isotopes are enriched by a factor no greater than 5. The A=20-50 mass region in enriched by a factor of no greater than 2, while the A=51-72 mass region is depleted by a factor of 5 (Fig 8.13). When the rate is reduced by a factor of 10^{-6} a depletion by a factor of 3 is observed in the CNO isotopes, and in the A=20-72 mass region production of abundances is suppressed by a factor between 20-30 (Fig 8.14). The A>72 region remained unperturbed.

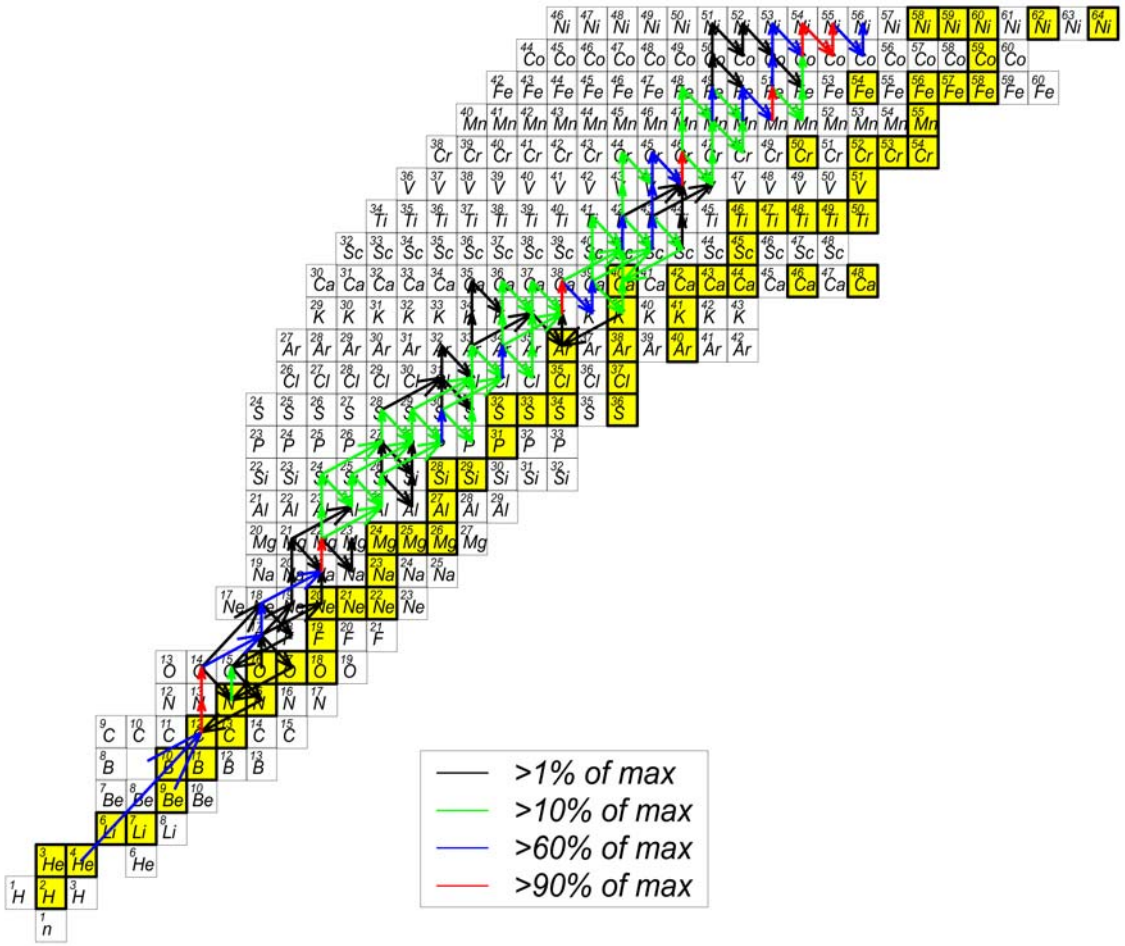

Figure 8.18. Flow with the $^{14}O(\alpha,p)^{17}F$ reaction rate reduced by a factor 10^{-4}. The two paths out of ^{14}O are primarily the $^{14}O(\alpha,p)^{17}F$ reaction and secondarily the weak $^{14}O(\alpha,\gamma)^{18}Ne$ reaction.

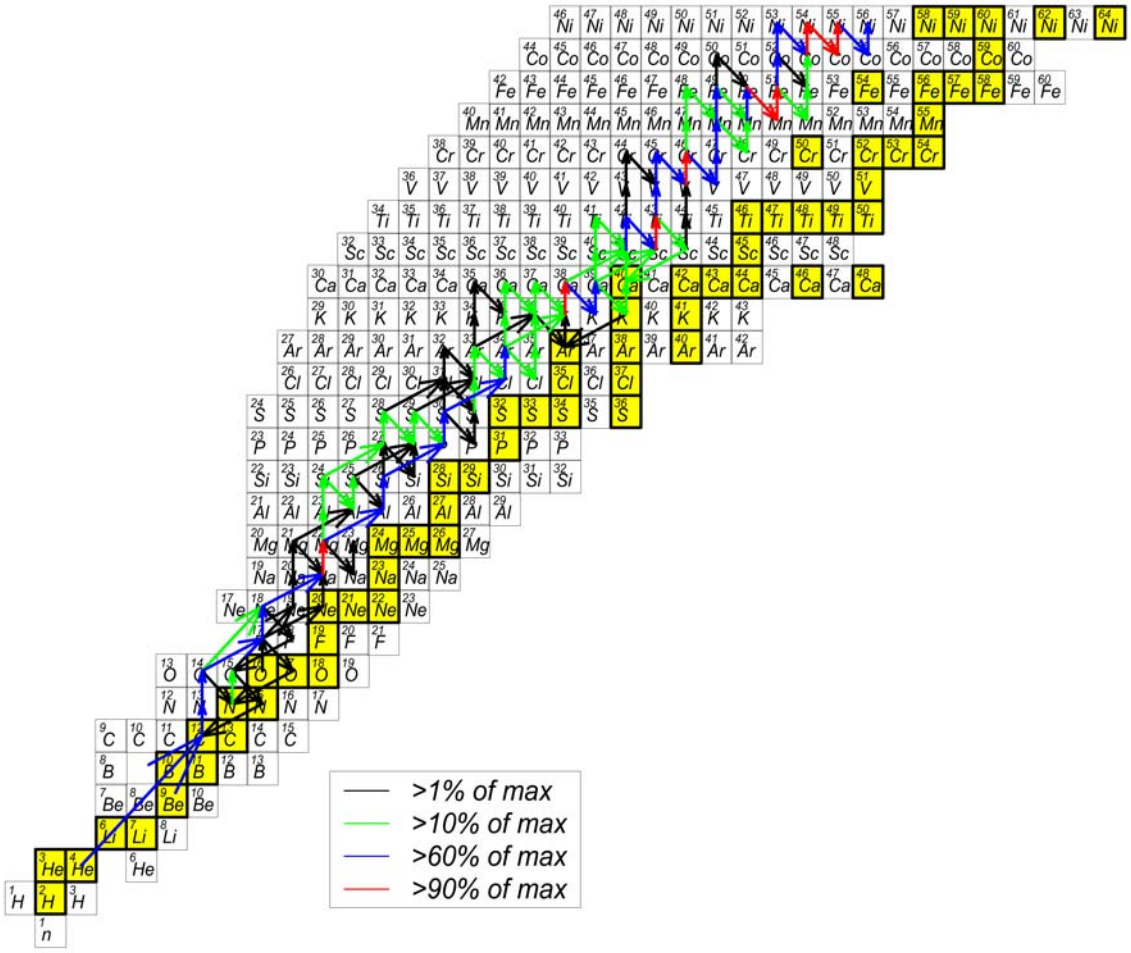

Figure 8.19. Flow with the $^{14}O(\alpha,p)^{17}F$ reaction rate reduced by a factor 10^{-5}. The two paths out of ^{14}O are primarily the $^{14}O(\alpha,p)^{17}F$ reaction and secondarily a relatively stronger $^{14}O(\alpha,\gamma)^{18}Ne$.

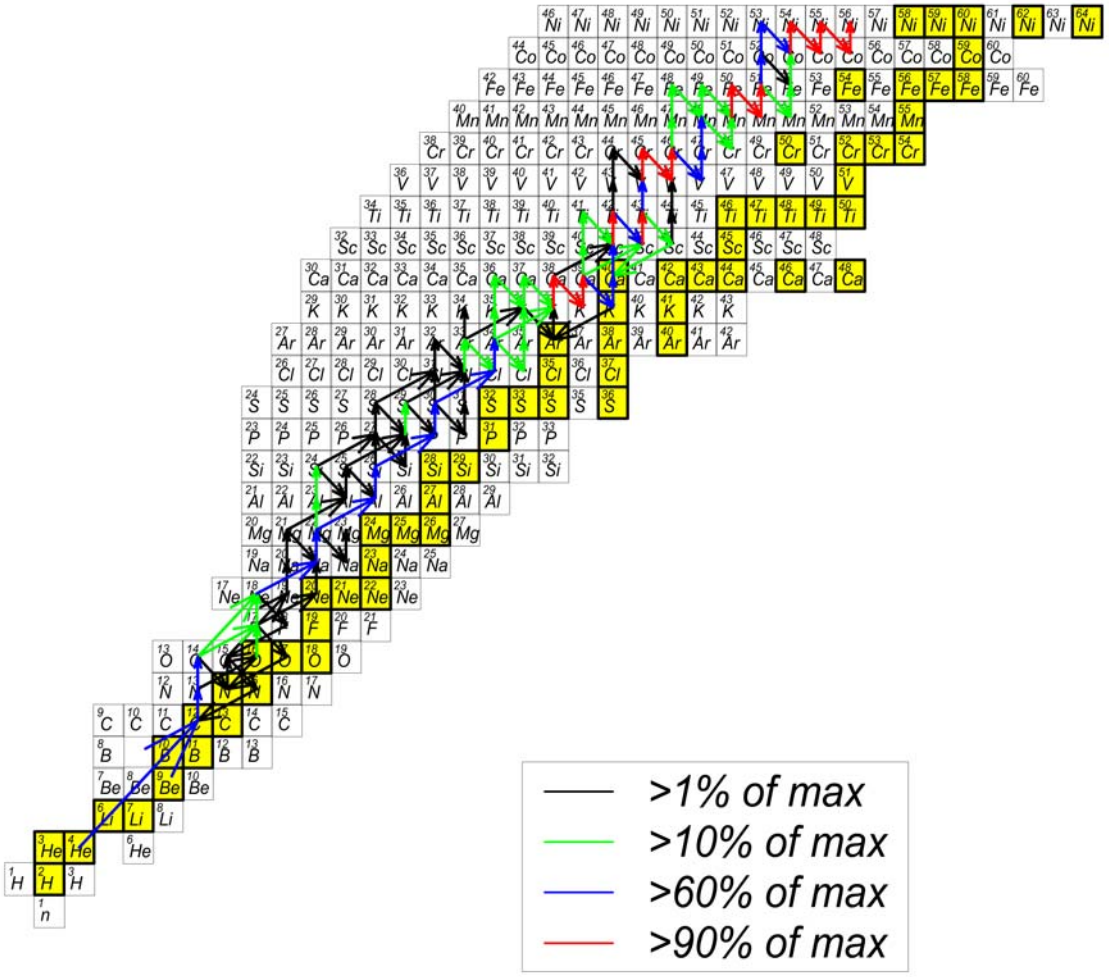

Figure 8.20. Flow with the $^{14}O(\alpha,p)^{17}F$ reaction rate reduced by a factor 10^{-6}. The two paths out of ^{14}O are $^{14}O(\alpha,p)^{17}F$ and $^{14}O(\alpha,\gamma)^{18}Ne$.

8.3 $^{14}O(\alpha,p)^{17}F$ Not Dominant (Factors 10^{-7} to 10^{-9})

A factor of 10^{-7} represents the limiting case when the $^{14}O(\alpha,p)^{17}F$ is not the dominant reaction path out of ^{14}O, while even smaller factors further reduce the importance of $^{14}O(\alpha,p)^{17}F$. The reaction flow between ^{14}O and ^{34}Ar for a factor of 10^{-7} (figure 8.21) reveals a different path toward the mass A=100 region than the reference case. ^{14}O is converted to ^{18}Ne by the reaction $^{14}O(\alpha,\gamma)^{18}Ne$, which is immediately converted to ^{22}Mg through $^{18}Ne(\alpha,p)^{21}Na(p,\gamma)^{22}Mg$. The reaction flow is then dominated by three consecutive (α,p)-(p,γ) reactions until the waiting point ^{34}Ar. The remainder of the reaction flow toward the A=100 mass region is dominated by the rp process, similar to the case in figure 8.1.

The different flows out of ^{22}Mg paint a comprehensible portrait of the distinction between the $^{14}O(\alpha,p)^{17}F$ rate being dominant or not. Figure 8.22 shows the build up toward ^{22}Mg and the eventual depletion of ^{22}Mg for the reference case of the $^{14}O(\alpha,p)^{17}F$ rate. The major flow out of ^{14}O is the (α,p) reaction to ^{17}F, with ^{17}F being instantly converted to ^{22}Mg during the burst. The most likely path out of ^{22}Mg is the (p,γ) reaction to ^{23}Al, with ^{23}Al directly converted to the waiting point isotope, ^{24}Si, by another (p,γ) reaction (see figure 8.1).

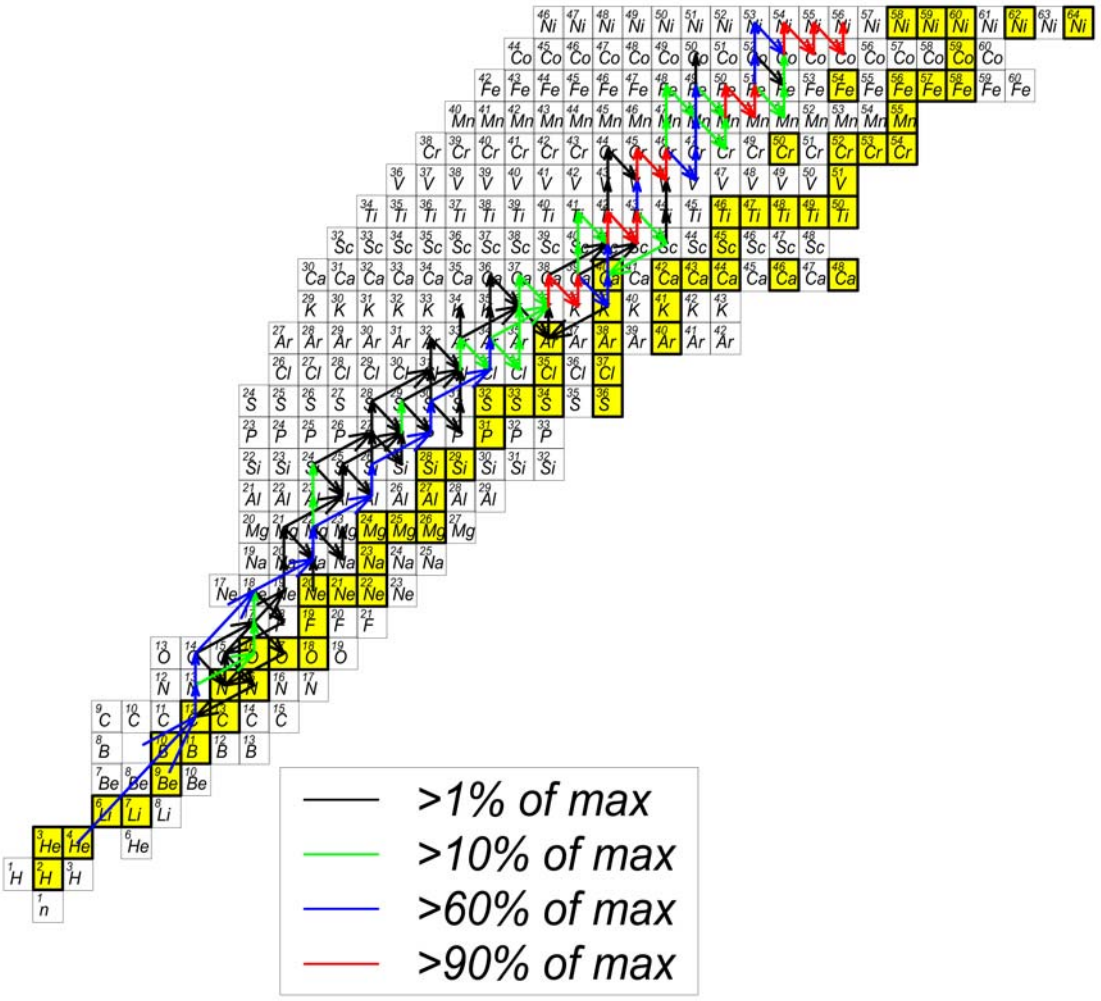

Figure 8.21. Flow with the $^{14}O(\alpha,p)^{17}F$ reaction rate reduced by a factor 10^{-7}. The two paths out of ^{14}O are primarily the $^{14}O(\alpha,\gamma)^{18}Ne$ reaction and the weaker $^{14}O(\alpha,p)^{17}F$ reaction.

The production and depletion of ^{22}Mg when the ^{14}O(α,p) ^{17}F rate is reduced by a factor of 10^{-7} is shown in figure 8.23. When the rate is not dominant, the most probable path for ^{22}Mg production is ^{14}O(α,γ) ^{18}Ne(α,p)^{21}Na(p,γ) ^{22}Mg. The depletion of ^{22}Mg occurs through three consecutive interspersed (α,p) and (p,γ) reactions that build toward ^{34}Ar. The three (α,p)-(p,γ) reactions preclude a major flow through the waiting points ^{24}Si and ^{29}S. The by-passing of those waiting points make a difference in the final abundances in the A=20 to A=72 mass region. As a result a comparison of the nucleosynthesis when the rate is reduced by scaling factors of 10^{-7} to 1, reveals that the reduced rate produces anywhere from 20 to 60 times lower abundances in the region A=20 to A=72 (see Figures 8.14-8.16). The CNO isotopes are also depleted by a factor of 7.

Figure 8.24 is a comparison of figure 8.22 and 8.23; it discloses a one second delay of the burst when the ^{14}O(α,p) ^{17}F rate is not dominant. Because of the delay, the burst will occur at higher temperatures when the ^{14}O(α,p) ^{17}F rate is not dominant. As a result more alpha burning occurs when the ^{14}O(α,p) ^{17}F rate is reduced by a factor of 10^{-7} compare to that of the accepted^{14}O(α,p) ^{17}F rate . As seen in fig. 8.21, the reaction flow between ^{14}O and ^{34}Ar is dominated by (α,p) and (p,γ) reactions. Over that

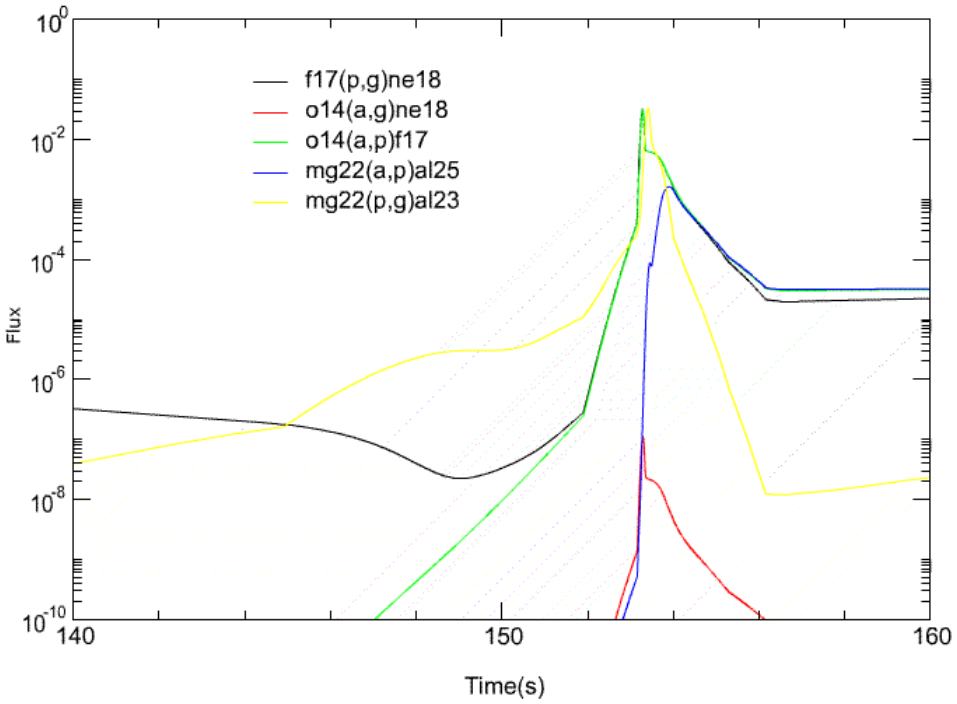

Figure 8.22. The most probable path for creation of ^{22}Mg during an XBR is ^{14}O(α,p) ^{17}F, with ^{17}F being instantly converted to ^{22}Mg. The most probable path for destruction of ^{22}Mg is ^{22}Mg(p,γ).

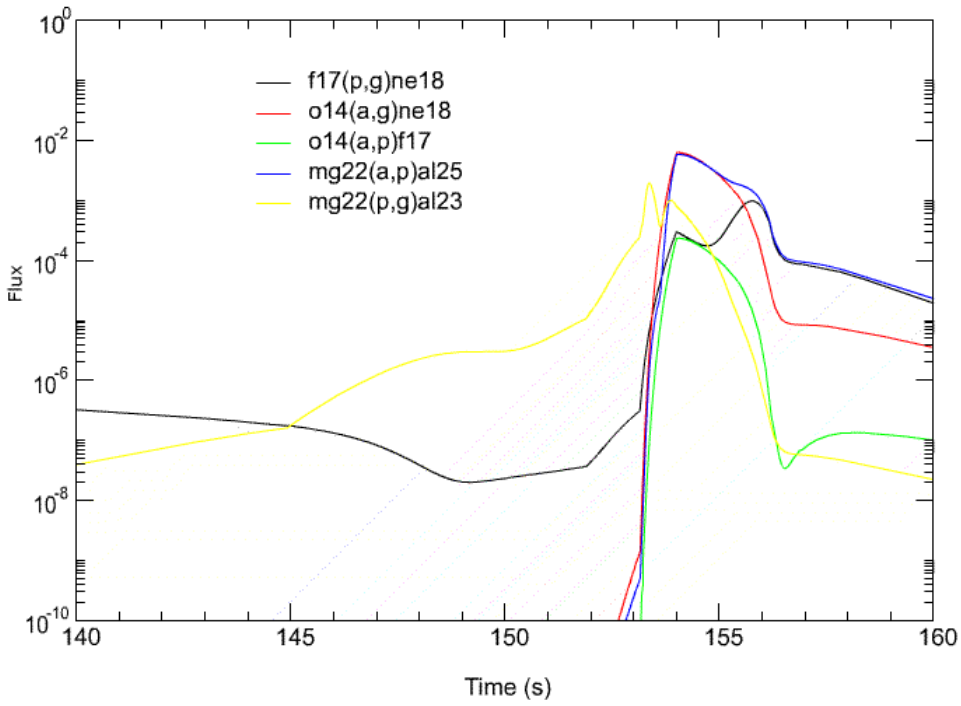

Figure 8.23. When the $^{14}O(\alpha,p)^{17}F$ rate is greatly reduced (multiplied by a factor of 10^{-7} or smaller) the most probable path creation for ^{22}Mg is $^{14}O(\alpha,\gamma)^{18}Ne$, with ^{18}Ne being instantly converted to ^{22}Mg. The most probable path for destruction of ^{22}Mg is $^{22}Mg(\alpha,p)^{23}Al$.

region more helium is burnt than protons, and during the peak of the burst considerably more helium is burnt (Fig 8.25). The mass region A>72 remained unperturbed when the $^{14}O(\alpha,p)^{17}F$ rate is reduced by 10^{-7}. The stability of this mass region against the effect of the $^{14}O(\alpha,p)^{17}F$ not being dominant can be explained by the movement of matter to the top of the network.

The progress of matter occurs in two stages during the simulation. In the first phase, the initial abundances are processed quickly to heavy masses A>72, which is when the more massive isotopes are created. The second phase is late time burning, which is when the abundances in the mass region A=20-72 are created. Reducing the $^{14}O(\alpha,p)^{17}F$ reaction rate by a factor of 10^{-7} has a direct effect on the A=20-72 mass region while the mass region A>72 remained unperturbed because the dearth of helium causes a dearth of ^{12}C production for late time. As a result we observed a deficiency in the mass A=20-72 region which is produced during late time burning.

The energy production of the $^{14}O(\alpha,p)^{17}F$ rate in when reduced by 10^{-7} displays four discrete phases similar to the case of the accepted $^{14}O(\alpha,p)^{17}F$ rate. Figure 8.26 shows evidence of distinction between the cases of the known rate and that of the rate being reduced by a factor of 10^{-7}. The first of

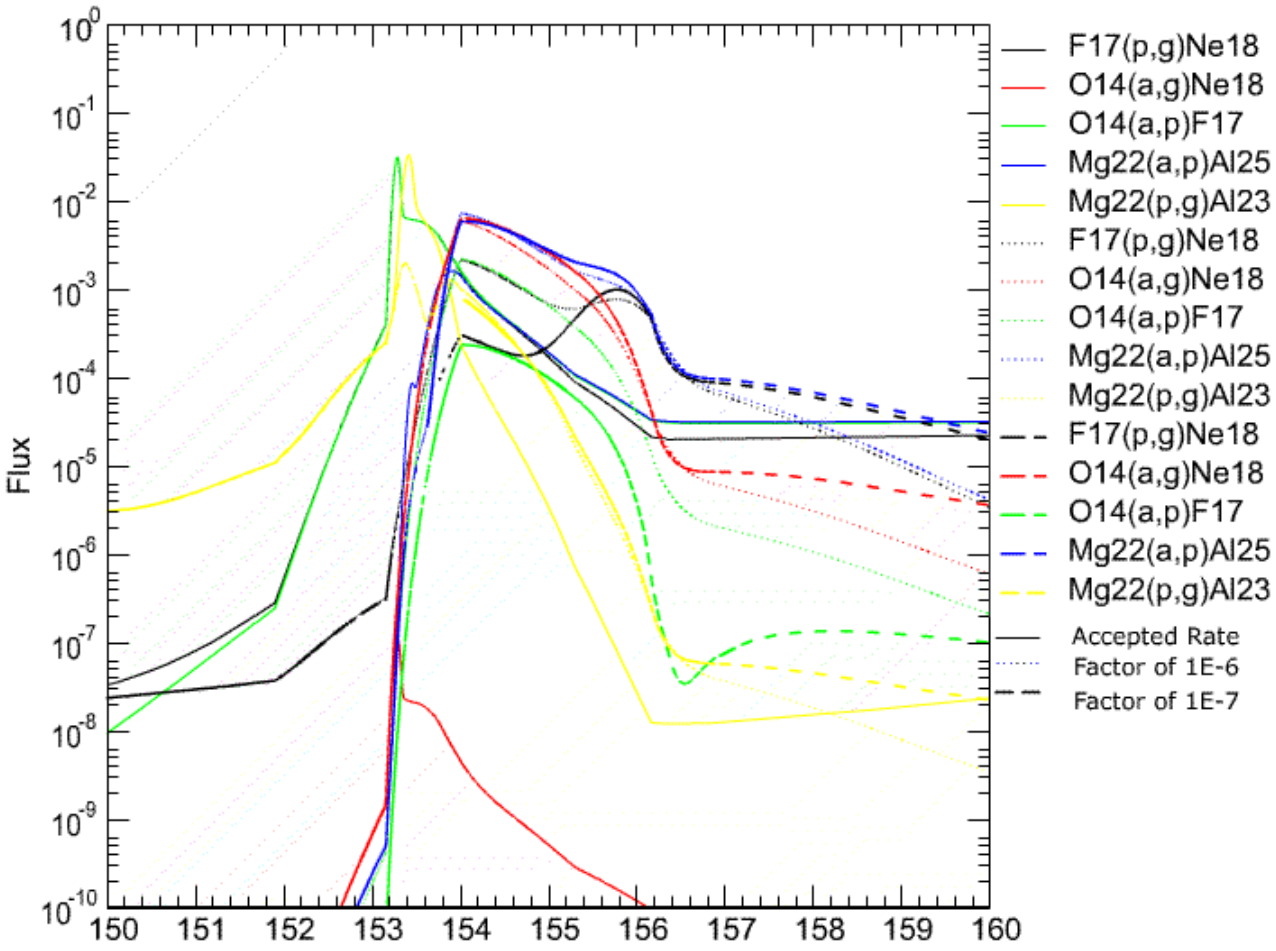

Figure 8.24. A one second delay is observed between the cases when the $^{14}O(\alpha,p)^{17}F$ rate is reduced by a factor of 10^{-7} and when the accepted rate is used.

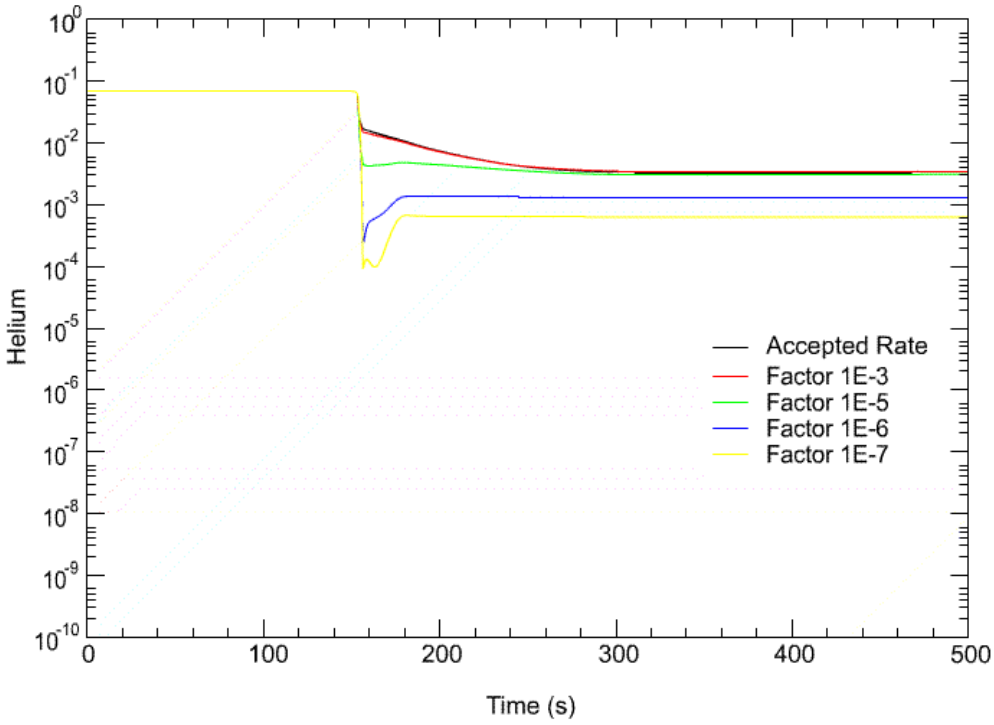

Figure 8.25. More helium is burnt when the $^{14}O(\alpha,p)^{17}F$ is reduced by a factor of 10^{-7} than for the accepted $^{14}O(\alpha,p)^{17}F$ rate.

distinction can be seen in phase (2) of the energy production. The differences in phase two can be seen in term of the temporal width. At a scaling factor of 10^{-7} matter takes different path to break out of the CNO cycle, the alteration in path causes a delay in energy production, which is seen as an increase in width on the energy timescale. The fine structure the two energy productions (see figure 8.26.1) shows the delay at roughly 153 seconds.

This delay allows the burst to occur a greater temperature than the accepted rate thus allowing more helium to burn during the peak of the burst. The delay although unphysical, is seen throughout the remainder of the energy production plot. The next chapter presents the result of the $^{14}O(\alpha, 2p)^{16}O$ rate as it is varied in a similarly to the $^{14}O(\alpha, p)^{17}F$ rate.

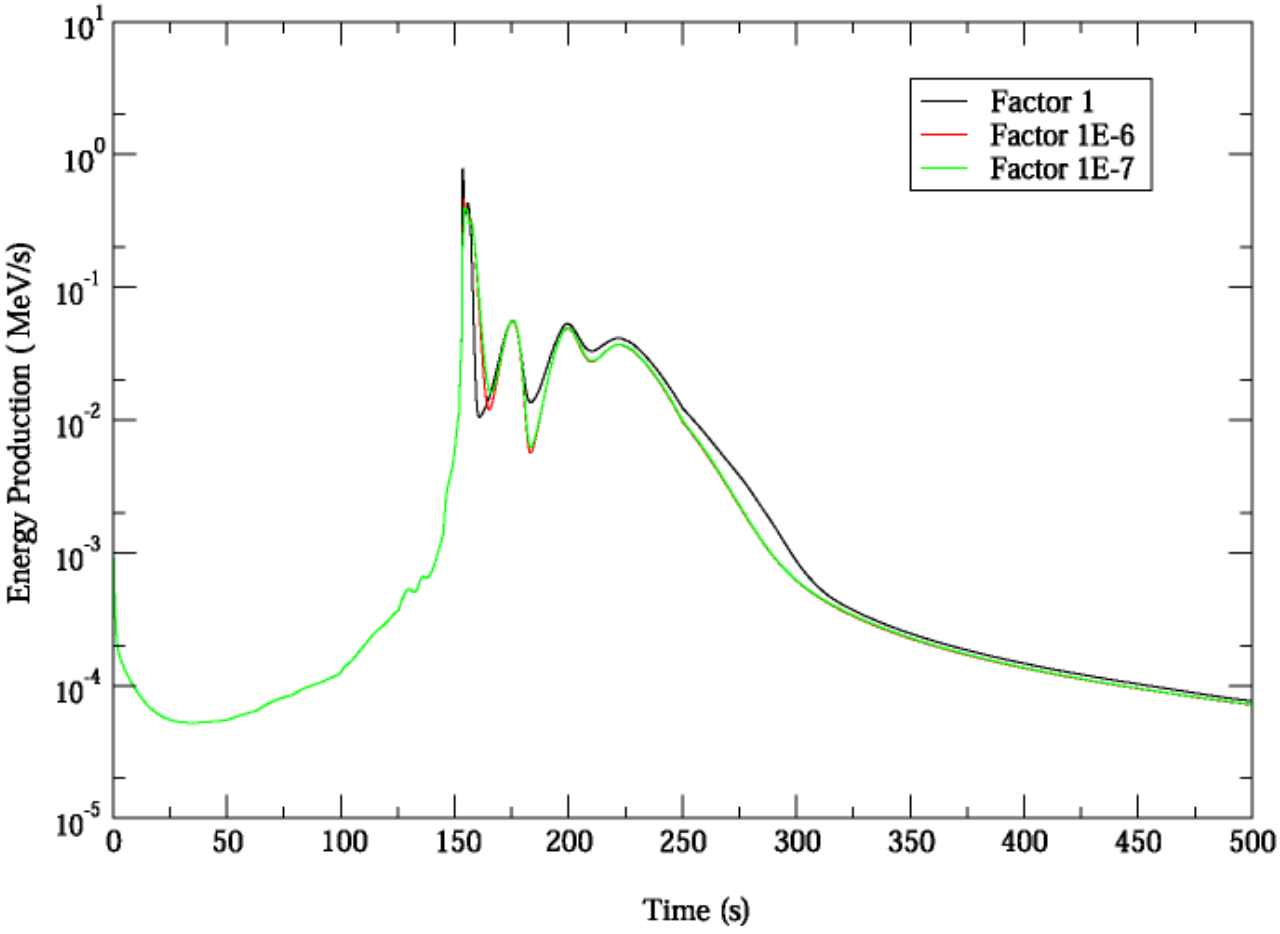

Figure 8.26. The energy production of when the $^{14}O(\alpha,p)^{17}F$ rate is reduced by factors of 10^{-6} and 10^{-7} shows a deficiency in late time energy production.

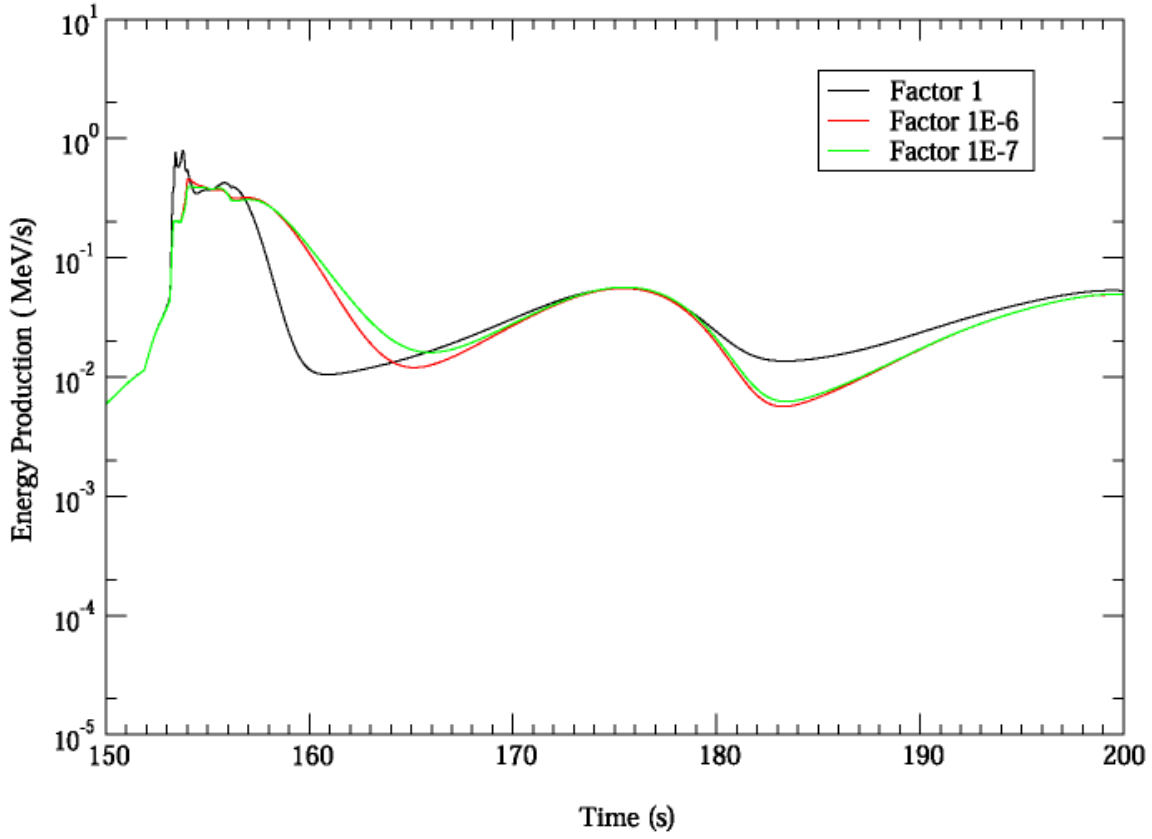

Figure 8.26.1 When the $^{14}O(\alpha,p)^{17}F$ rate is reduced by factors of 10^{-6} and 10^{-7} ; a delay in energy production is observed at roughly 153 seconds when compared to the accepted rate. This delay will affect the late time nucleosynthesis during energy production

Chapter 9
X Ray Burst Results (α,2p) Case

We introduced a new reaction into the reaction rate library, $^{14}O(\alpha, 2p)\,^{16}O$ based on the possible detection of a 2 proton decay out of ^{18}Ne [49] . Since the $^{14}O(\alpha,2p)^{16}O$ reaction is unmeasured we assumed the full strength of the $^{14}O(\alpha, p)\,^{17}F$ rate as substitute for the unknown $^{14}O(\alpha, 2p)\,^{16}O$ rate. This new reaction is than varied in strength over 12 orders magnitudes (competing with the known $^{14}O(\alpha, p)\,^{17}F$ rate). As we steadily increased the rate by factors of 10, we analyzed the flux diagrams, the variation of fluxes in time, the energy production, the variation of abundances in time, and the abundance ratios versus atomic mass.

Figures 9.1-9.6 display the ratio of final abundances produced by the network with the varied rates for $^{14}O(\alpha,2p)^{16}O$ to the final abundances produced by the network with the accepted rate for $^{14}O(\alpha,p)^{17}F$ without the $^{14}O(\alpha, 2p)\,^{16}O$ rate. Each final abundance ratio is plotted versus the atomic mass. From these plots we study the effect of the varied $^{14}O(\alpha,2p)^{16}O$ rate on the final abundances, and we will describe three sets of variations: 10^{-9} to 10^{-1}, 1,10 to 1000.

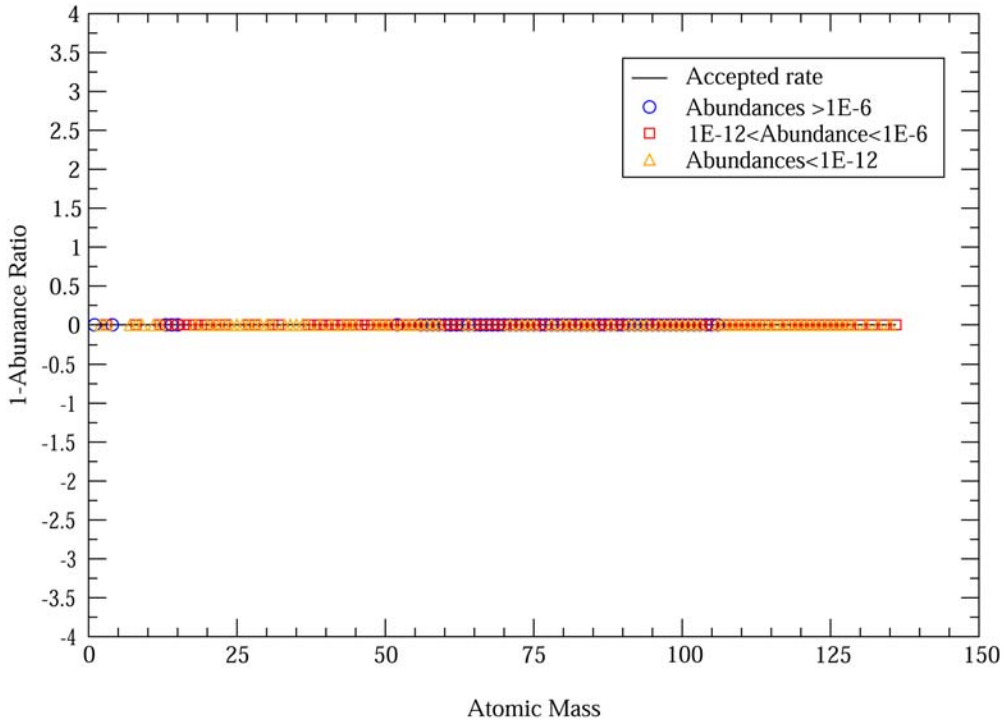

Figure 9.1. The final abundance ratio as a function of atomic mass when the $^{14}O(\alpha,2p)^{16}O$ rate is reduced by a factor of 10^{-9} relative to the accepted $^{14}O(\alpha,p)^{17}F$ rate. When the $^{14}O(\alpha,2p)^{16}O$ rate is reduced, the $^{14}O(\alpha,p)^{17}F$ dominates.

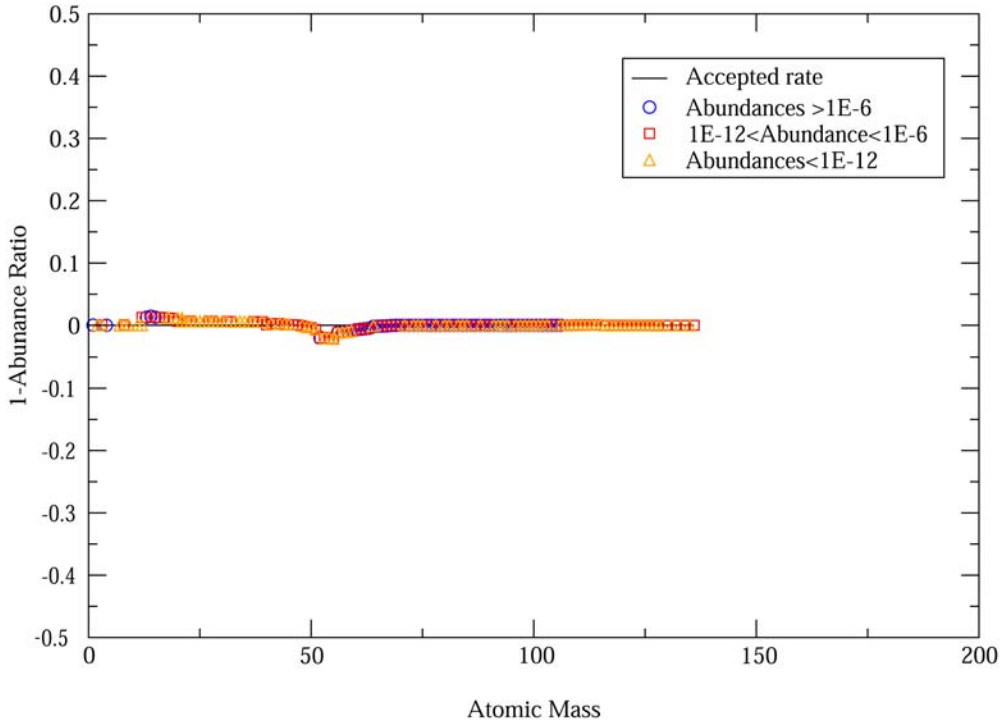

Figure 9.2. The final abundance ratio as a function of atomic mass when the $^{14}O(\alpha,2p)^{16}O$ rate is reduced by a factor of 10^{-1} relative to the accepted $^{14}O(\alpha,p)^{17}F$ rate. When the $^{14}O(\alpha,2p)^{16}O$ rate is slightly reduced, the $^{14}O(\alpha,p)^{17}F$ dominates.

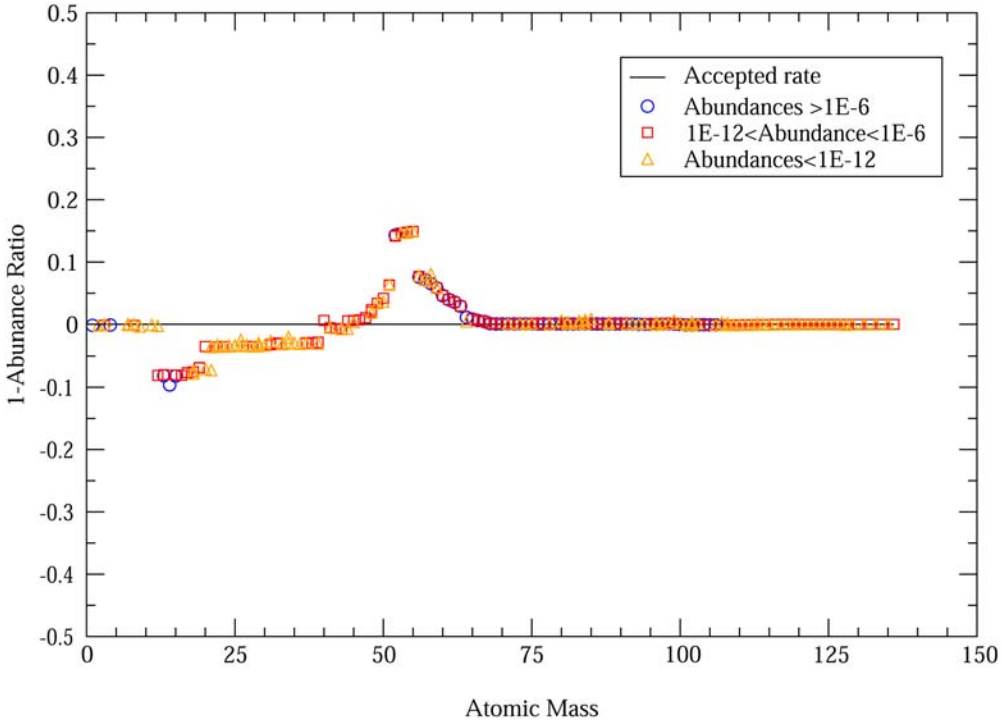

Figure 9.3. The final abundance ratio as a function of atomic mass when the $^{14}O(\alpha,2p)^{16}O$ rate is equal in strength to the accepted $^{14}O(\alpha,p)^{17}F$ rate. The enhancement of the $^{14}O(\alpha,2p)^{16}O$ rate enhances the flow of matter out of the CNO isotopes toward the A=20-72 region.

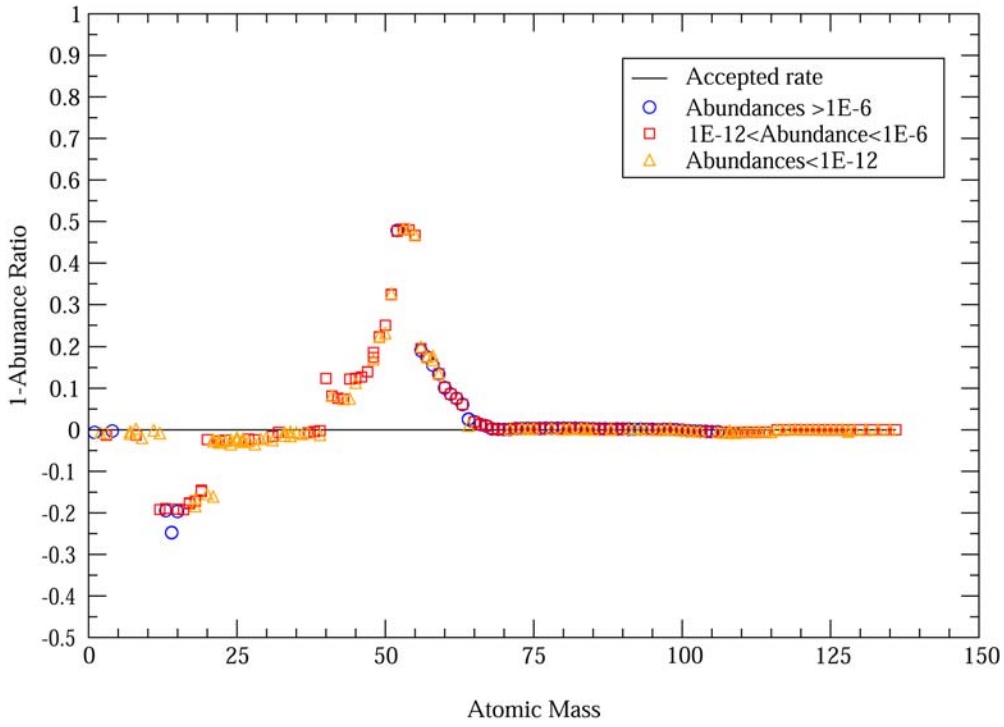

Figure 9.4. The final abundance ratio as a function of atomic mass when the $^{14}O(\alpha,2p)^{16}O$ rate is a factor of 10 larger times the accepted $^{14}O(\alpha,p)^{17}F$ rate. The enhancement of the $^{14}O(\alpha,p)^{16}O$ rate by a factor of 10 further enhances the flow of matter out of the CNO isotopes toward the A=20-72 region.

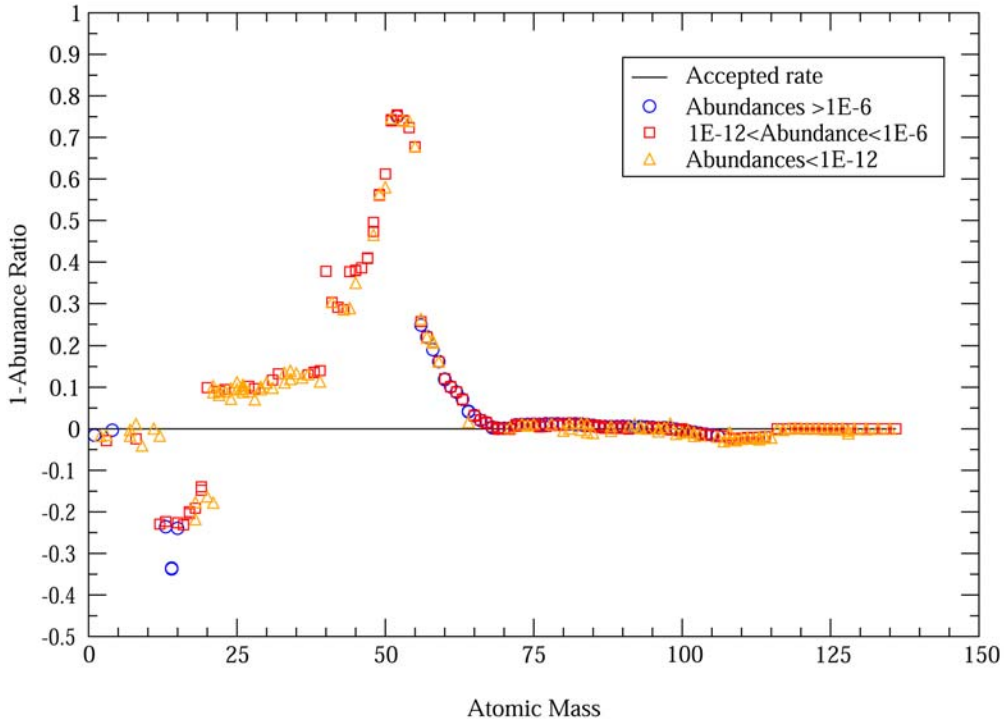

Figure 9.5. The final abundance ratio as a function of atomic mass when the $^{14}O(\alpha,2p)^{16}O$ rate is a factor of 100 larger times the accepted $^{14}O(\alpha,p)^{17}F$ rate. The $^{14}O(\alpha,2p)^{16}O$ rate saturates and does not enhance much greater than for a factor of 100.

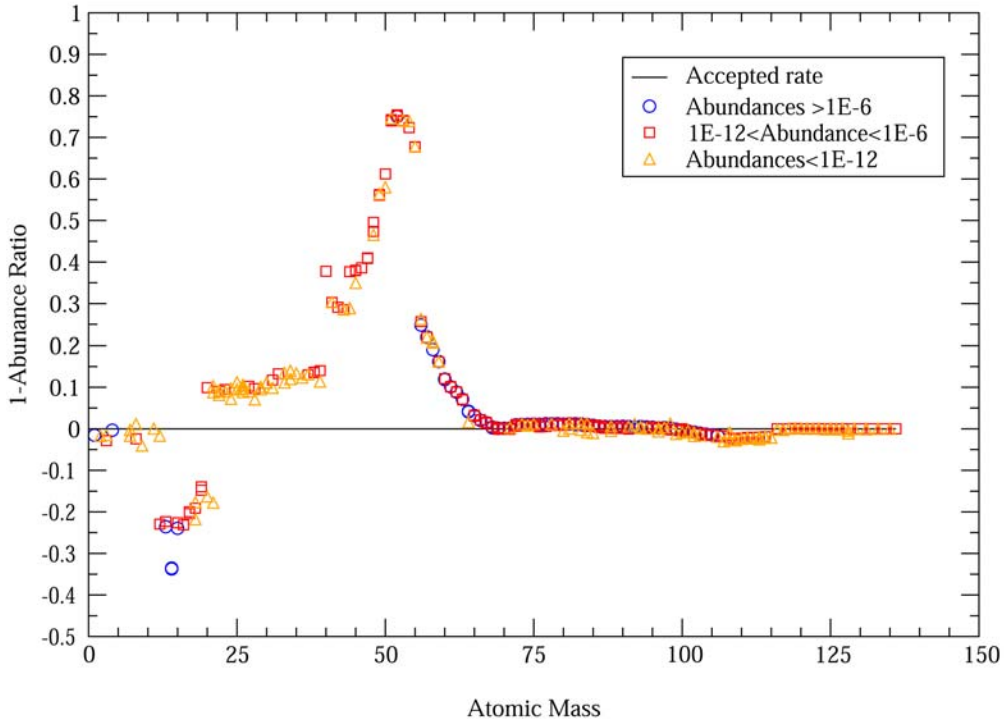

Figure 9.6. The final abundance ratio as a function of atomic mass when the $^{14}O(\alpha,2p)^{16}O$ is a factor of a 1000 larger times the accepted $^{14}O(\alpha,p)^{17}F$ rate.

When the unknown $^{14}O(\alpha,2p)^{16}O$ rate is multiplied by factors between 10^{-1} and 10^{-9}, the competing $^{14}O(\alpha,p)^{17}F$ reaction is the dominant path out of ^{14}O (see Figure 9.7). We find the build up toward the A=100 mass region is the same with that of the accepted $^{14}O(\alpha, p)^{17}F$ rate. At factors between 10^{-4} to 10^{-9} the path is dominated by $^{14}O(\alpha,p)^{17}F$ reaction with no contribution by the unknown $^{14}O(\alpha,2p)^{16}O$ reaction (see figure 9.8) . As a result, we observed less than 1% of changes in the final abundances and no change in energy production when compared to the accepted $^{14}O(\alpha, p)^{17}F$ rate. When the unknown $^{14}O(\alpha,2p)^{16}O$ rate is mildly reduced by a factor of 10^{-1}, a weak contribution from the unknown rate is observed. Thus the destruction of ^{14}O occurs primarily via the $^{14}O(\alpha,p)^{17}F$ reaction and secondarily via the unknown $^{14}O(\alpha,2p)^{16}O$ reaction, with the ^{16}O immediately converted to ^{17}F through $^{16}O(p,\gamma)^{17}F$ where the two paths converge. The path beyond ^{17}F toward A=100 mass region is consistent with figure 8.1. Thus we observe no significant change in either the final abundances or the energy production when compared to the known $^{14}O(\alpha,p)^{17}F$ rate .

The second regime is for the $^{14}O(\alpha,2p)^{16}O$ reaction rate set at equal strength to the $^{14}O(\alpha,p)^{17}F$ reaction. The destruction of ^{14}O occurs simultaneously via $^{14}O(\alpha,p)^{17}F$ and $^{14}O(\alpha,2p)^{16}O$ (see figure 9.9). Again the

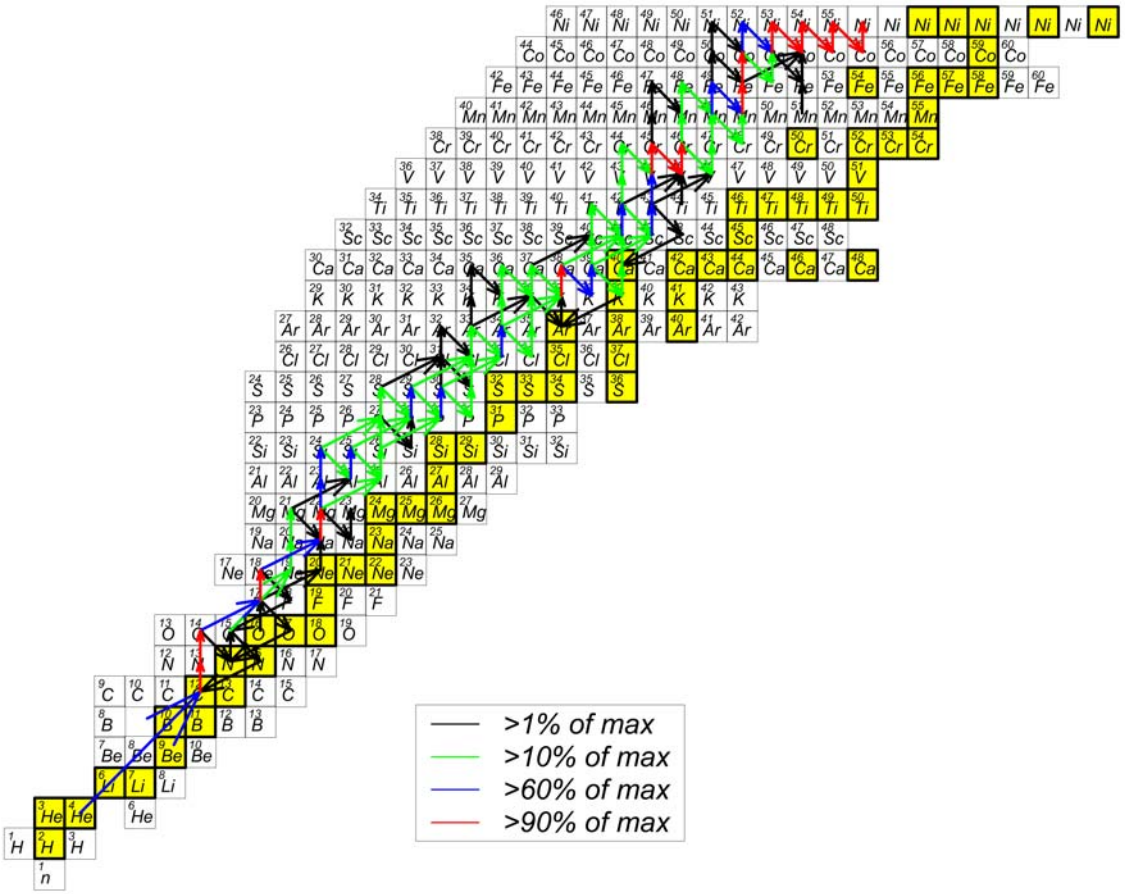

Figure 9.7. Flow with the $^{14}O(\alpha,2p)^{16}O$ reaction rate reduced by a factor of 10^{-2} times the accepted $^{14}O(\alpha,p)^{17}F$ reaction. The destruction of ^{14}O occurs via the $^{14}O(\alpha,p)^{17}F$ reaction.

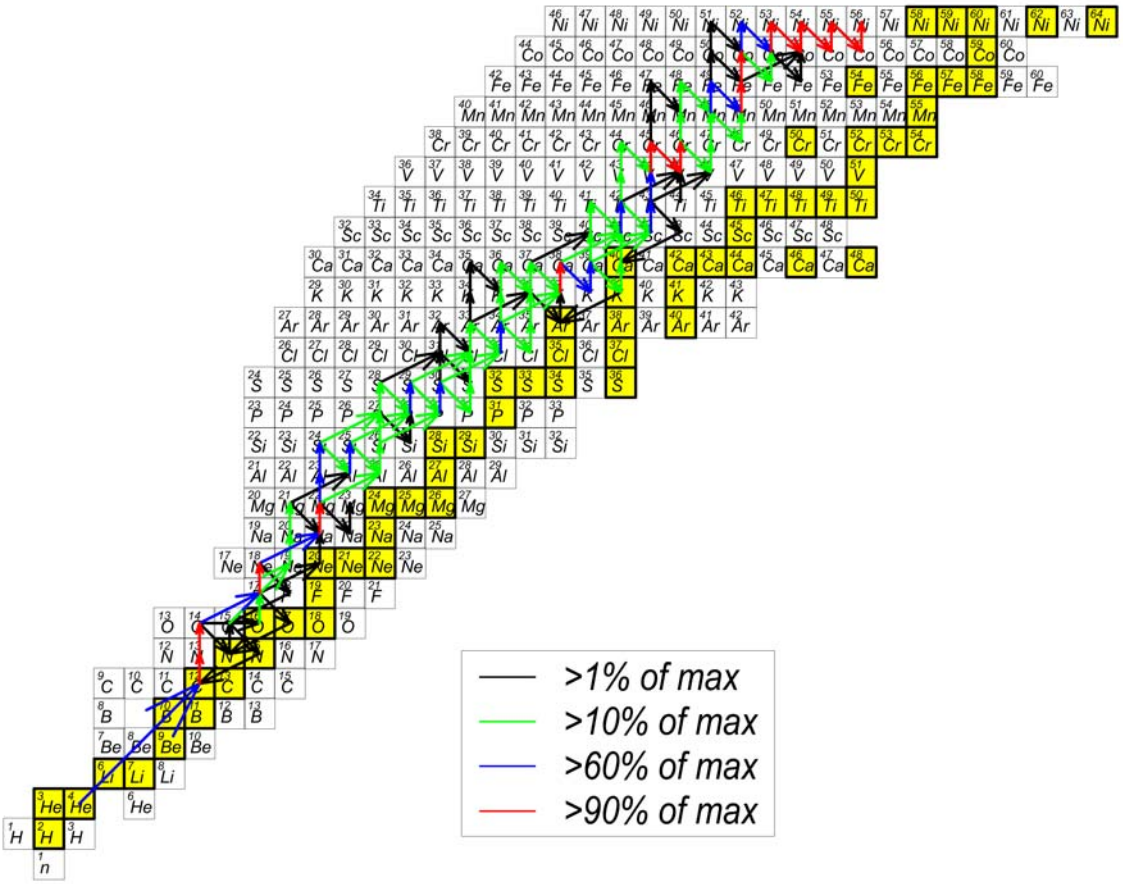

Figure 9.8. Flow with the $^{14}O(\alpha,2p)^{16}O$ reaction rate reduced by a factor of 10^{-1} times the accepted $^{14}O(\alpha,p)^{17}F$ reaction. The destruction of ^{14}O occurs primarily via the $^{14}O(\alpha,p)^{17}F$ reaction with the $^{14}O(\alpha,2p)^{16}$ reaction contributes weakly.

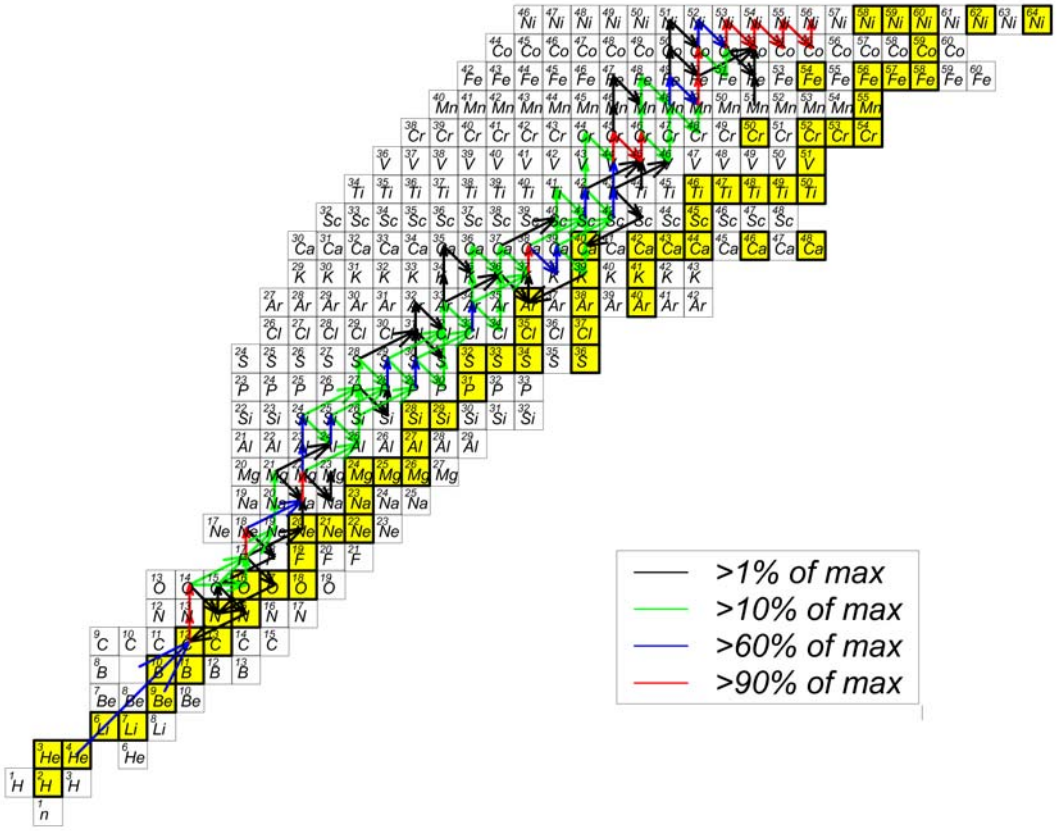

Figure 9.9. Flow with the $^{14}O(\alpha,2p)^{16}O$ reaction rate at equal strength to the accepted $^{14}O(\alpha,p)^{17}F$ reaction.

two paths converge at ^{17}F and the flow to the top of the mass region A=100 is again consistent with fig 8.1. We observed changes in the ^{14}O and ^{16}O isotopes, which changes by 10% and 8% respectively and ^{56}Ni is enriched by 8% when compared to the case using the accepted $^{14}O(\alpha,p)^{17}F$ rate. The energy production is consistent with the accepted $^{14}O(\alpha,p)^{17}F$ reaction rate.

When the unknown $^{14}O(\alpha,2p)^{16}O$ reaction rate is multiplied by factors of 10 or greater, the destruction of ^{14}O occurs primarily through $^{14}O(\alpha,2p)^{16}O(p,\gamma)^{17}F$ and secondarily through $^{14}O(\alpha,p)^{17}F$. As a result, the flow diagram is now dominated by the $^{14}O(\alpha,2p)^{16}O$ reaction (figure 9.10), with the ^{16}O immediately converted to ^{17}F by the reaction $^{16}O(p,\gamma)^{17}F$. At a factor of 10, ^{14}O is depleted by 25% and ^{16}O is depleted by 20%, while ^{56}Ni is enriched by 20 % when compared to the case using the accepted $^{14}O(\alpha,p)^{17}F$ rate. The energy production is consistent with the accepted $^{14}O(\alpha,p)^{17}F$ reaction . Enhancing the $^{14}O(\alpha,2p)^{16}O$ by a factor of 100 further depleted ^{14}O and ^{16}O by 33% and 24% respectively while ^{56}Ni is enriched by 25% when compared to the referenced case. The behavior of the $^{14}O(\alpha,2p)^{16}O$ reaction rate multiplied by factors of 1 and greater is similar to that of the $^{14}O(\alpha,p)^{17}F$ reaction rate multiplied by factors greater than 10. This

behavior suggests that the (α,p) branch out of ^{14}O is faster than the (α,2p) branch out of ^{14}O.

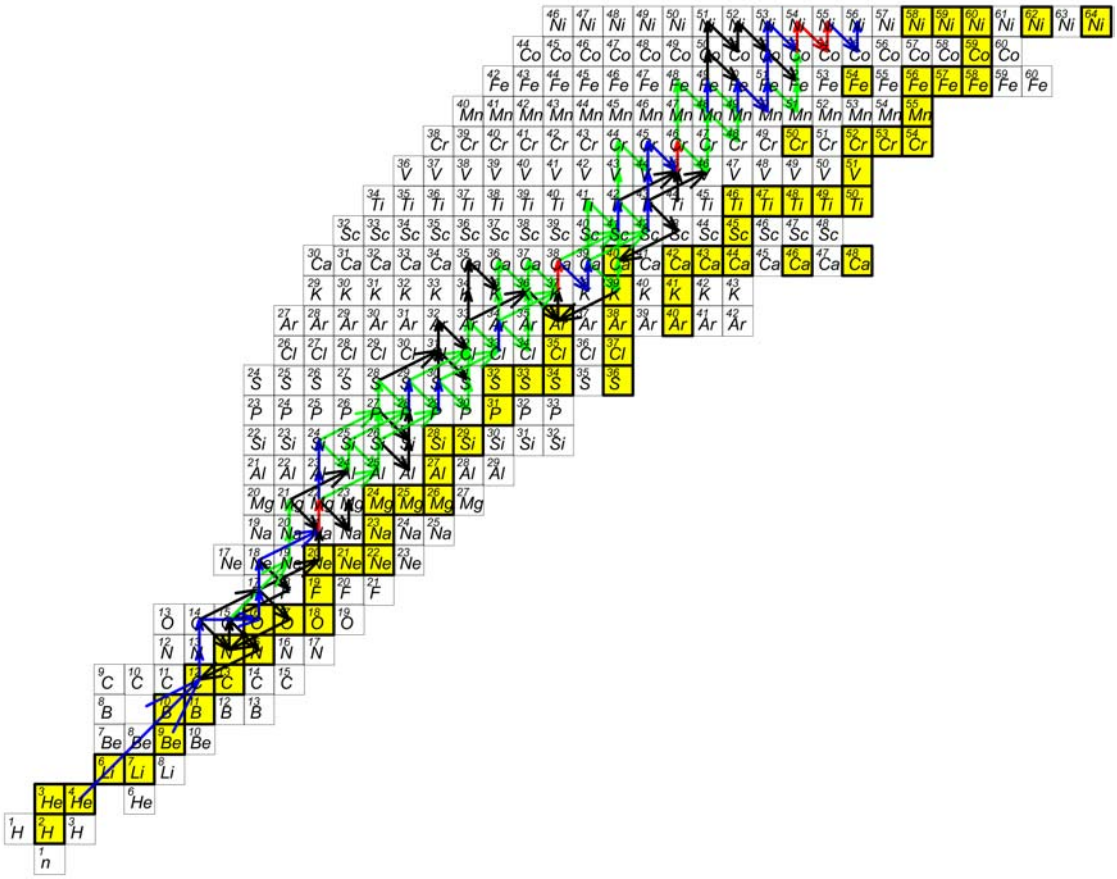

Figure 9.10. Flow with the $^{14}O(\alpha,2p)^{16}O$ reaction rate larger by a factor of 10 to the accepted $^{14}O(\alpha,p)^{17}F$ reaction rate. The destruction of ^{14}O occurs primarily via the $^{14}O(\alpha,2p)^{16}$ reaction with $^{14}O(\alpha,p)^{17}F$ contributing weakly.

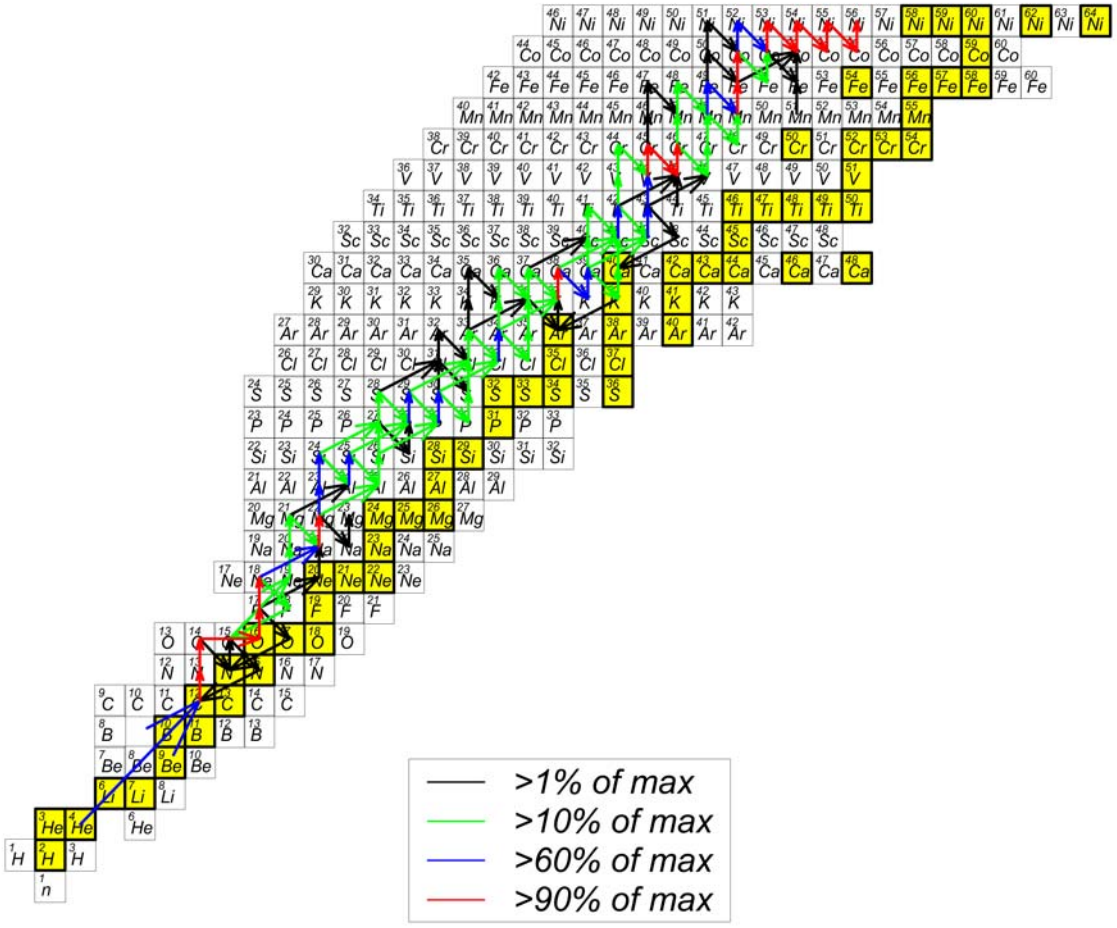

Figure 9.11. Flow with the $^{14}O(\alpha,2p)^{16}O$ reaction rate larger by a factor of 100 to the accepted $^{14}O(\alpha,p)^{17}F$ reaction rate. The destruction of ^{14}O occurs primarily via the $^{14}O(\alpha,2p)^{16}$ reaction.

Chapter 10
Conclusion

10.1 Summary

Variation of the $^{14}O(\alpha, p)^{17}F$ reaction rate produces an insignificant difference on the final abundances during the three nova simulations studied. We find that the $^{14}O(\alpha, p)^{17}F$ rate does not have any influence on final abundances or energy generation in the three representative novae simulations. This shows that the temperatures associated with novae are too low for the $^{14}O(\alpha, p)^{17}F$ reaction to play a crucial role. When the unknown $^{14}O(\alpha,2p)^{16}O$ rate is introduced with values varied over a large range, we also observed no significant difference in the nova nucleosynthesis. We found that the competition between the $^{14}O(\alpha, p)^{17}F$ and $^{14}O(\alpha,2p)^{16}O(p,\gamma)^{17}F$ reactions pathways only changed the final abundance of ^{14}O and ^{16}O.

Temperatures during X ray bursts are sufficiently high to break out of the CNO cycle through the $^{14}O(\alpha,p)^{17}F$ reaction. I pulled together the tools to do of X-ray burst calculations; the nuclear reaction network and an extended reaction rate library. I wrote a shell to the nuclear reaction network

that allows me to change the reaction rate in the nuclear rate library, I wrote many other programs for analysis.

Variation of the $^{14}O(\alpha, p)^{17}F$ rate shows depletion in the A=20-72 mass region by factors up to 60 when the $^{14}O(\alpha,p)^{17}F$ reaction rate is greatly reduced (multiplied by 10^{-6} or smaller). The CNO isotopes and A=20-50 are enriched up to 25% while the A=51-72 mass region are depleted by as much as 30% when the $^{14}O(\alpha,p)^{17}F$ rate is multiplied by factors between 10^{-3} and 10^{-5}. The γ-ray source ^{56}Ni is a good observable candidate. When the rate is multiplied by factors between 1 and 10^{3} the CNO and A=20-50 are depleted by as much as 33% while the A=51-72 is enhanced by as much as much as 25%.

When the $^{14}O(\alpha,2p)^{16}O$ reaction rate was introduced, we observed an insignificant of difference in the final abundances when the unknown $^{14}O(\alpha,2p)^{16}O$ reaction rate was multiplied by 10^{-1} the accepted $^{14}O(\alpha, p)^{17}F$ rate or less. We found varying the unknown $^{14}O(\alpha,2p)^{16}O$ rate by factors of 1 and greater only change the final abundance of the ^{14}O isotope by 3% and the ^{16}O isotope by 10% . We found the $^{14}O(\alpha,2p)^{16}O$ rate, when multiplied by a factors of 1 or greater to produce changes similar to those observed for the $^{14}O(\alpha,p)^{17}F$ rate multiplied by factors of 10 or greater.

10.2 Discussion

Many of the nuclear reactions of importance in nuclear astrophysics, especially is stellar explosions, occur on radioactive (unstable) nuclei. To further understand nucleosynthesis in exploding stars, it is important to study the reactions involving those radioactive nuclei. The reaction rates for those unstable nuclei are determined by either theoretical calculations (Hauser Feshbach) or in laboratory experimental measurements. Determinations of reaction rates by both methods can have significant uncertainties. While there are large uncertainties in many astrophysics reactions, for example, the $^{14}O(\alpha,p)^{17}F$ reaction rate has an uncertainty of a factor of 10^3. A very recent experiment at Oak Ridge National Laboratory has found the $^{14}O(\alpha,p)^{17}F$ reaction rate to be greater by a factor of 30 [66] than that of the currently accepted $^{14}O(\alpha,p)^{17}F$ rate. According to this work, this corresponds to a difference of less than 3% the final abundances and no difference on energy production. Our variation of this rate by many orders of magnitude shows the role that this reaction plays in a number of astrophysical environments.

Figure 8.26 compares the energy production when the $^{14}O(\alpha,p)^{17}F$ rate is at full strength to when it is greatly reduced (multiplied by 10^{-7}). This comparison shows a one second delay between the two cases after 153 seconds. Given that difference, we conclude that reactions other than $^{14}O(\alpha,p)^{17}F$ are responsible for the energy production prior to a time of 153 seconds. The thermodynamics behavior after 153 seconds is heavily influenced by the rate of $^{14}O(\alpha,p)^{17}F$. Therefore by turning the rate as far down as 10^{-7}, our post-processing assumptions break down. To be consistent in our understanding of the energy production at a factor of 10^{-7} of the known rate, we would need to incorporate the delay that occurs at 153 seconds into the thermodynamic profile of the burst that would avoid the rise in temperature we observed during the delay. Instead the temperature would be lower; therefore the reaction rate would be lower.

The reaction flow diagram with the $^{14}O(\alpha,p)^{17}F$ rate greatly reduced demonstrates the resilience of breakout under X-ray burst conditions: that another reaction serves as a breakout path if $^{14}O(\alpha,p)^{17}F$ is greatly reduced, with only minor changes in the final abundances. The reaction rate $^{15}O(\alpha,\gamma)^{19}Ne$ is frequently suggested as an alternative breakout path out of the CNO cycle in the literature [26,28]. However, $^{15}O(\alpha,\gamma)^{19}Ne$ reaction

depends on populating ^{15}O through the reaction $^{14}O(\beta^{+}\nu)^{14}N(p,\gamma)^{15}O$, and the β-decay is slow compared to particle capture on ^{14}O . We therefore find it more probable $^{14}O(\alpha,\gamma)^{18}Ne$ is an possible additional path for breakout of the CNO cycle then $^{15}O(\alpha,\gamma)^{19}Ne$. We also find that the $^{14}O(\alpha,2p)^{16}O$ reaction rate serves only as a boost to the $^{14}O(\alpha,p)^{17}F$ reaction since $^{16}O(p,\gamma)^{17}F$ follows rapidly and both paths end up at the same place, ^{17}F. The difference in nucleosynthesis just affects the final abundance of ^{16}O. Thus efforts to measure the $^{14}O(\alpha,2p)^{16}O$ reaction rate are not of great astrophysical interest unless the (α,2p) branch is much faster than the (α,p) branch, which is quite unlikely.

10.3 Future Directions

The uncertainties that are found in experimentally measured reaction rates are often due to the effect of missing or unknown resonances that can change the reaction rate at both nova and X-Ray burst temperatures. We plan to follow this work by performing X-ray burst simulations with the new $^{14}O(\alpha,p)^{17}F$ rate [66], but we already know to xpect an insignificant amount of change in the final abundances. Finally, the codes developed during this research allow one to easily vary any rate in the reaction rate library. Thus

we can test any other reaction rate in the reaction rate library and also test the astrophysical significance of any new measurements or proposed measurements.

REFERENCES

[1] J.M. Pasachoff. *Journey throught the Universe*. New York Saunders Publishing, (1992).
[2] R. Bowers & T. Deeming. *Astrophysics I Stars*. Jones And Bartlett Publishers, Boston, (1984).
[3] M. Wiescher, J. Gorres & H. Schatz. J.Phys. G: Nucl. Part Phys. **25**, R133 (1999).
[4] M.F. Bode & A. Evans. *Classical Nova.* John Wiley & Sons LTD, Chichester, (1989).
[5] R. Bowers & T. Deeming. *Astrophysics II Interstellar Matter and Galaxies*. Jones And Bartlett Publishers, Boston, (1984).
[6] E. Bohm-Vitens. *Stellar Astrophysics Vol 2&3*. Cambrige University Press, Cambdridge (1989).
[7] S. Starrfield, et al,. APJ Supplement **127,** 485 (2000).
[8] F. Rembges, et al,. APJ. **484,** 412-423 (1997).
[9] J.G. Hirsch & D. Page. *Nuclear and Particle Astrophysics*. Cambridge University Press, Cambridge, (1998).
[10] S. Starrfield, et al,. APJ. **258,** 683-695 (1982).
[11] D. Arnett. *Supernovae and Nucleosynthesis*. Princeton University Press (1996).
[12] R. Kippenhan & A. Weigert. *Stellar Structure and Evolution*. Springer-Verlag, Berlin, (1990).
[13] M.G. Edmunds & R.J. Terlevich. *Element and The Cosmo.* Cambridge University Press (1992).
[14] C. Rolfs & W.S. Rodney. *Cauldrons in the Cosmos*. University of Chicago Press, Chicago (1988).
[15] D. Clayton. *Principles of Stellar Evolution and Nucleosynthesis.* University of Chicago Press, Chicago (1983).
[16] M.Guidry, Private Communication, unpublished Astrophysics note.

[17] R.A. Serway, C.J. Moses, & C.A. Moyer. *Modern Physics*. Saunders College Publishing, Orlando Florida, (1989).
[18] J.W.Truan & M.Livio. APJ. **308**, 721 (1986)**.**
[19] A.C. Phillips. *The Physics of Stars*. John Wiley & Sons LTD, Chichester, (1994).

[20] J.E. Pringle & R. A. Wade. *Interacting Binary Stars*. Cambridge

University Press, Cambridge, (1985).
[21] J. Frank, A.R. King & D.J. Raine. *Accretion Power in Astrophysics*. Cambridge University Press, Cambridge, (1985).
[22] K. Nomoto. APJ. **253**, 798 (1982).
[23] D. Prialnik & A. Kovetz. APJ. **281**, 367 (1984).
[24] W.H.G. Lewin & E.P.J. Van Den Heuvel. *Accretion Driven X-ray Sources.* Cambridge University Press, Cambridge (1983).
[25] W.J. Kaufmann. *Universe 4th Edition*. W.H. Freeman and Company, New York, (1994).
[26] F. Kappeler, F.-K. Thielemann & M. Wiescher. AR Nucl. Part. Sci. **48**, 175 (1998).
[27] M. Wiescher, H. Schatz & A.E. Champagne. Phil. Trans. R. Soc. Lon. A **356**, 2105 (1998).
[28] M.S. Smith & K.E. Rehm. AR Nucl. Part. Sci. **51**, 91 (2001).
[29] R. Rosner, et al,. APJ. **562,** L177 (2001).
[30] L. Bildsten, et al,. APJ. **384**, 143 (1992).
[31] G. S. Kutter & W.M. Sparks. APJ. **340**, 985 (1989).
[32] R. D. Gehrz, et al,. Astronomical Society of the Pacific **110**, 3 (1998).
[33] D. K. Galloway, et al,. APJ**. 549**, L85 (2001).
[34] D. Q. Lamb. APJ. Supplements Series **127**, 395 (2000).
[35] D. A. Smith, et al,. APJ. **479**, L137 (1997).
[36] G. E. Brown, et al,. APJ. **547**, 345 (2001).
[37] M.C. Miller & F.K. Lamb. APJ **499**, L37 (1998).
[38] T.E. Strohmayer. APJ**. 523**, L51 (1999).
[39] J. Jose & M. Hernanz. APJ. **494**, 680 (1998).
[40] R.K. Wallace & S.E. Woosley. APJ. Supplement Series **45**,389 (1981).
[41] H. Schatz, et al,. APJ. **524**, 1014 (1999).
[42] E.V. Gotthelf, et al,. APJ. **490**, L161 (1997).
[43] E.C. Ford. APJ **519**, L73 (1999).
[44] R.E. Taam, S.E. Woosley, & D.Q. Lamb. APJ **459**, 271 (1996).
[45] S. Starrfield, et al,. Physics Report **227**, 223 (1993).
[46] E. Anders & N. Grevesse. Geochim. Cosmochi. Acta **53**, 197 (1989).
[47] W. M. Sparks, et al,. APJ **220**, 1063 (1978).
[48] D.W. Bardayan & M.S. Smith. Phys. Rev. C **56**, 1647 (1997).
[49] J. Gomez del Campo, et al,. Phys. Rev. Lett. **86**, 43 (2001).
[50] H. Schatz, et al. Phys. Rev. Lett. **86**, 0031 (2001).
[51] M. Wiescher, et al,. APJ. **326**, 384 (1988)
[52] J.-F. Rembges, et al,. Nuclear Physics A **621**, 413c **(year).**

[53] M. Politano, et al,. APJ. **448**, 807 (1995).
[54] A. Coc, et al,. Astron. Astrophys. **299**, 479 (1995).
[55] M. Wiescher, et al,. APJ **316**, 162 (1987).
[56] J. MacDonald. APJ. **267**, 732 (1983).
[57] H. A. Bethe. Phys. Rev. **55**, 434 (1939).
[58] A. Spitkovsky, et al,. APJ. **566**, 1018 (2002).
[59] H. Hendl, et al,. Physical Review C **52**, 1078 (1995).
[60] E.M. Burbidge, G.R. Burbidge, A.A. Fowler, & F. Hoyle. Rev. Mod. Phys. **29**, 547 (1957).
[61] W.A. Fowler, G.R. Caughlan, & B. Zimmerman. ARA & A **5**, 525 (1967).
[62] H. Schatz, et al,. Physics Report **294**, 167 (1998).
[63] R.D. Atkinson. The Observatory **69**, 161 (1949).
[64] O. Messer. PhD Dissertation University of Tennesse (2000)
[65] S. Parete-Koon, et al,. APJ. in preparation (2002); M.S. Thesis Univ. Tennessee (2002).
[66] M.S. Smith,et al,. In Preparation (2002).
[67] W.R. Hix & F.K. Thielemann, Journal of Computational and Applied Mathematics, **109,** 321-351, (1999)

[68] F.K. Thielemann, et al., http://ie.lbl.gov./astro/friedel.html

[69] T. Rauscher and F.-K. Thielemann, At. Data Nucl. Data Tables 75, 1 (2000).
[70] P. Moller, J.R. Nix, K.-L. Kratz, At. Data Nucl. Data Tables 66 (1997)131.
[71] M. Hirsch, A. Staudt, K. Muto, H.V. Klapdor-Kleingrothaus, At. Data Nucl. Data Tables 53 (1993) 165.
[72] G.R. Cauglan & W.A. Fowler. At. Nucl. Data Table **40**, 283 (1998).
[73] W. R. Hix *et al.*, Nuclear Reaction Rate Uncertainties and Their Effects on Nova Nucleosynthesis Modeling, in Proceedings of the 2nd Chicago Conference on Astrophysical Explosions, ed. E. Brown, J. Niemeyer, R. Rosner & J. Truran, in press
[74] E.F. Brown, et al. APJ **574**, 920 (2002).
[75] http://www.onlineastronomy.com/ (December, 2001)
[76] Press, W.H., Teulosky, S.A. Vwtterling, W.T., Flannery, B.P. *Numerical Recipes.* Cambridge, second edition (1992)
[77] Nuclear Wallet Cards, J. K. Tuli, National Nuclear Data Center, Brookhaven National Laboratory, (2000).

VITA

Luc Lucius Dessieux, Jr. was born in 1973, in Cap-Haitien, Haiti. He received a Bachelor of Arts degree in 1997 from Central Methodist College in Fayette, Missouri where he double majored in Physics and Mathematics. In 1996 he was he inducted into Kappa Mu Epsilon mathematics honor society. He received a Masters degree in Physics from the University of Tennessee in Knoxville in December of 2002.